Structure of the neutron-deficient nuclei ^{173}Au and ^{173}Pt and their α-decay descendants

Thesis submitted in accordance with the requirements of the University of Liverpool for the degree of Doctor in Philosophy

by

Alexander Michael Thornthwaite

Oliver Lodge Laboratory

2014

Abstract

Fusion-evaporation reactions have been used to populate excited states in ^{173}Au and ^{173}Pt, and expand the level schemes for these nuclei. Transitions feeding the $\pi^{-1}(s_{1/2})$ state in ^{173}Au have been discovered for the first time. No collective behaviour was observed in ^{173}Au either. Although no evidence of isomeric transitions or fine structure was present for the decay chain of ^{173}Au, an isomeric transition in ^{173}Pt was observed for the first time. It was found to be decaying from ^{173}Pt's $\nu(i_{13/2})$ band head to the $\nu(h_{9/2})$ band head. The excitation energy of both of these bands have been determined for the first time. The $\nu(h_{9/2})$ feeds the ground state via decay of a 104-keV γ ray. The ground state of ^{173}Pt has been established to be $\nu(f_{7/2})$. These new findings were compared to systematic trends for both the Pt and Au isotopes.

α-decay analysis of ^{173}Pt suggests a $\nu(f_{7/2})$ ground state for the daughter nucleus ^{169}Os, with the 35-keV $(5/2^-)$, 112-keV $(9/2^-)$, 136-keV and 171-keV states being populated via fine structure of ^{173}Pt's α decay. The α-decay chains originating from the isomeric $\pi^{-1}(h_{11/2})$ state and the $\pi^{-1}(s_{1/2})$ ground state have been studied, culminating in the observation of the α decay of ^{161}Ta^m and ^{165}Re^g, respectively. As well as reporting a new activity in the decay of ^{165}Re^g and confirming that the known α decay of ^{161}Ta is associated with the high-spin isomer, this work has allowed the excitation energy of the high-spin state of ^{161}Ta to be determined for the first time. In combining these new measurements with the information already available on ^{157}Lu it has also been possible to deduce the Q_α-value for the decay of the ground state of ^{161}Ta. This has enabled the Q_p-values of ^{161}Ta to be measured to give -129(24) keV and -37(21) keV for the ground and isomeric state, respectively, indicating that these states are only just bound with respect to proton

emission. The nuclear masses were deduced from Q_α measurements in this work and were found to be consistent with values obtained from more direct methods, such as Schottky mass spectrometry or Penning trap mass spectrometry.

Acknowledgements

Firstly, I would like to thank my two supervisors: Prof Robert Page and Dr David Joss, for providing the support, guidance and insight that I found invaluable during the course of my research. While they have many commitments, my supervisors have always found the time to discuss any issues that I have encountered. I would also like to thank my collaborators from the University of Jyväskylä (there are too many to list here!) for their assistance and for the successful experimental run, in which high quality data were produced. I would also like to thank Dr Martin Venhart for his insight and for taking the time out to show us Bratislava earlier this year. A big shout out to all of the other academic staff in the nuclear physics department at the University of Liverpool, for going out of their way to make sure that students are happy with what they are doing. Many thanks to the Science and Technology Facilities Council for providing funding for my research.

Secondly, a huge thanks goes out to Dave O'Donnell, for his invaluable support, and for being there if I ever had questions. I wish you the best for your future in Glasgow. I would also like to thank Robert Carroll, to whom now works in Surrey, for his invaluable support regarding Grain and the sort codes. A big thanks goes out to Paul Sapple for help getting me started without difficulty. Other thanks goes to the fellow PhD students: Bahadır Sayği, Mark Drummond, John Revill, Edward Parr, Fuad Ali, Daniel Cox, Joseph Rees, Joseph McKenna, Jamie Dormand, Alex Gredley, Faye Wearing, and Liam Vormawah for both their social and/or academic support. A special thanks goes out to Andrew "Everything is going to be just fine" Mistry and Chris "Xmas" McPeake.

Thirdly, for their enduring support, a special thanks goes out to my family: my mother Anne, father David, grandmother Edith, brother Glynn, auntie Jean, uncle Brian, and

cousins Stephen and Lynsey. My thanks also goes out to my extended family, which include my step mother Cheryl, and step brother Philip.

Finally, a special thanks to Stephen Philp for the support I needed during my undergraduate years at Liverpool; we remain as trusted friends whom will always be there in times of need. This can also be said of Warren Peters, whom gave me the honour to be his son's godfather. I also appreciate the support and motivation received from Iain Turner, Dave Collins, James Chang, Peter and Carol Sims, Ian Stott, Jason Blackford and Robb Bryant over the course of my life, and will remain as close life-long friends. A final shoutout to Eric Adil whom I can also trust and appreciate enduring support.

Contents

Chapter 1

Introduction

Studying nuclei around the proton drip line has become a major field of research in recent decades [1, 2]. With the successes of utilising fusion evaporation reactions, it has been possible to populate isotopes with greater neutron-deficiency, particularly in the region $N > 82 > Z$. Due to its proximity within the mid-shell region, many of the studied isotopes exhibited collective behaviour, and some had been found to coexist in entirely different shapes [3]. This knowledge has been invaluable for the testing of the current nuclear models, particularly for nuclei located beyond the drip line, where the outermost proton has become unbound. By studying the properties of emission of protons from these nuclei, one can reveal, with reasonable confidence, the nuclear structures of that configuration. The main limiting factor has been the use of stable beam projectiles in order to produce such exotic compounds. In order to reach the required neutron deficiency, one must evaporate many neutrons from the compound formation, which drastically reduces the production cross section. Despite this, several experiments have used this approach to collect as much data as possible for these nuclei, which currently serve as the current benchmark for our understanding of the proton drip line.

Figure 1.1 shows the full and expanded views of the Segrè chart, where the expanded region shows several nuclei of interest that were populated from a compound nucleus produced in this work's experiment. By coupling a high resolution, highly segmented, γ ray detector array with a powerful recoil separator and focal plane spectrometer, a

complete picture of the compound nucleus and its decay properties can be established. This has many implications; for example, by combining a correlated sequence of α decays from each generation of nuclei, and including measurements from other literature, it can be possible to indirectly measure the atomic mass of these exotic nuclei, as long as at least one nucleus in the decay chain has had its mass measured directly. Other methods include searching for exotic shapes, or simply cataloguing the evolution of nuclear structure towards instability.

Previous work that cover the nuclei of current interest in this work have already revealed interesting properties about them. In the case of ^{173}Au, a proton-unbound isotope, no collective structure had been observed [4], making this the first odd-mass isotope to exhibit such behaviour. Decay spectroscopy of its α decaying parent, ^{177}Tl, suggests a $\pi^{-1}(h_{11/2})$ long-lived isomer, along with a $\pi^{-1}(s_{1/2})$ ground state configuration [5]. The α-decaying grand-daughter of ^{173}Au, ^{165}Re, only has a reported decay from its isomeric state prior to this work [6]. The α-decay of ^{161}Ta, which is the α-decaying great-grand-daughter isotope of ^{173}Au, has only been reported for one state, and has been assumed to be emanating from its ground state [7]. This work has explored the decay schemes for both the low- and high-spin states of these nuclei, in order to verify the previously assigned α-decay paths.

^{173}Au's neighbouring isobar, ^{173}Pt, was also populated in previous experiments [9, 10]. Evidence showed collective behaviour in this nucleus, and followed the trend of collectivity within a large range of Pt isotopes. However, not much else is currently known about the structure of ^{173}Pt except for its $\nu(i_{13/2})$ intruder band [9] and its α decaying properties, which another study had found to exhibit fine structure to its daughter nuclide, ^{169}Os [10]. Unfortunately, the low-spin orbitals in ^{169}Os were not able to be linked with the previously discovered yrast band [11]. Calculations by Möller *et al.* have suggested ground state spin and parity assignments of $(1/2^+)$ for ^{169}Os, and $(3/2^+)$ for ^{173}Pt [12], although other literature have suggested a $(5/2^-)$ ground-state configuration for ^{177}Hg, ^{173}Pt, ^{169}Os and ^{165}W [10, 13]. By combining the efforts of in-beam, focal-plane and decay spectroscopy of the nuclei ^{173}Pt and ^{169}Os in this work, these configuration assignments were able to

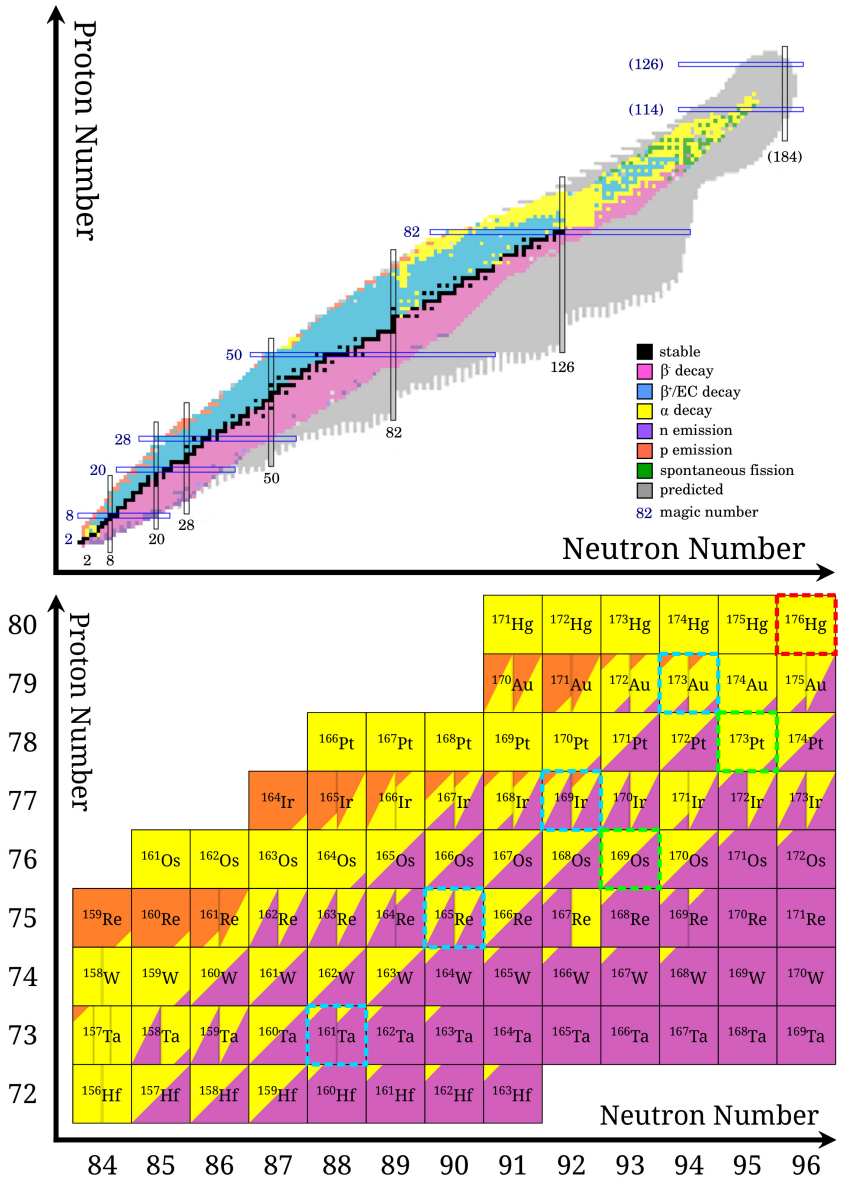

Figure 1.1: (Top) The chart of the nuclides, containing stable (solid black squares) nuclei, as well as synthesised and naturally-found radioactive nuclei, in which their primary radioactive decay modes are colour coded as shown in this figure. Yet discovered nuclei that are predicted by nuclear models are marked in grey. Image modified from the NNDC [8]. (Bottom) A zoomed-in section showing the region of interest in this work. The compound nucleus produced in this experiment is outlined in dashed red. The nuclei that are to be studied in this work are outlined in dashed green and dashed cyan.

be verified. With the increased amount of statistics available, as well as the accessibility to various, high-performing instruments, has allowed the obtainability of more detailed information for these exotic nuclei.

Chapter 2

Nuclear Structure

The understanding of atoms that contain most of their mass in a highly dense, positively charged, nucleus had been realised for the past century. It was unambiguously proven with a series of experiments performed by E Rutherford, with assistance from H Geiger and E Marsden [14] (and references therein), while also disproving other, earlier, proposed atomic models [15]. The Rutherford model of the atom serves as the foundation of atomic and nuclear physics, and was later refined into more accurate descriptions of the atom. For example, due to the fact that orbiting electrons would lose kinetic energy, and thus spiral into the nucleus, Rutherford's model was refined by Rutherford himself, working alongside with N Bohr, to give the *Bohr model* of the atom [16]. By including the relatively new quantum phenomena at the time, the model places atomic electrons into discreet 'energy levels' in an atom, and thus can only absorb or emit discreet wavelengths of light to move between these states.

The first sub-atomic particle, the *proton*, was discovered by Rutherford also, in what was considered the first induced nuclear reaction performed [17]. As with most of Rutherford's early experiments, a radioactive α source was used. When the emitting α particles were fired into gaseous nitrogen (^{14}N), which was used in this experiment, the two nuclei fused together, producing an isotope of oxygen, ^{17}O, along with an evaporated proton. However, the mass from the protons in the nucleus did not add up to the atomic mass, and Rutherford postulated a neutral particle, similar to that of the proton, making up the

remainder. It was not until 1932 when J Chadwick's reported discovery of the neutron [18] confirmed Rutherford's hypothesis. Neutrons are produced by bombarding α particles at a beryllium (^{9}Be) target, which fuse to create an isotope of carbon, ^{12}C, and an evaporated neutron.

2.1 The Liquid Drop Model

The mass of the atomic nucleus could now be calculated for a given nucleus that contains Z protons and N neutrons, and is given by

$$m = Zm_p + Nm_n - \frac{E_B}{c^2}, \tag{2.1}$$

where m_p, m_n, E_B and c are the proton and neutron's mass, the nuclear binding energy and the velocity of light, respectively. The first nuclear model, the *semi-empirical mass formula*, was formulated by C Weizsäcker in 1935, and was used to estimate the binding energy of the nucleus, and thus its mass, by using the liquid drop model. This model treats the nucleus as a spherical incompressible fluid, with all the nucleons held together by the short-interacting strong force. The formula used is given by

$$E_B = a_V A - a_S A^{2/3} - a_C \frac{Z(Z-1)}{A^{1/3}} - a_A \frac{(A-2Z)^2}{A} - \delta(A,Z), \tag{2.2}$$

where $A = Z + N$. Each of the five terms has a corresponding coefficient, which can either be calculated from principle, or obtained empirically from experimental data, which was performed by K Heyde [19].

Volume Term

The primary term arises due to the attraction of nucleons inside a volume of infinite size. As the nuclear strong force is short range, the nucleons generally only interact with their nearest neighbours. As the strong force is saturated over the dimensions of the size of the nucleus, the volume binding energy is roughly proportional to the number of nucleons A, as opposed to the total number of nucleon pairs, $A(A-1)/2$, should the force have a longer interaction range. This gives a constant volume binding energy *per nucleon*. The

coefficient for the volume term can be calculated by assuming the nucleus is made up of non-relativistic Fermi gas particles populating quantum states, in a spherical shape, up to the system's Fermi energy. Since the particles behave thus, their energy is minimised by having an equal number of protons and neutrons, all of which have filled energy states in pairs. The coefficient for this term was calculated to have a result of $\approx$ 20MeV, close to the empirical value of 15.75MeV.

Surface Term

As the nucleus is of finite size, the total binding energy is corrected by surface effects, which have less neighbouring nucleons compared to inside the bulk. As the volume term is proportional to A, then the surface term should be proportional to $A^{2/3}$, and the nuclear radius $A^{1/3}$. The coefficient for the surface term can be calculated the same way as for the volume term, giving roughly the same result. This is also close to the empirically determined value of approximately 18.34MeV.

Coulomb Term

This term includes electrostatic repulsive effects due to the nucleus containing positively charged protons within close proximity. Since the electromagnetic force interacts at long ranges, all of the protons feel the repulsive effects. At least two protons must be present inside the nucleus for the repulsive effect to take place. Using the approximated nuclear radius as $R = 1.25A^{1/3}$ fm, and assuming a uniform spherical charged distribution with a hard edge, the average Coulomb potential, $\langle E_C \rangle$, is given as

$$E_C = \frac{3e^2 Z(Z-1)}{5 \cdot 4\pi\epsilon_0 1.25 A^{1/3} \cdot 10^{-15}}, \tag{2.3}$$

where e is the fundamental electric charge, and ϵ_0 is the permittivity of free space. The coefficient for the Coulomb repulsion, a_C, can be calculated using the above assumptions to give

$$a_C = \frac{3e^2}{5 \cdot 4 \cdot 1.25\pi\epsilon_0 \cdot 10^{-15}} \approx 0.69\text{MeV}. \tag{2.4}$$

The calculated value is very close to the empirically determined value of 0.71MeV.

Asymmetry Term

While the volume term accounts for the Pauli Exclusion Principle for an equal number of protons and neutrons, the asymmetric term accounts for an excess number of protons or neutrons. As protons and neutrons are treated as two different projections of the nucleon's *isospin*, a single quantum state can be filled with both a proton and a neutron. If there are an excess number of either nucleon, these must occupy higher energy levels, which once again, increases the total energy of the nucleus. The magnitude of the reduction of binding energy, when using the Fermi gas model, is proportional to $(A-2Z)^2$, and is the second order term that appears in the derived equation for the average nucleon energy. The calculated coefficient for the asymmetry term (≈ 11MeV) is smaller than the reported value (23.21MeV) by a factor of just under two; this is because the estimated method ignores any change in the nuclear potential when the relative number of protons or neutrons changes.

Pairing Term

The second term, is a correction to the formula that takes into account the nucleon's spin-orbit interaction. For a particle that has a spin of 1/2, two can occupy the same quantum state with different spin projections: the spin-up $|\uparrow\rangle$ and spin-down $|\downarrow\rangle$ states. It is energetically favourable for all the nucleons, protons and neutrons alike, to occupy these states in *pairs*, reducing the total energy of the nucleus. This effect is reduced if the most outlying unpaired nucleon is located in a quantum state, and is further reduced if both outlying proton and neutron are unpaired. The expression for the pairing term is given as

$$\delta_{A,Z} = \begin{cases} +\delta_0 & Z, N\text{even } (A \text{ even}) \\ 0 & A\text{odd} \\ -\delta_0 & Z, N\text{odd } (A \text{ even}) \end{cases} \tag{2.5}$$

where δ, found empirically, is given by

$$\delta_0 = \frac{a_P}{A^{1/2}}. \tag{2.6}$$

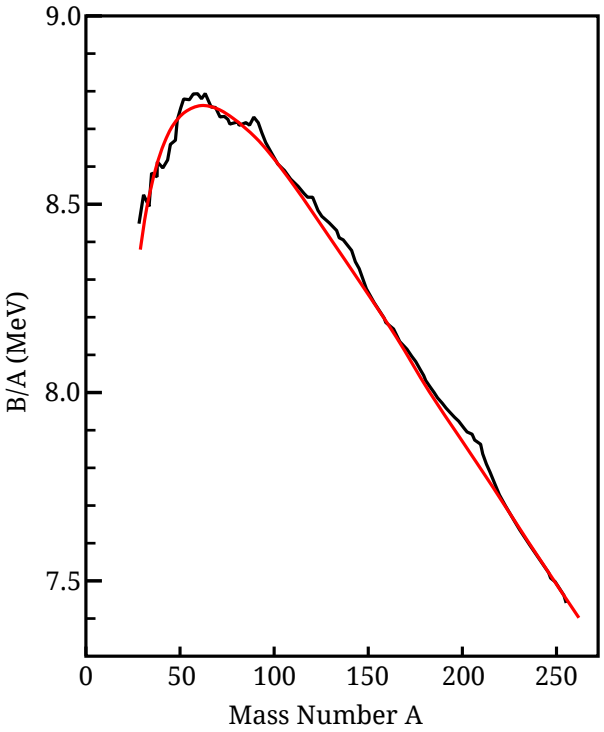

Figure 2.1: The calculated semi-empirical mass formula binding energy per nucleon (red) compared against the experimental values (black). Image modified from [19].

The pairing term coefficient was empirically determined to give 12MeV. The dependency on the mass number in the pairing term, $A^{-1/2}$, is smaller than the expected dependency of A^{-1} for the asymmetry term when using the Fermi gas approach; the nucleon pairing for large nuclei gives stronger binding energies than due to the proton-neutron asymmetry.

The binding energy per nucleon, B_E/A, is written as

$$\frac{E_B}{A} = a_V - \frac{a_S}{A^{1/3}} - a_C\frac{Z(Z-1)}{A^{4/3}} - a_A\frac{(A-2Z)^2}{A^2} - \frac{\delta(A,Z)}{A}. \tag{2.7}$$

When using the empirically determined coefficients to calculate the binding energy per nucleon, utilising all of the terms, successfully reproduces the experimentally found most stable nucleus of ^{62}Ni, with $\Delta E_B/A = |E_B/A_{exp} - E_B/A_{calc}| \approx 40$ keV [20], (it should be noted that ^{56}Fe is usually the end point of the stellar fusion process, due to the fact that in order to reach the two more bound isotopes: ^{58}Fe and ^{62}Ni, requires fusion reactions with nuclei simply not present at that stage inside a star). The mass formula also successfully demonstrated that performing nuclear fission for the heavier isotopes, and nuclear fusion

for the lighter isotopes, provided an excess of energy. This was later utilised for practical solutions, such as nuclear power plants and, more controversially, the development of nuclear weapons.

2.2 The Nuclear Shell Model

The liquid drop model produces a reasonable trend of nuclear binding energies for a range of nuclei; the comparison is shown in figure 2.1. However, it very poorly reproduces the binding energies for the lighter nuclei, non-spherical nuclei, and nuclei located around certain numbers of protons and neutrons, due to their *shell effects*. The liquid drop model can be modified for non-spherical nuclei, and is covered, in more detail, in Nuclear Deformation, section 4 of this chapter.

The liquid drop model uses the Fermi gas model, in which the density of states in the nucleus are constant, which is not the case for real systems. The *nuclear shell model* attempts to tackle this problem using a purely quantum mechanical system, completely analogous to the quantum atomic model used for the atomic shell electrons. While the use of perturbation theory in quantum electrodynamics allows precise calculations of the electron binding energies inside the atom, due to electromagnetism's small coupling constant, $\alpha_{fs} \approx 1/137$, the same cannot be said for hadrons, which their interactions are governed by the strong force. Perturbation theory relies on smaller than unity coupling constants, and at relatively low energies, the strong force's coupling value is around unity, making this method impossible to reach convergence. it is therefore necessary to employ alternative methods to model, in detail, the structure of a nucleus and the interactions between the constituent nucleons.

The shell model was formulated in 1949 by independent contributions from Mayer, Jensen, Haxel and Suess. It describes a system of particles that occupy discrete states inside a potential well. These quantum states have corresponding wavefunctions, $|\psi\rangle$, which are a set of eigenfunctions. Schrödinger in the 1920s had formulated an equation in which the energy eigenvalues, E, were obtained after applying the *Hamiltonian* to the

wavefunction. The time-independent relation is given by

$$\hat{H}\,|\psi\rangle = E\,|\psi\rangle\,, \tag{2.8}$$

where the *Hamiltonian* operator, $\hat{H}$, analogous to the classical equation of motion of a particle, is written as

$$\hat{H} = -\frac{\hbar^2}{2m}\nabla^2 + V(\mathbf{r}), \tag{2.9}$$

with

$$\nabla^2 = \frac{\partial^2}{\partial x^2} + \frac{\partial^2}{\partial y^2} + \frac{\partial^2}{\partial z^2} \tag{2.10}$$

being the Laplace formula, expressed in Cartesian coordinates. Using the polar coordinate system, it can be expressed as

$$\nabla^2 = \frac{\partial^2}{\partial r^2} + \frac{2}{r}\frac{\partial}{\partial r} + \frac{1}{r^2}\left(\frac{1}{\sin(\theta)}\frac{\partial}{\partial\theta}\left(\sin(\theta)\frac{\partial}{\partial\theta}\right) + \frac{1}{\sin^2(\theta)}\frac{\partial^2}{\partial\phi^2}\right), \tag{2.11}$$

which is extremely handy in separating the radial component of the wavefunction from the angular component, when the potential energy only depends on its radial component. This allows the angular components of the wavefunction to be solved directly, yielding *spherical harmonics* $Y_{\ell m_\ell}(\theta,\phi)$, and their functions depend on the angular momentum, l, and its magnetic projection, m_ℓ, of the state, for $\ell \geq 0$ and $-\ell \leq m_\ell \leq +\ell$. The spherical harmonics are the eigenfunctions for the momentum operator $\hat{\ell}^2$, which gives the corresponding eigenvalues $\ell(\ell+1)\hbar^2$.

The simplest construction of a quantum system uses a one-dimensional infinite square well potential that, inside the boundary between $0 < x < a$, has a uniform potential $V = V_0$, and $V = \infty$ outside. The solution for the wavefunction

$$|\psi\rangle = A\sin(kx), \tag{2.12}$$

must satisfy the boundary conditions

$$A\sin(ka) = 0;\; ka = n\pi, \tag{2.13}$$

giving the energy eigenvalues as

$$E_n = \frac{\hbar^2 \pi^2 n^2}{2ma^2}, \tag{2.14}$$

where n is the *principal quantum number*.

For an infinite spherical well of radius a, the wavefunction, when expressed in polar coordinates, now includes the radial component, which is interpreted as the particle's angular momentum. The resulting energy eigenvalues is similar to that of above

$$E_{n,\ell} = \frac{\hbar^2 \left[k_{n,\ell}^2\right]}{2m}, \tag{2.15}$$

where $k_{n,\ell} = X_{n,\ell}/a$ is the wave number for values of n and ℓ. For $\ell = 0$, the wavefunction only has a radial component, reproducing the energy eigenvalues for the infinite square well. For non-zero angular momentum, the values of $X_{n,\ell}$ are found numerically, by finding the roots of the Bessel function

$$J_l(ka) = 0. \tag{2.16}$$

The experimental nuclear shell gaps of 2, 8, and 20 were reproduced; larger shell closures still disagree with the experimental shell closures, however. Experimental shell gaps in nuclei contained 28, 50, or 82 protons, or 28, 50, 82 or 126 neutrons, or a mixture of both. These highly-bound configurations are referred to as *magic nuclei*, because they contain at least one *magical number* of protons or neutrons. Similar calculated results can be obtained if the potential well was changed from an infinite spherical well to that of a harmonic oscillator with the given potential as

$$V(r) = \frac{1}{2} m\omega^2 r^2 - V_0, \tag{2.17}$$

resulting in the energy eigenvalues as

$$E_{n,\ell} = \hbar\omega \left\{ (2(n-1) + \ell) + \frac{3}{2} \right\} - V_0. \tag{2.18}$$

Figure 2.2 shows the calculated energy eigenvalues described in both potential wells,

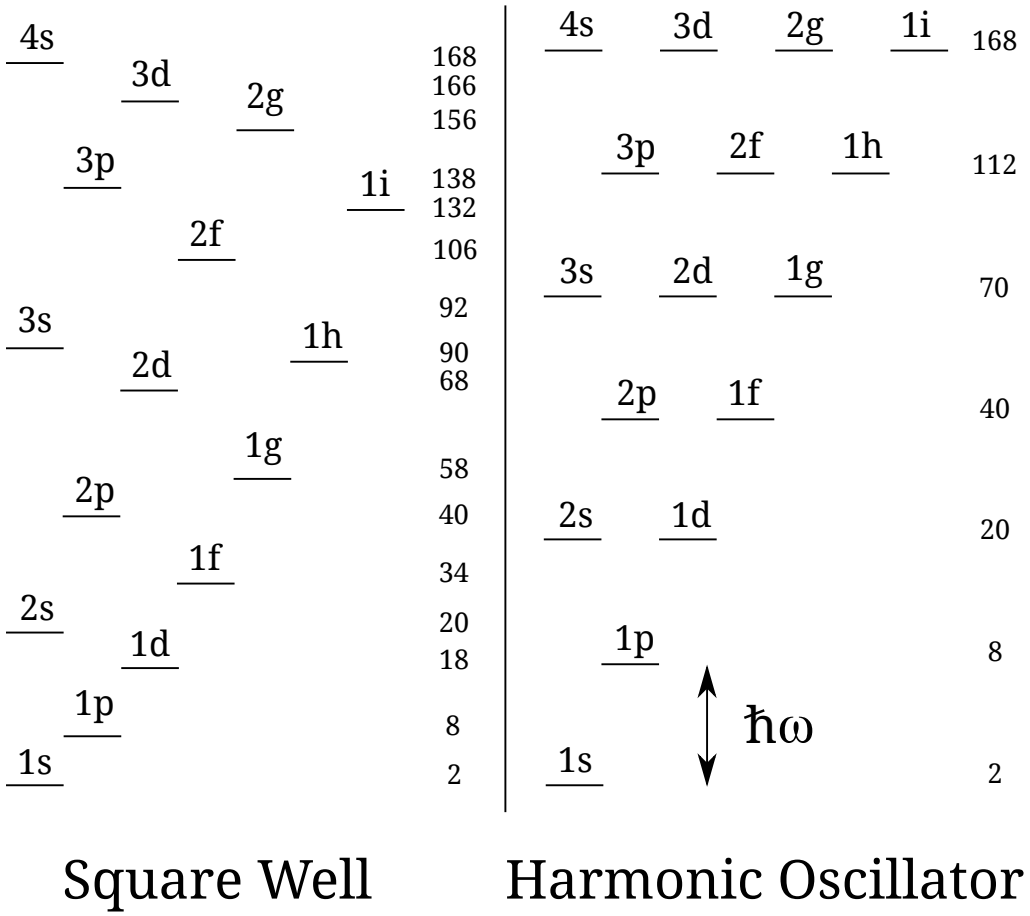

Figure 2.2: The calculated energy eigenstates for two different nuclear potentials: The infinite spherical well (left), and the harmonic oscillator (right). Figure obtained from [21].

along with the number of degenerate states due to the magnetic substates: $m_\ell = -\ell, -\ell+1, -\ell+2, \ldots, +\ell-1, +\ell$, and due to the spin of a fermion particle: $m_s = -1/2, +1/2$. A large degeneracy is noted, particularly for the higher quantum states. This degeneracy is lifted by including the term $\hat{j}^2$ to the nuclear potential

$$V(r) = \frac{1}{2}m\omega^2 r^2 - V_0 - \frac{2}{\hbar^2}\hat{j}^2, \tag{2.19}$$

where

$$\hat{j}^2 = (\hat{\ell} + \hat{s})^2 = \hat{\ell}^2 + \hat{s}^2 + 2\hat{\ell}\cdot\hat{\mathbf{s}} \tag{2.20}$$

contains the *centrifugal* term, $\hat{\ell}^2 = \hbar^2 \ell(\ell+1)$, and the *spin-orbit* coupling term

$$\begin{aligned} \hat{\ell} \cdot \hat{\mathbf{s}} &= \frac{\hbar^2}{2} \left\{ \hat{j}^2 - \hat{\ell}^2 - \hat{s}^2 \right\} \\ &= \frac{\hbar^2}{2} \left\{ j(j+1) - \ell(\ell+1) - \frac{3}{4} \right\}. \end{aligned} \tag{2.21}$$

The harmonic oscillator's potential can now be written as

$$V(r)_{\ell,j} = \frac{1}{2} m\omega^2 r^2 - V_0 - 2\alpha_c \left\{ \ell(\ell+1) + \frac{3}{4} \right\} - \alpha_s \left\{ j(j+1) - \ell(\ell+1) - \frac{3}{4} \right\}, \tag{2.22}$$

where α_c and α_s are the strengths of the centrifugal and spin-orbit interactions, respectively. With two possible spin orientations, $j = \ell \pm 1/2$, the spin-orbit component differs between the parallel and anti-parallel states. The orbital centrifugal term, $\propto \ell^2$, flattens the potential well of the harmonic oscillator, giving it a more realistic function. The modified energy eigenvalues of the modified harmonic oscillator

$$E_{n,\ell,j} = \hbar\omega \left\{ (2(n-1) + \ell) + \frac{3}{2} \right\} - V_0 - 2\alpha_c \left\{ \ell(\ell+1) + \frac{3}{4} \right\} + \alpha_s \begin{cases} -\ell \\ \\ \ell + 1 \end{cases} \tag{2.23}$$

lifts the degeneracy of the total angular momentum, $j = \ell \pm 1/2$, of a given state in the nucleus. This approach successfully reproduces the observed effects of nuclei that contain these specific amount of protons and/or neutrons. Figure 2.4 shows the splitting of the various orbitals due to the spin-orbit coupling.

While using the harmonic oscillator has the benefits of calculating the solutions to the wavefunctions analytically, it is not an accurate description of the nuclear potential. Several different nuclear potentials were employed, each producing different energy eigenvalues as a result. Figure 2.3 illustrates the various different functions used. From the experimentally measured charge densities of spherical nuclei, the *Woods-Saxon* potential describes the nuclear potential with the most accuracy. The formula of this nuclear potential is given by

$$V(r) = \frac{V_0}{1 + \exp((r-R)/a)}, \tag{2.24}$$

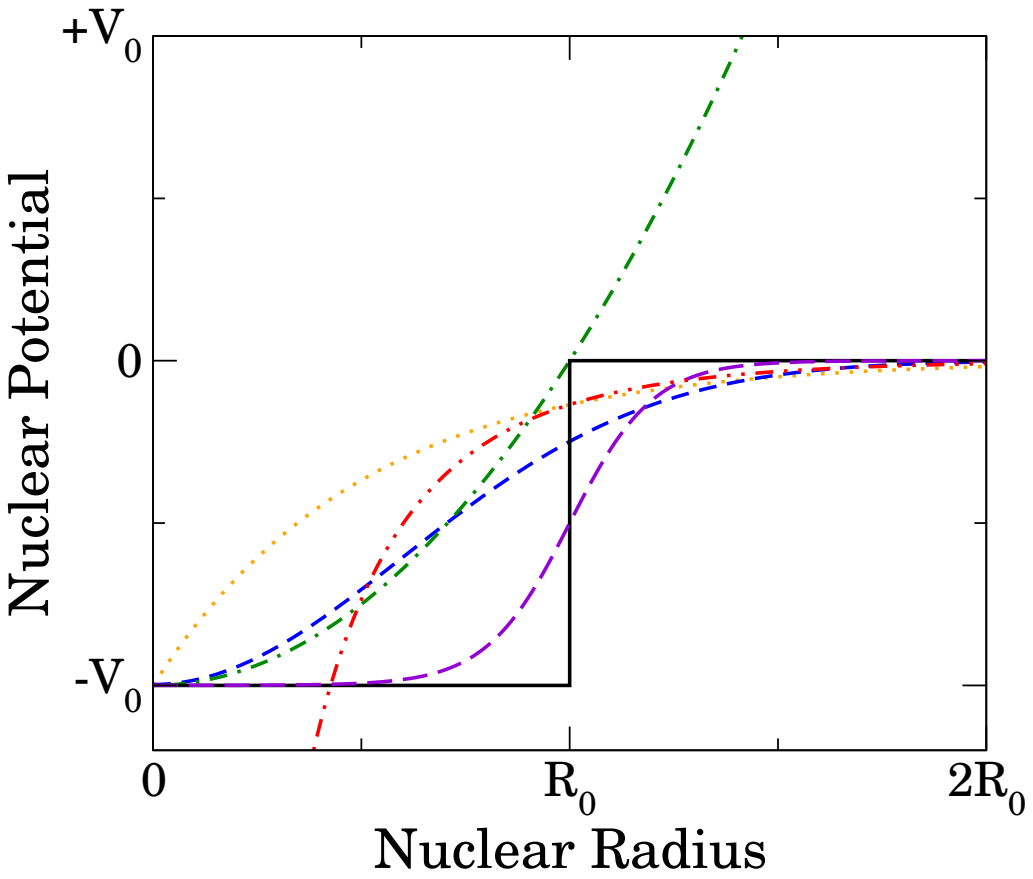

Figure 2.3: Illustration of the various mean field potentials used to describe the nucleus. The potential functions include: Spherical Harmonic Oscillator (green), Square Well (black), Gaussian (blue), Exponential (orange), Yukawa Potential (red) and Woods-Saxon Potential (violet).

where $R = r_0 A^{1/3}$, $r_0 = 1.25$ fm and $a = 0.67$ fm. Solutions to the wave equation were solved numerically; the eigenstates are presented in figure 2.4, and show subtle differences compared to the modified harmonic oscillator potential.

2.3 Nuclear n-body Systems

The above description of the shell structure of the atomic nucleus assumes a single nucleon interacting with the mean nuclear potential, and travel with negligible collisions with other nucleons, giving them a very large mean free path. This assumption, however, is contrary to the nuclear strong force's short interaction range. Nucleons interact with other nucleons within distances of a few femtometres [22]; multiple body interactions inside the

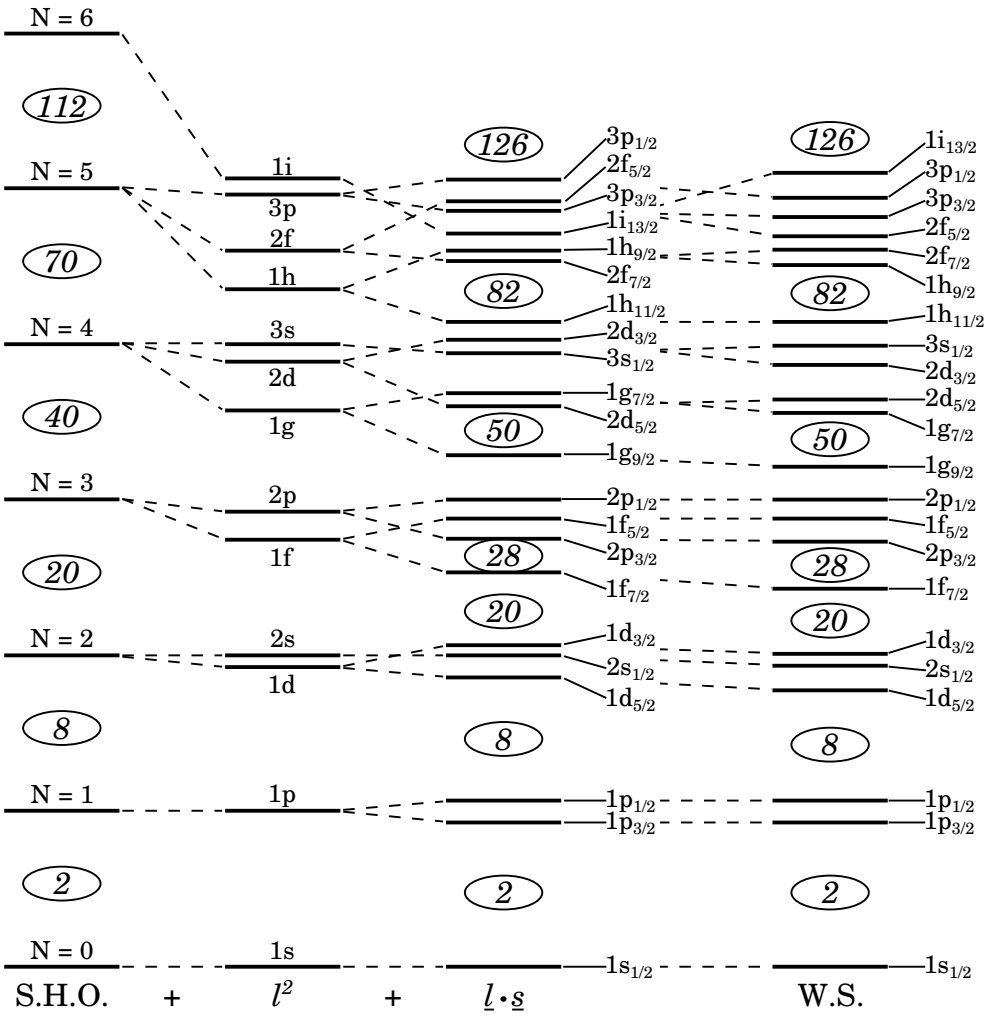

Figure 2.4: The energy eigenstates when using, from left to right, a spherical harmonic oscillator, the centrifugal correction term, the spin-orbit correction term, and the Woods-Saxon potential. This figure has been modified from [21].

nucleus is necessary, therefore, in order to acquire more accurate energy eigenvalues. This consequently also affects the nuclear potential between the collisions of nucleons. The n-body Schrödinger equation becomes

$$\hat{H}\psi = E\psi, \tag{2.25}$$

where the n-body Hamiltonian is given by

$$\hat{H} = -\frac{\hbar^2}{2m_i}\sum_i \nabla_i^2 + \sum_{i,j} V_{i,j} + \sum_{i,j,k} V_{i,j,k} + \cdots. \tag{2.26}$$

Finding the solutions to the n-body problem requires the use of Monte-Carlo methods, in which substantial computing power is required to obtain accurate properties of the nucleus. With recent advances in computing technology, nuclear properties of light nuclei have been calculated to high accuracy; the significant complexity of the n-body formula, however, makes evaluation of even medium-mass nuclei impractical. More approximate methods are required, therefore, which are used to estimate the nuclear properties for the heavier isotopes.

The *Hartree-Fock* method simplifies this process somewhat, by approximating the nuclear potential to that of a mean field between the nucleon-nucleon (NN) interaction. The non-relativistic Hamiltonian of the mean field NN system can be written as

$$\hat{H} = \sum_{i=1}^{A} \left(\frac{-\hbar^2}{2m_i} \nabla_i^2 + V(\vec{r}) \right), \tag{2.27}$$

where $V(\vec{r})$ is the mean-field potential, consisting of a single body potential that has been *perturbed* by the potential due to the interaction with a second particle. The solutions using the Hartree-Fock approach also utilise Skyrme forces [23]; zero range structures that contains a density dependence to the nucleon-nucleon potential field. While non-trivial, the nuclear properties for spherical and near-spherical nuclei can be calculated to reasonable accuracy using an iterative method.

2.4 Nuclear Deformation

Thus far, the nucleus has been described as a system of either non-interacting or interacting nucleons that feel an averaged potential well that was assumed to be spherical (with the exception of the full Monte-Carlo calculations, which evaluates the multi-body interaction explicitly). For nuclei located at or near the magic numbers, this setup describes their behaviours with reasonable accuracy. However, these cases are isolated; for a large number of atomic nuclei are found to exhibit collective properties, particularly in the mid-shell gap regions. These collective motions of particles behave either *vibrationally*, *rotationally* or in a *transitional* state.

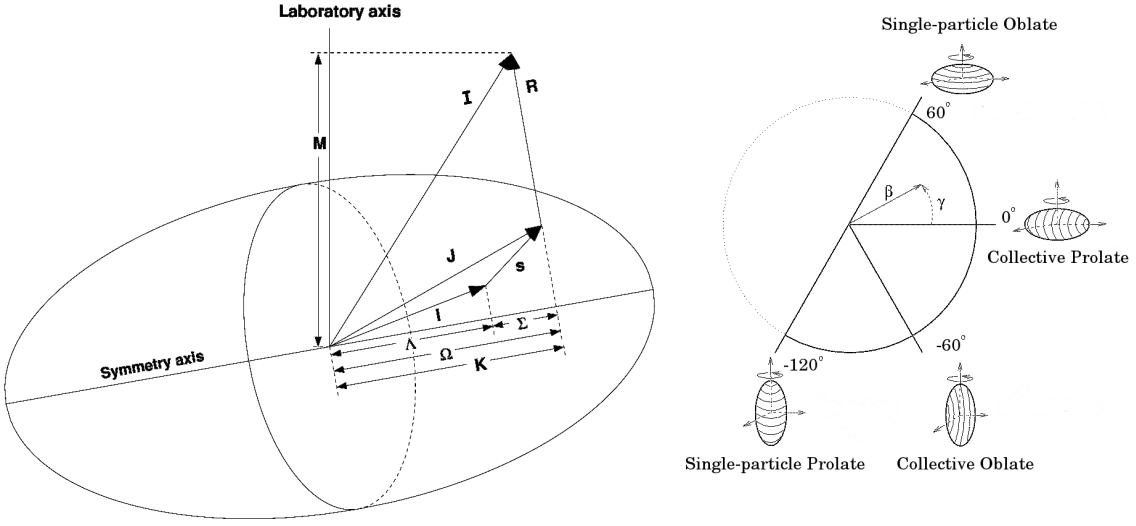

Figure 2.5: (Left) An axially symmetric deformed nucleus, containing all of the components of its total angular momentum, and their projections onto the respective axes. (Right) The different modes of deformation, governed by the deformation parameter β and the triaxiality γ. The images were obtained and modified from references [21, 24].

A deformed nucleus, using the liquid drop model, has its dimensions modified so that its major axis, a, and minor axis, b, are given by

$$a = R(1+\varepsilon) \tag{2.28}$$

$$b = R(1+\varepsilon)^{-1/2}, \tag{2.29}$$

where ε is a deformation parameter. This, in turn, changes the Coulomb and surface interactions, giving a new binding energy per nucleon

$$\frac{E_B}{A} = a_V - \frac{a_S\left(1+\frac{2}{5}\varepsilon^2\right)}{A^{1/3}} - a_C\frac{Z(Z-1)\left(1-\frac{1}{5}\varepsilon^2\right)}{A^{4/3}} - a_A\frac{(A-2Z)^2}{A^2} - \frac{\delta(A,Z)}{A}. \tag{2.30}$$

Using a quantum mechanical approach, the modified radius R, is modified in terms of the spherical harmonics, given by

$$R = R_0\left[1+\sum_{\lambda=0}^{\infty}\sum_{\mu=-\lambda}^{\lambda} a_{\lambda\mu}Y_{\lambda\mu}(\theta,\phi)\right]. \tag{2.31}$$

λ	Multipolarity	Number of Poles	π	μ
0	Monopole	1	+	0
1	Dipole	2	-	0,±1
2	Quadrupole	4	+	0,±1,±2
3	Octupole	8	-	0,±1,±2,±3
4	Hexadecupole	16	+	0,±1,±2,±3,±4

Table 2.1: A list of the most common multipole moments.

Leading to the *electric multipole moment* of the deformation

$$\mathcal{M}_\lambda = \sum_{k=1}^{Z} r_k^\lambda Y_{\lambda 0}\left(\theta_k\right), \tag{2.32}$$

which describes the nucleus' shape and behaviour, with the number of 'poles' determined by the parameter 2^λ, where λ is the degree of the multipolarity, the parity $\pi = (-1)^\lambda$, and the multipolarity projections $\mu = -\lambda, -\lambda+1, \ldots, \lambda-1, \lambda$. A brief list of the common electric multipole moments of a nucleus is summarised in table 2.1. Assuming the protons are distributed uniformally inside the nucleus, the electric quadrupole moment is given by

$$\mathcal{M}_{\lambda=2} = \sum_{k=1}^{Z} r_k^{\lambda=2} Y_{(\lambda=2)0}\left(\theta_k\right) \approx \frac{3}{4\pi} Z R_0^2 \beta_{\lambda=2}, \tag{2.33}$$

where r_k, θ_k, and ϕ_k are the polar coordinates of the k^{th} proton, $Y_{\lambda 0}$ is a spherical harmonic of the order λ, and

$$\beta_{\lambda=2} = \sqrt{\frac{4\pi}{5}}\varepsilon \tag{2.34}$$

is the quadrupole deformation parameter. This is related to the *intrinsic* electric quadrupole moment

$$Q_0 = \sqrt{\frac{16\pi}{5}}\mathcal{M}_{\lambda=2} \approx \frac{5}{\sqrt{5\pi}} Z R_0^2 \beta_{\lambda=2} \tag{2.35}$$

and can be measured indirectly from, for example, the transitional probabilities (see Gamma Decay, chapter 3, section 3) of photons decaying from these collective states.

Nuclei that purely oscillate between deformed and spherical shapes are considered vibrational, with restoring forces acting on the nucleons in the deformed regions that causes the oscillatory behaviour. Vibrational phonon states can be thought of in analogy

to the vibrational states in molecular crystal structures. Emitted photons from vibrational nuclei have energies in units of $\hbar\omega$. For an ideal vibrator, the excitation energy ratios of the first two excited states in an even-even nucleus, $E(4^+)/E(2^+) = 2$. On the other hand, the excitation energy ratio for a pure rotor is larger, giving a value of $E(4^+)/E(2^+) = 3.33$. This collective behaviour is noted by large increases in the quadrupole transitional probability, $B(E2)$, between these states, compared to nuclei located near or at the proton or neutron magic numbers.

Rotors arise due to the reduction of excitation energies, much lower than the nucleon pairing energy, in even-even nuclei located far from regions containing closed shells. Rotors in odd-A and odd-odd nuclei can behave in similar ways, where the lone nucleon(s) is(are) coupled to the collective 0^+ even-even core of its neighbouring isotone and/or isotope. The Hamiltonian describing the rotation of a deformed nucleus is given by

$$\begin{aligned} H_{rot} &= \frac{\hbar^2}{2\Im}\mathbf{R}^2 = \frac{\hbar^2}{2\Im}(\mathbf{I}-\mathbf{J})^2 \\ &= \frac{\hbar^2}{2\Im}\left(\mathbf{I}^2+\mathbf{J}^2-2K^2-(I_+I_-+I_-I_+)\right), \end{aligned} \tag{2.36}$$

where $\Im$ is the moment of inertia, $\mathbf{R} = \mathbf{I} - \mathbf{J}$ is the rotational angular momentum of the system, $\mathbf{I}$ is the total angular momentum, K is the projection of $\mathbf{I}$ along the symmetry axis, $(I_+I_- + I_-I_+)$ is the coupling term corresponding to the Coriolis force, and $\mathbf{J}$ is the additional angular momentum due to single-particle excitations in odd-A nuclei, or due to nuclear vibrations. Neglecting the Coriolis force coupling, and noting that K and J are constants for a given rotational band, one can obtain the rotational energy eigenvalue as

$$E_{rot} = E_K + \frac{\hbar^2}{2\Im}I(I+1), \tag{2.37}$$

where $I = K, K+1, K+2, \ldots$, and E_K is the energy of the lowest eigenstate of the rotational band, where $I = K$, and is known as the *bandhead*.

Deformed nuclei that have one symmetry axis (axially symmetric) can exist in two different configurations: *oblate* and *prolate*, and a polar plot showing these different modes is shown in figure 2.5. The two important coefficients used to describe this shape, a_{20} and

a_{22}, are given by

$$a_{20} = \beta\cos(\gamma) \tag{2.38}$$

$$a_{22} = \frac{1}{\sqrt{2}}\beta\sin(\gamma), \tag{2.39}$$

where β and γ are the polar coordinates used for the plot. Multiples of $\gamma = 60°$ give non-triaxial shapes, and in the limit $\beta \to 0$, the nucleus becomes spherical.

2.5 The Nilsson Model

A correction to the spherical shell model was made by Nilsson in 1955 in order to describe the properties of deformed nuclei. The method utilised the single particle approach, bound inside an anisotropic harmonic oscillator

$$V(r) = \frac{1}{2}m\left(\omega_1^2x^2 + \omega_2^2y^2 + \omega_3^2z^2\right) - V_0 - 2\alpha_c\left\{\ell(\ell+1) + \frac{3}{4}\right\} - \alpha_s\left\{j(j+1) - \ell(\ell+1) - \frac{3}{4}\right\} \tag{2.40}$$

where each axis is treated independently, i.e. $x \neq y \neq z$, and contains the centrifugal and spin-orbit terms as was discussed prior. For axially symmetric shapes, two directions preserve symmetry (in this case, the x and y components). Neglecting the last two terms, the energy eigenvalues for the Nilsson model are

$$E_{N,n_z} = \left[\left(N + \frac{3}{2}\right) - \varepsilon\left(n_z + \frac{N}{3}\right) + \frac{1}{9}\varepsilon^2\left(N + \frac{3}{2}\right)\right]\hbar\omega_0 - V_0, \tag{2.41}$$

where $N = n_x + n_y + n_z$ is the harmonic oscillator quantum number of the state, with n_z being its z-axis component. Additional quantum numbers are used that remain good for a deformed axially symmetric nucleus:

- The z-axis projection of ℓ, giving $m_\ell = \Lambda$.
- The z-axis projection of s, giving $m_s = \Sigma = \pm\frac{1}{2}$.
- The z-axis projection of j, giving $m_j = \Omega = \Lambda + \Sigma$.
- The parity of the state is $\pi = (-1)^\ell$.

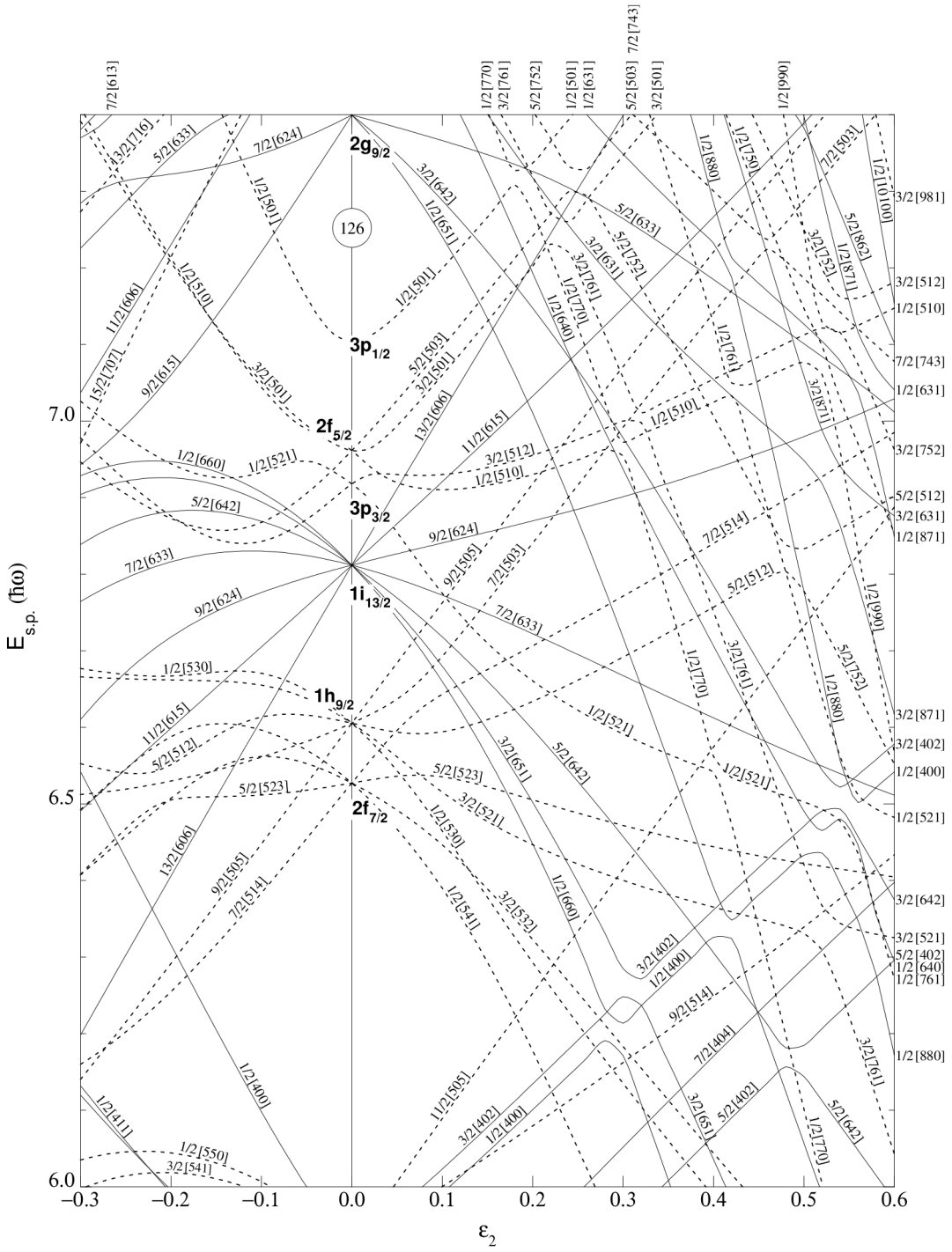

Figure 2.6: The single particle Nilsson model as a function of the quadrupole deformation parameter ε_2, and the hexadecupole parameter, $\varepsilon_4 = -\varepsilon_2^2/6$ for neutrons between the two magic numbers $82 < N < 126$. The single particle energy on the vertical axis is given in MeV. Image taken from [24].

This ultimately leads to the notation used to describe a Nilsson orbital as

$$\Omega^{\pi}\left[Nn_z\Lambda\right]. \tag{2.42}$$

As a consequence, many degeneracies are lifted for non-spherical nuclei, or for $|\varepsilon| > 0$. Difficulties arise when the spin-orbit and centrifugal terms are included in the evaluation; this is due to the quantum numbers Λ and n_z not being constants of motion (i.e. they are no longer "good" quantum numbers), and only become constants again in the limit $\varepsilon \to \infty$, and are therefore called *asymptotic* quantum numbers. Despite this, the same numbers are used in the calculated Nilsson orbitals, which are shown, around the region of interest, in figure 2.6. From this diagram, general features arise from the Nilsson model. Orbits with low values of Ω become more bound in prolate ($\varepsilon > 0$) structures and vice-versa for oblate ($\varepsilon < 0$) structures. Also, at large values of ε, levels with the same n_z move almost parallel to each other, and could be thought of as having pseudo-spin symmetries appearing in the Nilsson model.

2.5.1 Beyond The Nilsson Model

One of the limitations of using this model assumes the fact that the system is treated as a macroscopic system. This causes problems when even the slightest subtleties arise, due to fluctuations or perturbations inside the deformed nucleus. *Strutinsky* [25] proceeded to include microscopic elements to the macroscopic system, by adding the shell model effects to the liquid drop model's binding energy. The result, which was formulated in the late 1960s, allows the nucleus' binding energy and deformation parameters to be calculated to high accuracy; the consequences of this are discussed in more detail under Spontaneous Fission, chapter 3, section 4.

Another method that aimed to calculate the macroscopic behaviour in deformed nuclei using a completely microscopic approach is known as the *cranked shell model* (CSM), which modifies the Hamiltonian of the system in terms of the single-particle and collective

contributions, and is expressed as

$$\hat{H}_{CSM} = \hat{H}_{s.p.} - \hbar\omega J. \tag{2.43}$$

This model also includes rotational forces that have been neglected previously, such as the Coriolis force, as well as the centripetal force. It also takes nuclear pairing into account, which reduces the rotor's moment of inertia, $\Im$; experimental values of $\Im$ give lower values than that of a rigid liquid drop, in which the moment of inertia is given by

$$\Im = \frac{2}{5} m_u A R_0^2 \left[1 + \frac{1}{2}\sqrt{\frac{5}{4\pi}}\beta \right], \tag{2.44}$$

where m_u, A, R and β are the nucleon's mass, the mass number, the nuclear radius and the deformation parameter, respectively. Only two quantum numbers survive in the CSM: The parity $\pi = (-1)^{\ell}$, and the signature, $\alpha_{\pm}$, of the rotational system. For odd-A nuclei, the signature of a given rotational band has two projections of $\pm 1/2$; one such projection has favourability in energy compared to its other state, and their quantum numbers can therefore be written as

$$\alpha_f = \frac{1}{2}(-1)^{j-1/2} \qquad \alpha_u = \frac{1}{2}(-1)^{j+1/2}, \tag{2.45}$$

where α_f and α_u are the favoured and unfavoured signature projections, respectively.

Chapter 3

Nuclear Stability and Radioactive Decay

As with all things in nature, a given system will try its utmost to find a configuration that minimises its total energy, (i.e. relaxing towards its zero-point energy). This is no different for the composite nucleus inside an atom; for certain configurations of protons and neutrons bound together to form stable states, whereas more numerous configurations do not, and undergo a series of transitions that does take this system to the most energetically bound configuration (i.e. minimising the total energy of the system). The types of radioactive decay depends on a multitude of factors, but generally is dictated by a more energetically bound daughter nucleus. Common nuclear transformations are shown in figure 3.1.

While radioactivity was discovered by Becquerel in 1896 [26], it was not for several more years until the scientists were able to categorise different types of decay [27]. Three types of "ray" where discovered: α rays, β rays and γ rays, in which their symbols were originally chosen by the order of which they were discovered. Since then, several other types of radioactive decay have been observed, including some very rare types; details of each are summarised within this chapter.

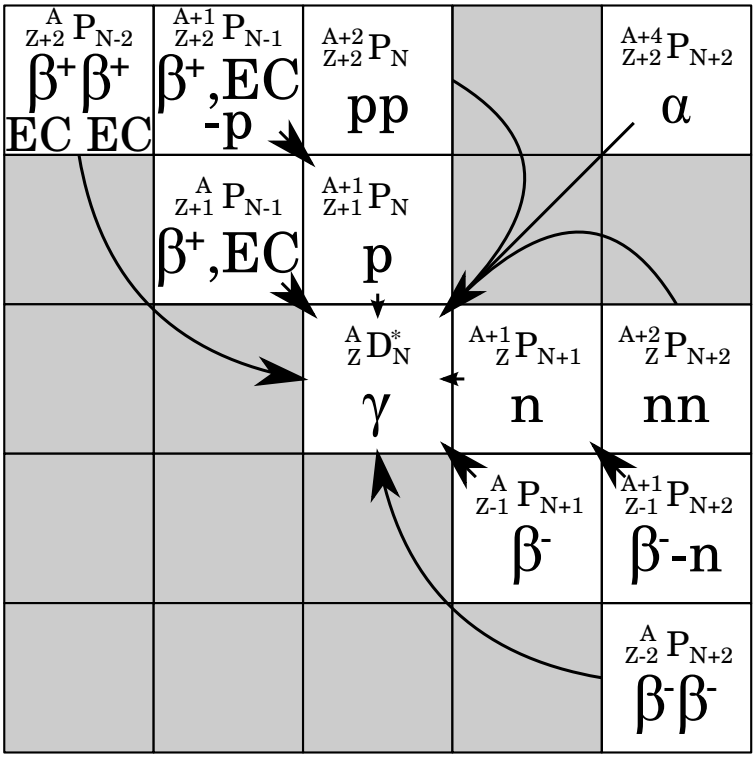

Figure 3.1: An illustration showing, using the standard nuclide chart convention, the disintegration paths of the different decay modes from parent nuclei. The spontaneous fission and cluster decay modes are not shown in this diagram.

3.1 Alpha Decay

The spontaneous emission of a helium ion ($^4_2\mathrm{He}^{++}$, labelled α) from the parent nucleus was the first type of decay to be categorised by Rutherford. It removed two protons and two neutrons from its parent nucleus, which can be imagined as the formation of an α particle within the nucleus before penetrating through the Coulomb barrier known as *quantum tunnelling*, and is governed by the strong force. The reaction of this process can be written as

$$^A_Z X \rightarrow ^{A-4}_{Z-2} Y + \alpha, \tag{3.1}$$

where Z and A are the proton and mass numbers, respectively. The α particle's Q-value, Q_α, neglecting small electron binding energy differences between the parent and daughter nuclei, is given by

$$Q_\alpha = E_B(^{A-4}_{Z-2}Y) - E_B(^A_Z X) + E_B(\alpha)\mathrm{MeV}, \tag{3.2}$$

where $E_B(\alpha) \approx 28.3\text{MeV}$, the binding energy of the α particle. This process can take place when $Q_\alpha > 0$, or

$$E_B({}^{A}_{Z}X) > E_B({}^{A-4}_{Z-2}Y) + 28.3\text{MeV}. \tag{3.3}$$

The Q-value is the contribution of the kinetic energies of the α particle, T_α, and the daughter nucleus, T_D. As the emitted α particles travel non-relativistically ($T_\alpha = 10\text{MeV}$ corresponds to $\beta \approx 0.07c$), classical mechanics can be used as a decent approximation, giving the Q-value relation

$$Q_\alpha = T_\alpha \left[1 + \frac{M_\alpha}{M_D}\right], \tag{3.4}$$

where M_α and M_D are the masses of the α and daughter nuclei, respectively.

An unbound α particle can remain in the confines of the nucleus for a finite time due to the Coulomb potential, which for a two-body system, is written as

$$V(r) = \frac{q_1 q_2}{4\pi\epsilon_0 r}, \tag{3.5}$$

where q_1 and q_2 represent the charges of the first and second particle, respectively, for $r > R$, $R = r_0 A^{1/3}$, the nuclear radius. A square well potential is approximated inside the nuclear radius, arising due to the dominating strong interaction. Using $q_1 = Z_\alpha = 2$, and $q_2 = Z_D$, the barrier height at the nuclear radius, B, is given by

$$B = \frac{2Z_D}{4\pi\epsilon_0 R}, \tag{3.6}$$

and the distance at which the α particle just emerges outside of the potential, b,

$$b = \frac{2Z_D}{4\pi\epsilon_0 Q_\alpha} \tag{3.7}$$

depends on its Q-value, with smaller values leading to a greater barrier thickness. Assuming this is the case for all α decays ($r_0 A^{1/3}/b \ll 1$), the decay constant, λ_α, is the product of the barrier penetration probability P and the frequency of the α particle collisions, f,

with the inside of the potential well. Using the above assumptions, the decay half-life results in

$$T_{1/2} = \frac{\ln(2)}{\lambda_\alpha} = \frac{\ln(2)}{fP} = \frac{\ln(2)R}{v_{in}} \exp\left(\frac{Z_D e^2}{\epsilon_0 \hbar v} - \frac{4e}{\hbar}\sqrt{\frac{Z_D m R}{\pi \epsilon_0}}\right), \tag{3.8}$$

where v_{in}, v and m are the α particle's internal velocity, its ejected velocity, and its reduced mass, respectively. Replacing v as

$$v = \sqrt{\frac{2Q_\alpha}{m}}, \tag{3.9}$$

one can write the half-life in terms of the Geiger-Nutall law of α decay

$$\log_{10} T_{1/2} = a + \frac{b}{\sqrt{Q_\alpha}}, \tag{3.10}$$

which is an empirically determined formula, with the coefficients a and b determined based on the α decay data that was available in the early 1910s. Given these limitations, the formula had reproduced the measured decay half-lives of nuclei with remarkable accuracy, and shows the strong dependence of the energy Q-value of the α particle.

Figure 3.2 illustrates the Geiger-Nutall's law of α decay, along with the potential well used to evaluate the calculation of $T_{1/2}$. The dashed line above includes an additional effect that is due to centrifugal effects, resulting in the total potential to become

$$V(r) = \frac{2Z_D e^2}{4\pi\epsilon_0 r} + \frac{\ell(\ell+1)\hbar^2}{2mr^2}. \tag{3.11}$$

As the helium nucleus has a ground state of 0^+, in order for a parent isotope to decay into a state of the daughter isotope that has a different spin, $\Delta j = |j_i - j_f| \neq 0$, the α particle must carry away the excess angular momentum, which requires the nucleus to form in that excited state. This consequently *hinders* the decay process, and is expressed in terms of an increased barrier thickness. The above correction to the Coulomb potential does not take into account of parity conservation during the decay event. For odd values of ℓ, a change of parity is required, further hindering the α decay process. Finally, the α

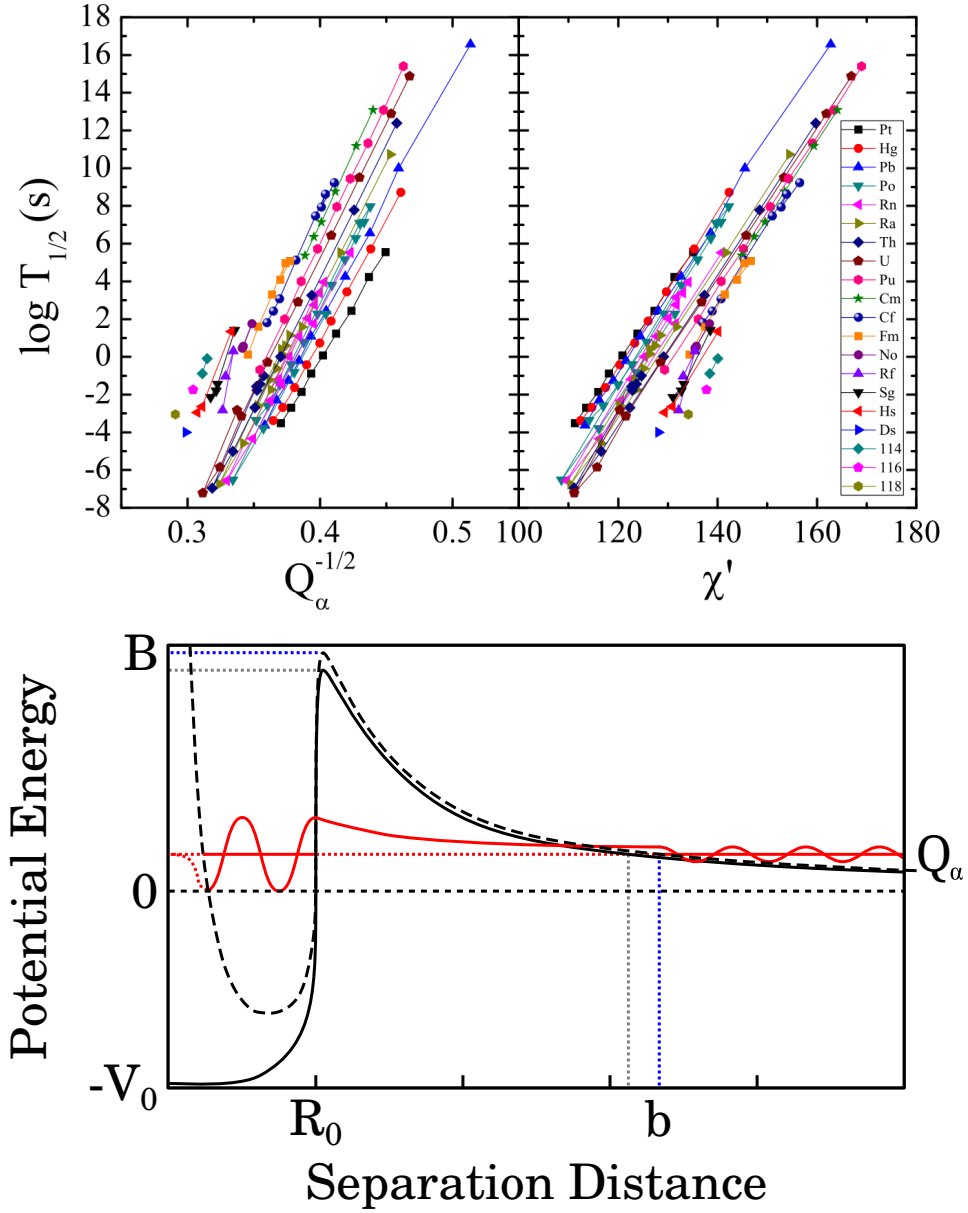

Figure 3.2: (Top left) α Q-value systematics plot as a function of the logarithm of the decay's half-life, for even-even nuclei for $Z \geq 78$. The relationship that Geiger-Nuttall deduced empirically can be clearly seen here. (Top right), as with the top left, but the x-axis coordinate now set to $\chi' = Z_1 Z_2 \sqrt{A/Q_\alpha}$. The graphs were taken from reference [28]. (Bottom) A schematic of an unbound α particle inside the nucleus, which tunnels through the Coulomb potential and centrifugal barrier (if $\Delta\ell > 0$) and is ejected from the nucleus.

decay process favours transitions that give the largest value of Q_α.

3.2 Beta Decay and Electron Capture

Historically the second type of discovered "ray", β decay originally assumed the emission of electrons from the parent nucleus only. Unlike α decay, where the particles have characteristic decay energies, β decay produces a continuous spectrum of kinetic energies, $0 < E_\beta < Q_\beta$, where the maximum energy is the decay's Q-value. Questions were asked as to why the electron did not carry away all of the energy in the decay process; given that the nucleus was also understood to contain no electrons, the apparent creation of electrons inside the nucleus became an enigma for many a scientist. Pauli in 1930 suggested that the remaining energy was carried away in a second particle; electrically neutral and fermion in nature, it was labelled the *neutrino*. It was not until the Cowan-Reines neutrino experiment, performed in 1953 [29], confirmed its existence.

The creation of the electron is governed by the weak interaction; upon the discovery of constituent quarks that make up the protons and neutrons in atoms (and by extension, all other hadrons), β decay could be described as the transformation from one quark flavour to another inside the hadron. Depending on the type of transition, either the process results in the emission of an electron and anti-neutrino (β^-), or in the emission of a positron and neutrino (β^+). In the simplest example, the free neutron, consisting of two down and one up quarks (udd), undergoes β^+ decay, and the hadron is transformed into a proton (uud) in the reaction

$$n \rightarrow p + e^- + \bar{\nu}_e. \tag{3.12}$$

In a more general case, isotopes containing an excess number of neutrons can undergo β^- decay, transforming the nucleus with the process given by

$${}^A_Z X_N \rightarrow {}^A_{Z+1} Y_{N-1} + e^- + \bar{\nu}_e. \tag{3.13}$$

Neglecting the small electron binding energy differences between the parent and daughter

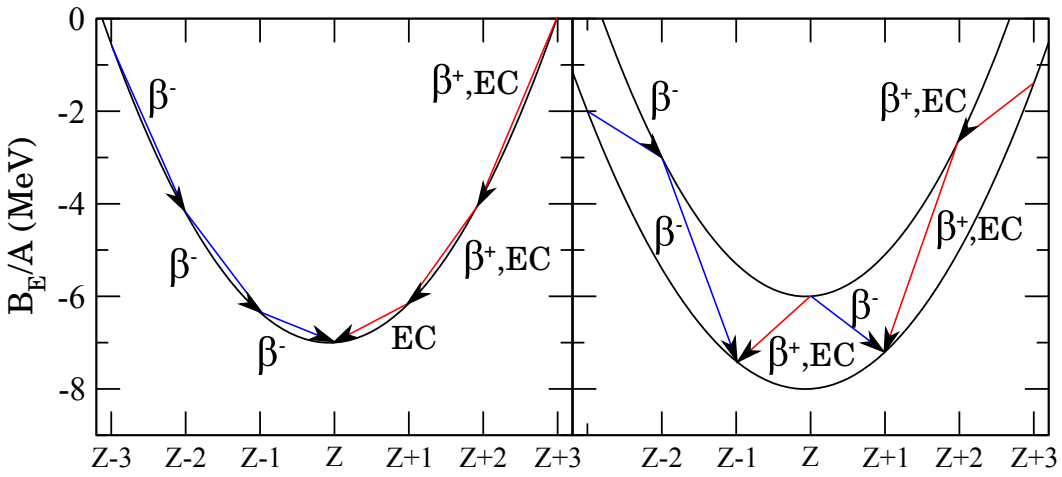

Figure 3.3: A typical decay path for nuclei undergoing β decay for odd-mass (left), and even-mass (right) isotopes. The pairing contribution gives two "valleys" for the even-mass isotopes; the less bound parabola arises from an odd proton and neutron, compared to the more bound configuration, where all nucleons are paired. The *valley of β stability* corresponds to the minimum for each curve, where the nucleus is unable to undergo β decay any further (with the exception of $\beta\beta$ decay).

nuclei, the Q-value of this decay is given by

$$\begin{aligned} Q_{\beta^-} &= M\left({}^{A}_{Z}X_N\right)c^2 - Zm_ec^2 - M\left({}^{A}_{Z+1}X_{N-1}\right)c^2 + (Z+1)m_ec^2 - m_ec^2 \\ &= M\left({}^{A}_{Z}X_N\right)c^2 - M\left({}^{A}_{Z+1}X_{N-1}\right)c^2. \end{aligned} \tag{3.14}$$

Similarly, nuclei with excess numbers of protons undergo β^+ decay, with the process written by

$${}^{A}_{Z}X_N \rightarrow {}^{A}_{Z-1}Y_{N+1} + e^+ + \nu_e, \tag{3.15}$$

along with the decay Q-value

$$\begin{aligned} Q_{\beta^+} &= M\left({}^{A}_{Z}X_N\right)c^2 - Zm_ec^2 - M\left({}^{A}_{Z-1}X_{N+1}\right)c^2 + (Z-1)m_ec^2 - m_ec^2 \\ &= M\left({}^{A}_{Z}X_N\right)c^2 - M\left({}^{A}_{Z-1}X_{N+1}\right)c^2 - 2m_ec^2, \end{aligned} \tag{3.16}$$

requiring an energy difference, between the parent and daughter nuclei, of at least double the electron's rest mass, or $2m_e \approx 1.022\text{MeV/c}^2$.

In situations that this condition is not satisfied, the nucleus may only decay via a method known as *electron capture*, in which a deeply bound atomic electron is captured

by the nucleus, releasing a neutrino in the process:

$$ {}^{A}_{Z}X_N + e^- \rightarrow {}^{A}_{Z-1}Y_{N+1} + \nu_e. \tag{3.17} $$

In this scenario, the Q-value of the process

$$ \begin{aligned} Q_{EC} &= M\left({}^{A}_{Z}X_N\right)c^2 - (Z-1)m_e c^2 - M\left({}^{A}_{Z-1}X_{N+1}\right)c^2 + (Z-1)m_e c^2 - E_B(e^-) \\ &= M\left({}^{A}_{Z}X_N\right)c^2 - M\left({}^{A}_{Z-1}X_{N+1}\right)c^2 - E_B(e^-), \end{aligned} \tag{3.18} $$

requires a much lower energy difference than β^+ decay. $E_B(e^-)$ is the atomic binding energy of an electron in the parent nucleus that is captured; the most likely event takes place for states where the electron is more likely to be found inside the nucleus (i.e. the most deeply bound electron orbitals). This decay mode can still compete with β^+ decay if the Q-value is large enough to permit both processes. Figure 3.3 illustrates the decay process for a given isobar, whereby the optimum ratio of protons and neutrons is reached. For odd A isobars, there is only one β-stable nuclide, whereas even A, due to the pairing interaction differences between even-even and odd-odd nuclei, can have two or three β-stable nuclides. All of the presented three modes assumes that the neutrino is massless; recent experiments, however, suggest that these leptons actually have non-zero mass [30].

Unlike the α particle, which exhibits behaviour that of a boson particle, favouring the 0^+ ground state configuration, both the $\beta^{\pm}$ and (anti-)neutrino particles are fermions, and have spins of $1/2\hbar$; this makes calculating the transformation rates complicated. In brief, both fermions can be thought of a superposition of two quantum states, characterised by their spin projection, to give the total spin of the system, $\mathbf{S}_\beta$, and can form either a singlet or triplet state. Decay events are considered *allowed* when no angular momentum, $\mathbf{L}_\beta = 0$, is carried away from the parent nucleus, making these processes unhindered. Forbidden transitions take place when the decay products must also carry away angular momentum from the parent nucleus; the degree of forbiddeness depends on the amount of changed angular momentum $\mathbf{L}_\beta = n$ and parity change $\pi = (-1)^n$ between the parent and daughter nuclei; transitions of larger differences further prohibits the decay to take

place.

3.3 Gamma Decay

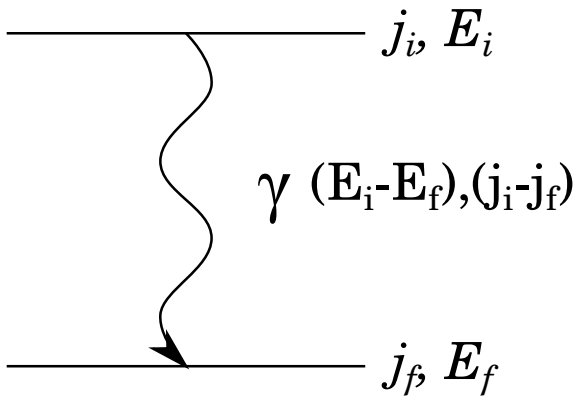

Figure 3.4: A brief description of γ decay, showing the de-excitation of a state with energy E_i and angular momentum j_i, to a less energetic state of energy E_f and angular momentum j_f. A photon carries away the excess energy, $\Delta E = E_i - E_f$, and angular momentum, $\Delta j = j_i - j_f$, from the nucleus.

The third type of "ray" to be originally categorised, γ decay involves the emission of photons from the parent nucleus. This process does not change the number of protons or neutrons in the nucleus, but it does arise due to the perturbations of the nuclear charge and current distribution. The sequence can be written as

$$ {}^{A}_{Z}Y^{*} \rightarrow {}^{A}_{Z}Y + \gamma, \tag{3.19} $$

where the Q-value of the transition, neglecting the recoiling energy of the nucleus, is simply equal to the energy of the photon, $Q_\gamma = E_\gamma$. It is this process that removes excess excitation energy inside the nucleus until it has reached its most bound configuration, (i.e. the ground state). An example of this de-excitation is shown in figure 3.4.

As γ rays are a form of electromagnetic radiation, they can be described by its multipolarity λ, similar to the descriptions that describes the rotational or vibrational behaviour of a collective nucleus. γ rays may give rise to magnetic or electric transitions, depending on whether the de-excitation of the nucleus is either single-particle or collective behaviour, respectively. As excited states in a given nucleus are non-stationary, time-dependent

methods must be employed in order to determine transition rates between the initial ($|i\rangle = |I_i M_i\rangle$) and final ($|f\rangle = |I_f M_f\rangle$) states. Fermi's golden rule gives this description, and is given by

$$\frac{1}{\tau}_{i\to f} = \frac{2\pi}{\hbar} |\langle I_f M_f | H'_{\lambda\mu} | I_i M_i \rangle|^2 \rho, \tag{3.20}$$

where ρ is the density of final states and μ is the multipolarity projection of λ. The matrix element of this equation depends on the spin and magnetic substates (i.e. the orientation) quantum numbers; in order to separate these two quantities, the Wigner Eckart Theorem allows the matrix element to be expressed as

$$\langle I_f M_f | H\prime_{\lambda\mu} | I_i M_i \rangle = (2I_f + 1)^{-1/2} \langle I_i M_i \lambda\mu | I_f M_f \rangle \langle I_f | |H'_\lambda| | I_i \rangle , \tag{3.21}$$

where the *reduced* matrix element, $\langle I_f | |H'_\lambda| | I_i \rangle$, only contains the intrinsic nuclear property, removing the dependency of the magnetic quantum numbers, which make up inside the "Clebsch-Gordon" coefficient term $\langle I_i M_i \lambda\mu | I_f M_f \rangle$. This leads to the reduced transition probability

$$B(H'_\lambda; I_i \to I_f) = \frac{1}{(2I_i + 1)} |\langle I_f | H'_\lambda | I_i \rangle|^2, \tag{3.22}$$

for $M_f = M_i + \mu$ and $|I_f - I_i| \leq \lambda \leq I_f + I_i$. The transition rate from an initial to final state of a given multipolarity is given by

$$\frac{1}{\tau}(H'_\lambda) = \frac{8\pi(\lambda + 1)}{\hbar\lambda \left([2\lambda + 1]!!\right)^2} \left(\frac{E_\gamma}{\hbar c}\right)^{2\lambda+1} B(H'_\lambda). \tag{3.23}$$

Table 3.1 shows the calculated transition rates for electric and magnetic multipoles ($E\lambda$,$M\lambda$) in terms of the reduced transition probability and the photon energy, given in MeV. Assuming that these transitions are of single-particle in nature, and take place within a uniform charge density, Weisskopf calculated the reduced transition probabilities for different transition multipolarities. The Weisskopf transition rates and single particle strengths can be expressed in terms of *Weisskopf units*, or W.u.

Multipolarity	$1/\tau$	Units
E1	$1.59 \times 10^{15} \cdot E_\gamma^3 \cdot B(E1)$	$e^2\text{fm}^2$
E2	$1.225 \times 10^{9} \cdot E_\gamma^5 \cdot B(E2)$	$e^2\text{fm}^4$
E3	$5.708 \times 10^{2} \cdot E_\gamma^7 \cdot B(E3)$	$e^2\text{fm}^6$
M1	$1.758 \times 10^{13} \cdot E_\gamma^3 \cdot B(M1)$	μ_N^2
M2	$1.355 \times 10^{7} \cdot E_\gamma^5 \cdot B(M2)$	$\mu_N^2\text{fm}^2$
M3	$6.313 \cdot E_\gamma^7 \cdot B(M3)$	$\mu_N^2\text{fm}^4$
Multipolarity	**$B(E/M\lambda)_W$**	**$1/\tau$ (s^{-1})**
E1	$0.0645 \cdot A^{2/3} \cdot e^2\text{fm}^2$	$1.025 \times 10^{14} \cdot E_\gamma^3 \cdot A^{2/3}$
E2	$0.0594 \cdot A^{4/3} \cdot e^2\text{fm}^4$	$7.276 \times 10^{7} \cdot E_\gamma^5 \cdot A^{4/3}$
E3	$0.0594 \cdot A^{2} \cdot e^2\text{fm}^6$	$3.339 \times 10^{1} \cdot E_\gamma^7 \cdot A^{2}$
M1	$1.79 \cdot \mu_N^2$	$3.148 \times 10^{13} \cdot E_\gamma^3$
M2	$1.65 \cdot A^{2/3} \cdot \mu_N^2\text{fm}^2$	$2.236 \times 10^{7} \cdot E_\gamma^5 \cdot A^{2/3}$
M3	$1.65 \cdot A^{4/3} \cdot \mu_N^2\text{fm}^4$	$1.042 \times 10^{1} \cdot E_\gamma^7 \cdot A^{4/3}$

Table 3.1: The calculated transition rates (top), along with the Weisskopf estimates (bottom), for the most common multipole γ transitions.

3.3.1 Internal Conversion

Photons have no electric charge, and have an intrinsic spin of 1 $\hbar$. It is this latter property that forbids any monopole transition that can take place between two 0^+ states, resulting in a net change of zero angular momentum, or $\Delta J = 0$. This transition can proceed by a process known as *internal conversion*, where the nucleus exchanges this excess energy with one of the deeply bound atomic electrons, or by pair production, for energies larger than twice the electron's rest mass, or 1.022MeV. The interaction probability of a given atomic shell depends on the wavefunction overlap of the bound electron over the dimensions of the nucleus. Since the K-shell has the biggest wavefunction overlap, the conversion electrons are most likely to have emanated from this state. If the energy between the two nuclear states exceeds that of the atomic shell binding energy, the following reaction takes place:

$$ {}^{A}_{Z}Y^* \rightarrow {}^{A}_{Z}Y + e^- + K_{\alpha,\beta,\ldots}L_{\alpha,\beta,\ldots}\ldots, \tag{3.24} $$

where a cascade of X-rays take place following the interaction process, due to the remaining atomic electrons filling the new shell vacancies. The kinetic energy of the emitted electron

is given by

$$T_{e^-,IC} = E_i - E_f - E_B(e^-_{IC}), \tag{3.25}$$

where E_i, E_f and $E_B(e^-, IC)$ are the initial and final nuclear states, and the binding energy of the converted electron, respectively. There is also the possibility for the emission of *Auger electrons* to be emitted instead of the X-rays, where the kinetic energy of these electrons is given by

$$T_{e^-,Auger} = E(K_{\alpha,\beta,\ldots}L_{\alpha,\beta,\ldots}\ldots) - E_B(e^-_{Auger}). \tag{3.26}$$

The production of Auger electrons dominates in light nuclei and decreases with increasing Z, with X-rays starting to dominate at $Z > 30$ [31].

Internal conversion, not only does it takes place for $\Delta J = 0$ transitions, but is in competition with γ decay, especially for high multipolarity transitions, taking place within heavy nuclei. Pair production also starts to dominate at energies around 10MeV. For lower energy transitions, pair production can be ignored. For the two remaining decay modes, the ratio of the total number of converted electrons, $I(e_{K,L,M,\ldots})$, to the number of photons arising from γ decay, I_γ, is given by the *internal conversion coefficient*:

$$\alpha_{ICC} = \frac{I(e_{K,L,M,\ldots})}{I_\gamma}. \tag{3.27}$$

An alternative way of measuring the internal conversion coefficient is by measuring the intensity ratio between the emitted X-rays and the γ radiation. For K-shell ionisation, this is written as

$$\alpha_{ICC,K} = \frac{I(K_{\alpha,\beta,\ldots})}{I_\gamma \omega_K}, \tag{3.28}$$

where ω_K is the *X-ray fluorescence yield*, and can vary between purely Auger electron dominated ($\omega_K = 0$) to purely fluorescent ($\omega_K = 1$). For purely converted transitions, $\alpha_{ICC} = \infty$, whereas pure γ decay gives the other extreme $\alpha_{ICC} = 0$; a value of 1 corresponds to a 50% branching ratio for either decay mode.

3.4 Spontaneous Fission

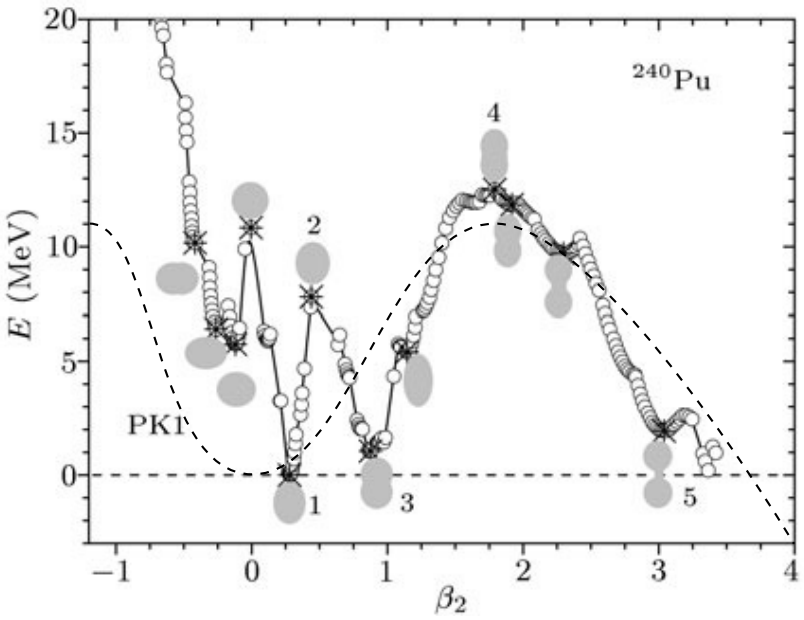

Figure 3.5: An example of the fission process of heavy nuclei using the liquid drop model (dashed lines) and when including shell model effects (solid line), which was obtained from [32]. In the latter, the potential minima takes place at non-zero nuclear deformation, with the possibility of a secondary, isomeric state of larger deformation. The liquid drop model, on the other hand, favours sphericity, unless $Z^2/A > 49$, where it undergoes prompt fission.

The splitting, or fissioning, of heavier nuclei into two smaller fragments is a consequence of large coulomb repulsion effects, coupled with large nuclear deformations located in mid-shell regions. The mass distribution of the two fission fragments can either be symmetrical, or asymmetrical, and depends on the fissioning parent nucleus. The liquid drop model predicts that fissioning becomes possible when $Z^2/A > 49$. This is most prominently observed in the actinide and trans-actinide (superheavy) elements.

Figure 3.5 shows the potential well for a liquid drop, as a function of the deformation parameter ε. The binding energy for a deformed liquid drop, expressed in Nuclear Deformation (chapter 2, section 4), suggests that the nucleus is always spherical, until a point is reached (i.e. $Z^2/A > 49$) where the nucleus will fission immediately, which is most certainly not the case for real nuclei. The Strutinsky method was employed, described in Beyond The Nilsson Model (chapter 2, section 6). The consequence of this method more accurately reproduces the behaviour of deformed nuclei, where states bound inside

the potential well may undergo nuclear fission via barrier penetration; the transition rate is also dictated by the barrier thickness. In certain configurations, for example ^{240}Pu[32], the nuclear potential contains two minima; a second, more deformed, isomeric state can be populated from nuclear excitations.

3.5 Proton and Neutron Emission

From the point of view of the liquid drop model, adding protons or neutrons to a stable nucleus, will in turn affect the overall Coulomb and asymmetry contributions to its binding energy. Adding neutrons reduces the Coulomb repulsive effects, at the expense of the nucleus' asymmetry; stable nuclei, of medium to heavy masses, become neutron rich, in order to balance these two contributions, maximising its nuclear binding energy. In scenarios where a nucleus has so many excess protons or neutrons, giving rise to large Coulomb or asymmetry repulsive effects, respectively, the ability of *spontaneous* drip-line decay can take place. This is expressed in terms of *proton emission*:

$$ {}^{A}_{Z}X_N \rightarrow {}^{A-1}_{Z-1}Y_N + {}^{1}_{1}p, \tag{3.29} $$

and in terms of *neutron emission*:

$$ {}^{A}_{Z}X \rightarrow {}^{A-1}_{Z}Y_{N-1} + {}^{1}_{0}n, \tag{3.30} $$

where these processes can only take place when the Q-value of the reaction, $Q_{n,p}$, satisfies the condition

$$ \begin{aligned} Q_n &= M\left({}^{A}_{Z}X_N\right)c^2 - M\left({}^{A-1}_{Z}X_{N-1}\right)c^2 - m_n c^2 > 0 \\ Q_p &= M\left({}^{A}_{Z}X_N\right)c^2 - M\left({}^{A-1}_{Z-1}X_{N}\right)c^2 - m_p c^2 > 0, \end{aligned} \tag{3.31} $$

and can be interpreted as a negative *separation energy*, $S_{n,p}$, where

$$ S_{n,p} = -Q_{n,p}. \tag{3.32} $$

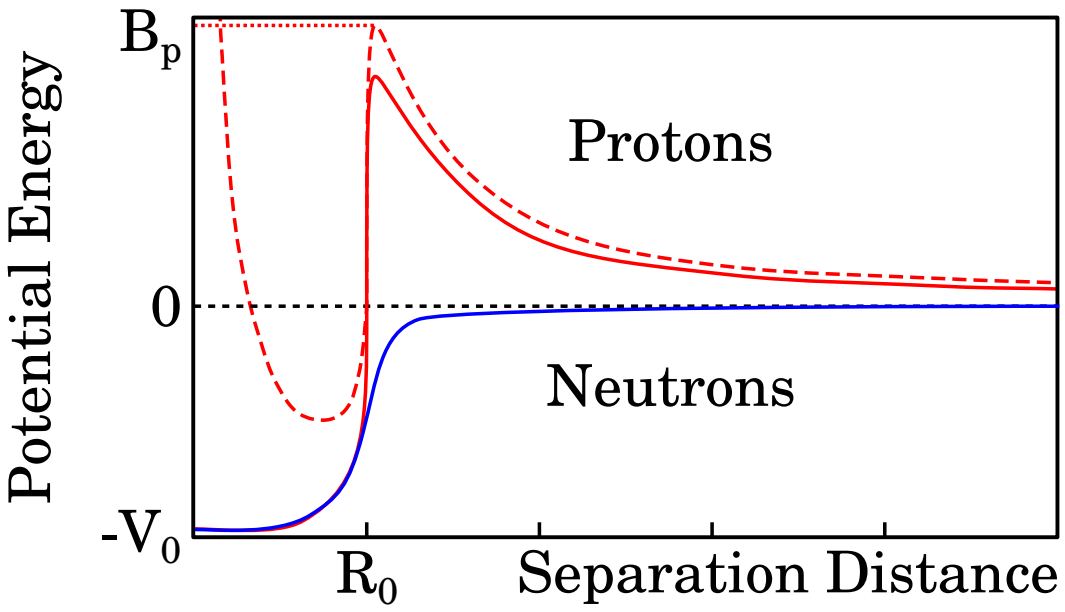

Figure 3.6: The nuclear potential experienced by the outermost bound proton (red) or neutron (blue), along with centrifugal contributions for non-zero $\Delta\ell$ transitions for proton emission.

The unbound neutron in the nucleus does not experience the effects of the Coulomb potential inside the nucleus. Consequently, even a slightly unbound neutron feels the repulsive strong force acting upon it. The neutron escapes its parent nuclide in very short time scales of the order of 10^{-21} seconds.

The unbound proton, on the other hand, does feel the Coulomb potential, as well as the centrifugal barrier, allowing the possibility to perform detailed spectroscopy of these nuclei. Like α decay, the unbound proton, with a Q-value less than the potential barrier's height, must tunnel through it before it is emitted from the parent nucleus. In addition, a similar empirical formula, known as the Viola-Seaborg formula [33], given by

$$\log_{10} T_{1/2(reduced)} = \frac{aZ+b}{\sqrt{Q_p}} + cZ + d|\beta_2^3| + h_i \tag{3.33}$$

was used to estimate the half-life of proton emission. For unhindered decays ($h_i = 0$), the parameters $a = 0.3993$, $b = -0.3510$, $c = -26.9276$, and $d = 0$ were determined empirically for spherical nuclei [34]. The reduced half-life is described by the emission of the proton when neglecting centrifugal effects. The total half-life for transitions requiring

non-zero $\Delta\ell$, is given by

$$\log_{10} T_{1/2(reduced)} = \frac{\log_{10} T_{1/2}}{\exp\left(\frac{2\hbar\ell(\ell+1)}{\sqrt{2\mu Q_p R_C^2}} \cdot \sqrt{\frac{R_C}{R_t}\left(1 - \frac{R_t}{R_C}\right)}\right)}, \tag{3.34}$$

where $\mu = m_p M_D/(M_p + M_D)$, $R_C \approx Z_1 Z_2 e^2/4\pi\epsilon_0 Q_p$, and $R_t = 1.225(1 + A_D^{1/3})$fm are the reduced mass of the proton-daughter system, the classical turning point of a particle with energy Q_p, and the touching radius, respectively. The nuclear potential experienced for each type of drip-line decay is shown in figure 3.6.

3.6 Rare Decay Events

Other types of decay from radionuclides exist, but the probability of them happening are extremely low by comparison. *Double beta decay*, $\beta\beta$ for example, concerns the simultaneous emission of two β particles, as well as two (anti-)neutrinos. While this process can take place in competition with regular β decay, the latter decay process wins out, due to its much larger transition probability. Exceptions of this are for select nuclei where single β are forbidden due to negative Q-values, while $\beta\beta$ decays give positive Q-values, and are thus allowed. The transition for $\beta\beta$ decay can be written as

$${}^{A}_{Z}X \rightarrow {}^{A}_{Z\pm2}Y_{N\mp2} + 2e^{\mp} + 2\bar{\nu}_e, 2\nu_e. \tag{3.35}$$

This has only been observed for eleven radio-isotopes [30], with very long half-life measurements varying between 10^{18} to 10^{24} years. *Neutrino-less* double β decays, where only two electrons or positrons are emitted from the parent nucleus, are an even more exotic form of the weak interaction process; no evidence of this decay mode has been observed thus far.

Cluster decay is the general form of radioactive decay where-by a smaller nucleus (larger than ^{4}He) inside a larger one is formed, before tunnelling through the Coulomb barrier, leaving its parent nucleus behind. Like α decay, cluster decay is governed by the strong interaction, and favours producing daughter nuclei near or at shell closures (*i.e.* magic

numbers of neutrons and/or protons), where the Q-value is maximised. The measured branching ratios, relative to α decay, varies per nuclide, but has not been found to be larger than 10^{-5}, and are normally around the order of $10^{-13\pm3}$ [35], making this decay mode extremely rare.

Chapter 4

Experimental Procedure

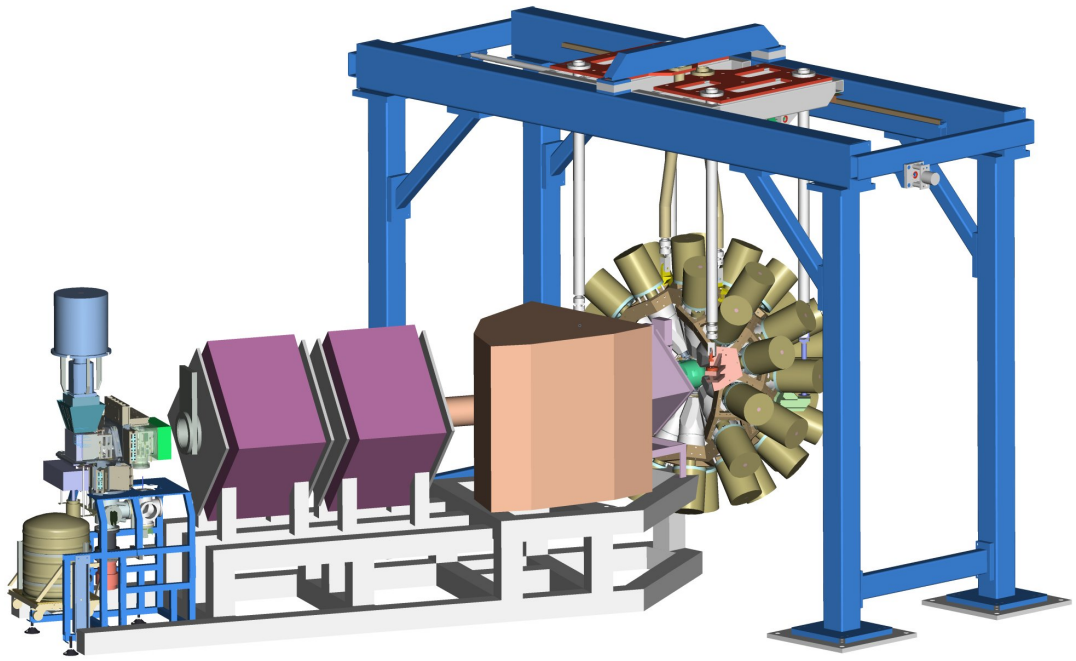

Figure 4.1: Rendered drawing of the experimental setup, showing (from right to left) JUROGAM and its supporting frame and mobile carriages, the gas-filled RITU separator and focal plane spectrometer array GREAT. This image shows the previous JUROGAM array; it was upgraded in 2008 to JUROGAM II, which saw the replacement of the central rings' Phase-I crystal detectors with clover detectors. The beam travels from right to left, reacts with the target located in JUROGAM II, and is then transported through RITU into GREAT. Image credit: Dave Seddon (University of Liverpool).

Experimental Length (hours)	^{92}Mo Thickness (mg/cm^2)	E_{beam} (MeV)	I_{beam} (pnA)	Measured β_{recoil}	Interested Nucleus
34	0.50	392	7.0	0.0442(3)	^{173}Pt
92	0.60	392	7.2	0.0438(3)	^{173}Pt
85	0.60	400	8.9	0.0441(2)	^{173}Hg
48	1.15	400	6.0	0.0431(5)	^{173}Hg

Table 4.1: A summary of the beam and target properties used in this experiment. The main focus of this experiment was to maximise production of two isobars ^{173}Hg and ^{173}Pt; although a sizeable amount of ^{173}Au was produced, the beam energy was not optimised for its production.

A fusion-evaporation experiment was performed at the University of Jyväskylä Accelerator Laboratory, Finland, for a total beam duration of 259 hours. The setup utilised JUROGAM II, an array of detectors surrounding the target chamber; RITU, a gas filled recoil mass separator; GREAT, an array of detectors located at the focal plane. The whole experimental setup is shown in figure 4.1. Details of these instruments are explained later in this chapter. All of the detectors are independently read out using the triggerless data acquisition system (see Total Data Readout, section 6 of this chapter). A ^{92}Mo target, isotopically enriched to 98%, was mounted onto the target frame inside the chamber. Neutral atoms of the beam material ^{84}Sr had 16 of its electrons stripped off inside the Electron Cyclotron Resonance Ion Source (ECRIS) facility, giving it an ionic charge state of $q = +16e$ per atom. The ions were then accelerated inside the K130 cyclotron, before they were focused and directed onto the ^{92}Mo target in the RITU experimental cave.

During the experiment, different target thicknesses and beam kinetic energies were used, in order to optimise production cross-sections for several nuclei of interest – a summary of these parameters are shown in table 4.1.

4.1 Nuclear Reactions

Probing the most exotic configurations of nuclei far from stability allows the testing of current nuclear theories on how the structure of the nucleus behaves in extreme regions of the Segrè chart. However, there are significant experimental challenges in order to

synthesise these nuclei, and to perform detailed spectroscopy on them. Different nuclear reactions have been employed, depending on how far the nucleus of interest is located from stability, the available facilities, as well as the properties of the nucleus of interest that wished to be measured. Experiments where the production cross section is particularly low (< 10nb) must run for days, even weeks, at a time in order to obtain enough decay statistics for those nuclei. In any case, these reactions involve bombarding a beam of ions, which one will denote the symbol A, into a target material, B, to produce a compound formation, C, along with any evaporated particles that de-excite this formation, D. This can be written as the following reaction

$$A + B \longrightarrow C + D. \tag{4.1}$$

One of the main factors that dictate the kind of reaction that takes place is the impact parameter R_L, the minimum radius achieved of a given ion-target interaction. It depends on the projectile's offset parameter b_{gr}, the projectile's kinetic energy, and the strength of the repulsive Coulomb potential between the ion and the target. A small value of R_L corresponds to very close collisions with the target nucleus (which would be the most likely candidate for nuclear fusion to take place), whereas large values of R_L are the opposite, with reactions taking place being either elastically scattered or undergo Coulomb excitations (Coulex) to the target nucleus. Intermediate values of R_L allows the projectile to become close enough to the target nucleus so that nucleons are transferred between the two. An illustration of these different scenarios of nuclear interaction is shown in figure 4.2.

In order for the projectile to reach a distance close enough to the target nucleus to undergo nuclear transformation, it must have sufficient kinetic energy to overcome the repulsive force due to the Coulomb potential of the ion-target system. The repulsive potential barrier due to the atomic electrons is first considered. The electric potential, V, between a travelling beam particle and a particle located in the target material is given by

$$V = \frac{q_1 q_2}{4\pi\epsilon_0 R}, \tag{4.2}$$

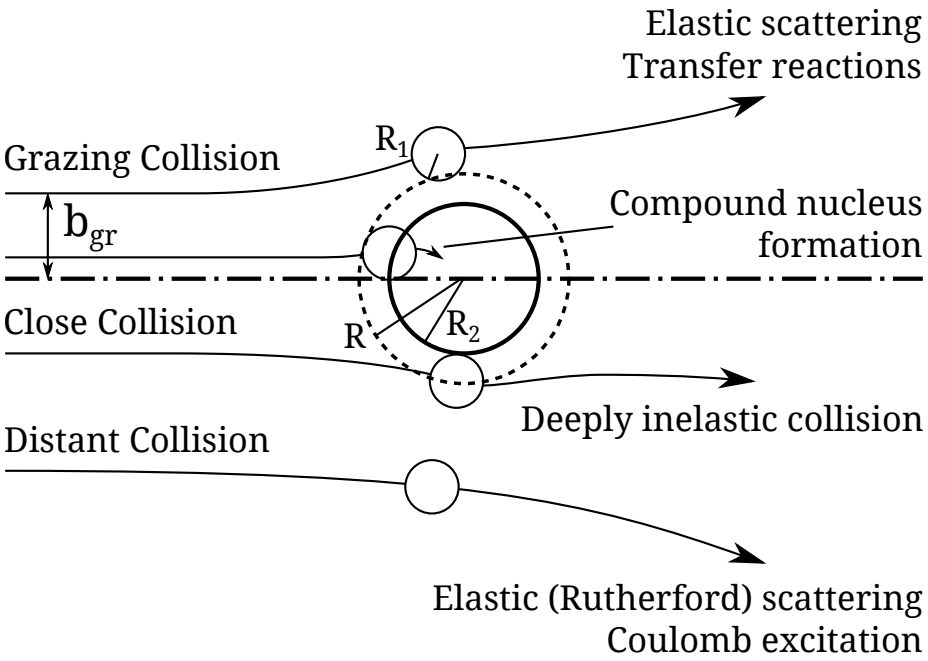

Figure 4.2: Illustration of the various different kinds of nuclear interaction that takes place in ion-beam reactions. Close and grazing collisions (where the parameter b_{gr} is small) can only take place if the ion's kinetic energy is enough to overcome the Coulomb potential at the combined radius ($R = R_1 + R_2$) of the ion-target system. Image modified from [36].

where q_1 and q_2 represent the electric charges of the beam projectile and target particle, respectively, and R is the radial distance between the two charges. As the projectiles must travel through the electron orbits before interacting with the nucleus, the Coulomb potential barrier due to the atomic electrons in the ion-target system has been estimated. Assuming that half of the total number of electrons have been stripped off from the projectiling atom, the reaction is symmetric ($Z_1 \approx Z_2 \approx Z$) and populates heavy mass compounds ($Z_1 + Z_2 \approx 80$), and the atomic Coulomb potential is at its maximum when the ion-target separation distance is equal to double the Bohr's radius $R = R_1 + R_2 = 2a_0$, where

$$a_0 = \frac{4\pi\epsilon_0\hbar^2}{m_e e^2} \approx 52.9\text{pm}, \tag{4.3}$$

one can estimate the atomic Coulomb potential barrier of the ion-target system to give

$$\begin{aligned} V_{atomic} &= \frac{0.5Z^2e^2}{8\pi\epsilon_0 a_0} \\ &\approx 11\text{keV}. \end{aligned} \tag{4.4}$$

This is compared to the Coulomb potential due to the protons inside the nuclei of the projectile and the target. Using the nuclear radius relation $R = 1.2 + 1.16A^{1/3}$ fm from Bohn *et al.* [37], where A is the mass number of the nucleus, and making the same assumptions as above, one gets the Coulomb potential due to proton repulsion to be

$$\begin{aligned} V_{nuclear} &= \frac{Z_1 Z_2 e^2}{4\pi\epsilon_0(2.4 + 1.16(A_1^{1/3} + A_2^{1/3})) \times 10^{-15}} \\ &\approx 180\text{MeV}. \end{aligned} \tag{4.5}$$

The repulsive contribution due to the atomic electrons in the ion-target system is negligible when compared to the contribution due to the protons in both nuclei. The corresponding minimum kinetic energy for a successful nuclear reaction to take place depends on the projectile's mass, m, and the target's mass, M. For symmetrical nuclear reactions ($m \approx M$), the minimum beam energy is estimated to give

$$\begin{aligned} E_{lab} &= \frac{m + M}{M} V_{total} \\ &\approx 2V_{nuclear} \\ &\approx 360\text{MeV}. \end{aligned} \tag{4.6}$$

4.2 The Fusion Evaporation Process

In order to produce the nuclei of interest in this work, fusion evaporation reactions are the only reasonable candidate that synthesises nuclei that are incredibly neutron deficient. However, there is major competition during the formation of the compound nucleus that causes it to split into fission fragments. A visual description of the formation process is shown in figure 4.3. When there is a successful fusion reaction between the projectile and the target nuclei, it is formed in an energetic state ($E_{excitation} \approx 30$MeV) at large spin ($J \approx 25\hbar$), with the complete process taking place within 10^{-21} seconds [36]. At this point, if the nucleus has not undergone fission, due to, for example, strong radial frictional forces that has prevented the Coulomb repulsion between the two nuclei, it starts to *evaporate* excess nucleons, because there is sufficient nucleon separation energy. These carry away relatively large amounts of the nucleus' excitation energy (roughly 5–10MeV per nucleon),

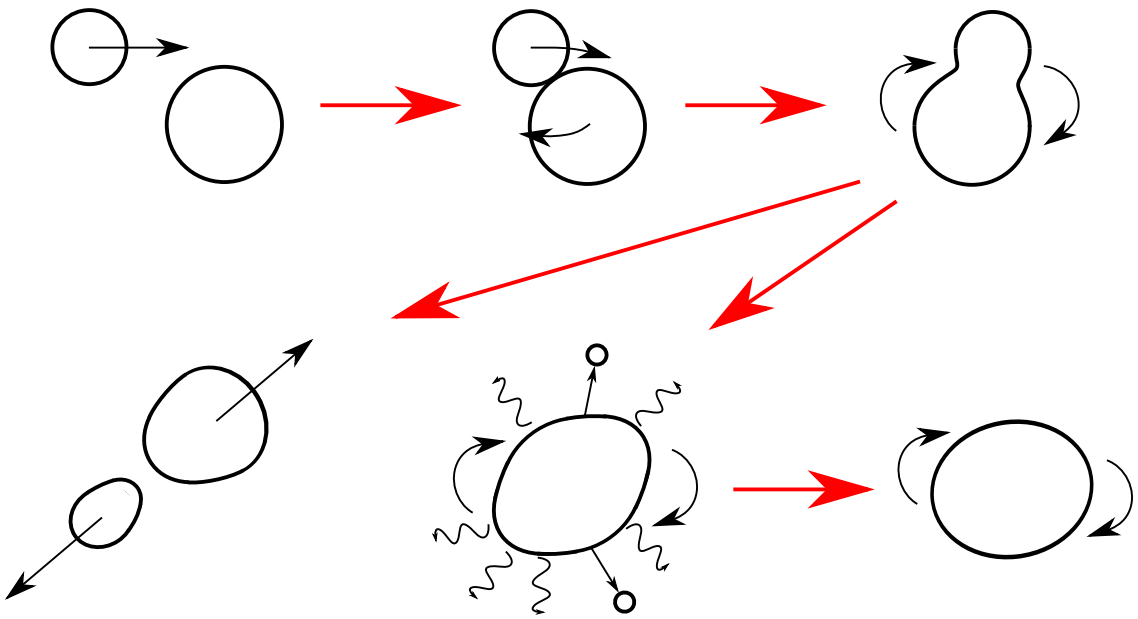

Figure 4.3: A schematic sequence of the fusion evaporation process. There are far fewer cases of *head-on* collisions compared to reactions where the projectile is slightly off-centre. This primarily drives a large angular momentum in the compound nucleus, with a more likely possibility of it simply splitting again.

while only reducing the nucleus' spin by a small amount (usually by 1–2$\hbar$). This process takes place roughly $10^{-18\pm2}$ seconds after the formation of the compound nucleus, and stops when the nucleon separation energy becomes less than zero in the nucleus. The population distributions for the nuclei of interest is shown in figure 4.4. The emission of statistical γ rays proceeds the evaporation of nucleons. These energetic (1–3MeV) dipole transitions come from a region where the density of states in the nucleus are very high; so much so that performing any useful γ ray spectroscopy would be unfeasible. Each statistical γ ray also reduces the nucleus' total spin by roughly 1$\hbar$, with the process taking roughly $10^{-15\pm2}$ seconds, until the structure of the nucleus has reached the *yrast* region.

The *yrast* structure of the nucleus, defined as having the lowest excitation energy available for a given angular momentum J, undergoes primarily stretched quadrupole γ ray transitions. They take away less energy than their statistical γ ray counterparts; stretched quadrupole transitions, on the other hand, take away 2$\hbar$ of spin from the nucleus, and at this point, it is the most effective way of de-exciting nuclei at low excitation energies. Quadrupole transitions are generally slower than dipole transitions (see Gamma Decay,

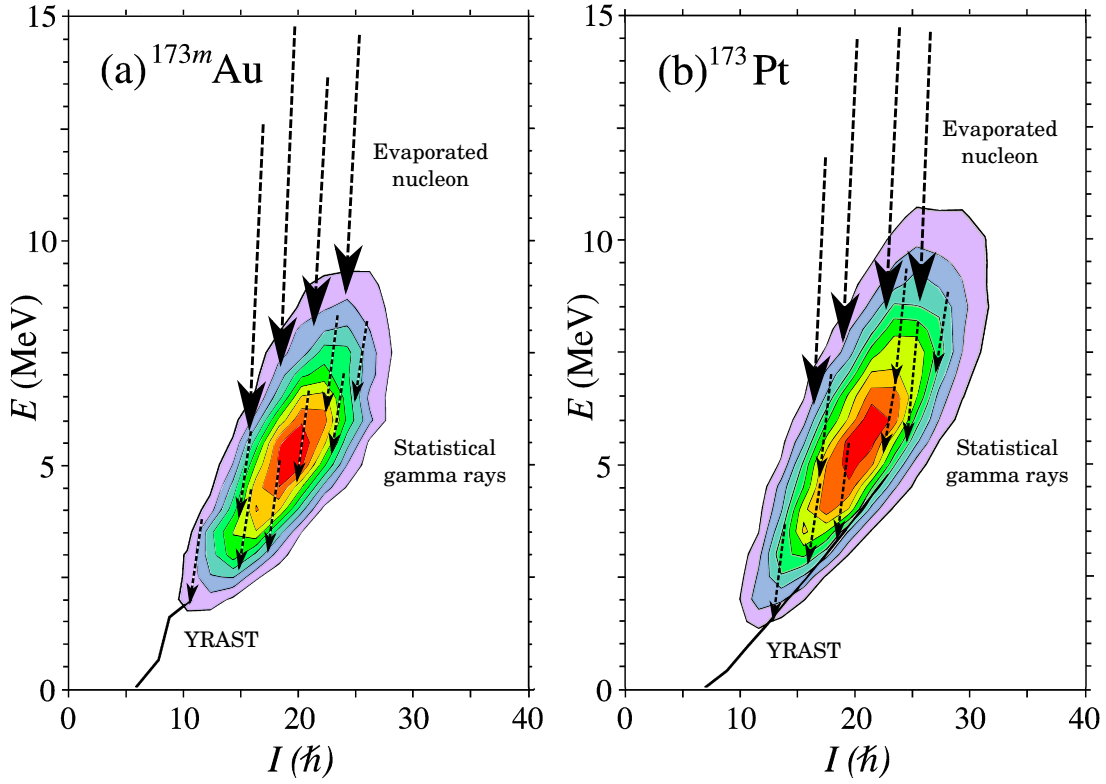

Figure 4.4: Measured fusion evaporated population distributions, along with the previously known yrast line (solid black), of the nuclei of interest [38]. The energy and angular momentum distributions were obtained by measuring the modular energy and multiplicity, respectively, of the germanium/BGO detector combination at GAMMASPHERE. This was then transformed into the displayed phase space above by using a 2-dimensional Monte-Carlo unfolding method [38], given the response functions that were obtained by using an ^{88}Y source.

chapter 3, section 3), and thus dominate over time regions of roughly $10^{-11\pm1}$ seconds since fusion took place. As the states have become more discreet at lower excitation energies, in-beam γ ray spectroscopy can be performed.

Certain states in nuclei may be meta-stable ($T_{1/2} > 10^{-9}$ seconds). These *isomeric transitions* (IT), if sufficiently short lived, can take place when the recoiling nucleus is still inside the target chamber. For longer-lived isomers, it will not be possible to utilise the detectors in the target chamber; instead, as the recoil would have likely reached the focal plane detector chamber before the isomer has completely decayed, the detectors there will be able to measure its decay. It should be noted that extremely long lived isomers do exist; the 9^+ state in ^{180}Ta^m, for example, is so long lived that no decays have been observed

from this state; a lower limit to its half-life of $> 10^{15}$ years has been set [39]. This is in contrast to the half-life of roughly 8 hours for its 1^+ ground state [40]. An isomeric state could also face severe competition due to more favourable decay modes, particularly for nuclei located far from stability.

It should be noted that the compound nucleus leaves the target material with its angular momentum vector roughly perpendicular to the direction of the beam. This becomes "smeared" after the evaporation of several nucleons; a high degree of orientation is retained, however, and lasts over the typical lengths of reaction target chambers. Consequently, this allows the opportunity of measuring the angular intensity distributions of emitted γ rays, as a function of the target-chamber detector's azimuthal angle θ. Without going into the details, different angular distributions arise from different multipolarity transitions taking place inside the nucleus, and allows them to become distinguishable. In this work, measurements were obtained using DCO (Directional Correlations de-exciting Oriented states) ratios for the more intense γ rays in ^{173}Pt (see chapter 7, Spectroscopy of the Neutron Deficient Nucleus ^{173}Pt), and in the case of lower statistics, angular intensity ratios in ^{173}Au (see chapter 6, Spectroscopy of Proton Unbound ^{173}Au and its α-decay Descendants).

4.3 JUROGAM II

In order to capture as much radiation as possible in the target chamber, detectors of high photo-peak efficiency and resolution, which are sensitive to energy regions between 50keV and 2MeV, are employed. An array of detectors is situated around the target, covering as much solid angle as practically possible. Using semi-conductor solid state crystals instead of scintillators benefits from vastly improved energy resolution of the detector, with the trade-off of having lower photo-peak efficiency. The interaction cross section of photoelectric absorption is roughly proportional to Z^4 for pure materials, or the average $\bar{Z}^4$ for a compound crystal; this value tends to be larger for scintillator crystals, due to their compounds containing heavy elements, than their semi-conductor counterparts. The resolution of a photo-peak depends on a number of factors, some being detector

Ring	θ	ϕ	Detector Type
1	157.6°	0°, 72°, 144°, 216°, 288°	EUROGAM Phase-I
2	133.57°	18°, 54°, 90°, 126°, 162°, 198°, 234°, 270°, 306°, 342°	EUROGAM Phase-I
3	109°, 100°	15°, 45°, 75°, 105°, 135°, 165°, 195°, 225°, 255°, 285°, 315°, 345°	Segmented Clover
4	80°, 71°	15°, 45°, 75°, 105°, 135°, 165°, 195°, 225°, 255°, 285°, 315°, 345°	Segmented Clover

Table 4.2: A list of azimuthal (θ), polar angles (ϕ) and detector type for each ring in the JUROGAM II detector array.

independent (such as electronic noise or statistical charge/photon collection) and others being detector intrinsic (such as the type of material and detector size).

The target chamber is surrounded by JUROGAM II, a Compton suppressed hyperpure germanium (HP-Ge) detector array made up of 15 EUROGAM Phase-I type detectors [41] and 24 segmented Clover detectors [42], and captures prompt γ radiation emitted from fusion-evaporated recoiling nuclei formed at the target position. The array is divided into four rings of detectors, details of which can be found in table 4.2. The detectors have a measured full width at half maximum (FWHM) of ∼3.3keV at 121keV, and ∼5.6keV at 1408keV; this permits detailed γ spectroscopy that would otherwise be impossible to perform on detectors with poorer energy resolutions.

Each detector housing consists of an entrance absorber that attenuates lower energy photons from entering the germanium crystal, usually at energies below ∼50keV. (see figure 4.5). Furthermore, each HP-Ge detector is surrounded by bismuth germanate (BGO) scintillators connected to photo-multiplier tubes (PMTs) that vetoes any photon that Compton scatters from a HP-Ge crystal into one of the BGO detectors. The entrance of these detectors have collimators that reduce the amount of scattered photons coming from the target chamber, as well as to suppress direct triggering from the BGO scintillators.

The germanium detectors are of coaxial nature, with the outer edges of the crystal rounded off so that it gives a uniform electric field within the depletion region. They typically require a bias voltage of about 5kV to fully deplete the crystal. Germanium

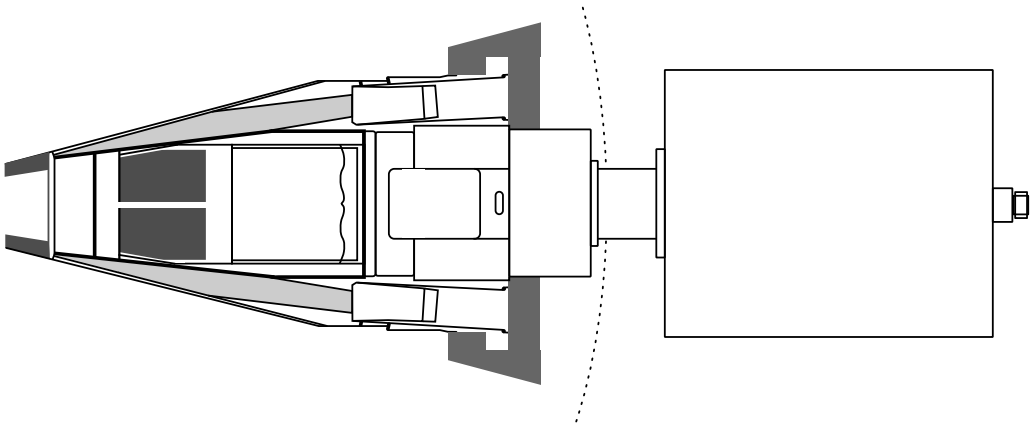

Figure 4.5: The composition of the Compton suppressed HP-Ge detector. The BGO scintillators surround the crystal and vetoes any photon signal detected in both the germanium and the BGO detector. The HP-Ge crystal is kept at constant temperature from contact with a metallic finger, connected to the LN_2 dewar. The pre-amplifier electronics are housed at the back of the setup. Image used from [41].

crystal detectors may possibly have the best photon energy resolution available, when compared to other semiconductors or scintillators, for the purpose of detecting γ and X-radiation. This is primarily due to germanium's small band gap of approximately $\sim$0.7eV. This causes a significant problem with thermal electrons jumping the band gap due to thermal excitations, dominating over any other effect, such as photo-electric absorption, which causes substantial electrical noise at room temperature. To reduce this noise to a tolerable level, the detectors must be cooled significantly; liquid nitrogen (LN_2) is sufficient in doing this. A system has been installed where LN_2 is pumped to the dewars that are in thermal contact, via a *cold finger*, with the inner coaxial walls of each germanium crystal to maximise heat flow, and are refilled three times per day. The germanium crystal is cooled down to temperatures of approximately 90K, greatly reducing the number of thermal band gap excitations.

Using BGO suppression shields greatly enhances the detector's peak to total ratio, allowing very weak photo-energy peaks to be discernible that would otherwise have been swamped by the background continuum. This is further enhanced for clover detectors by add-backing Compton scattered γ rays that have hit neighbouring crystals in the segmented clovers. When comparing the add-backed and raw γ spectra using the ^{152}Eu+^{133}Ba calibration sources, the efficiency of the clover detector was enhanced; indeed, at 1.33MeV,

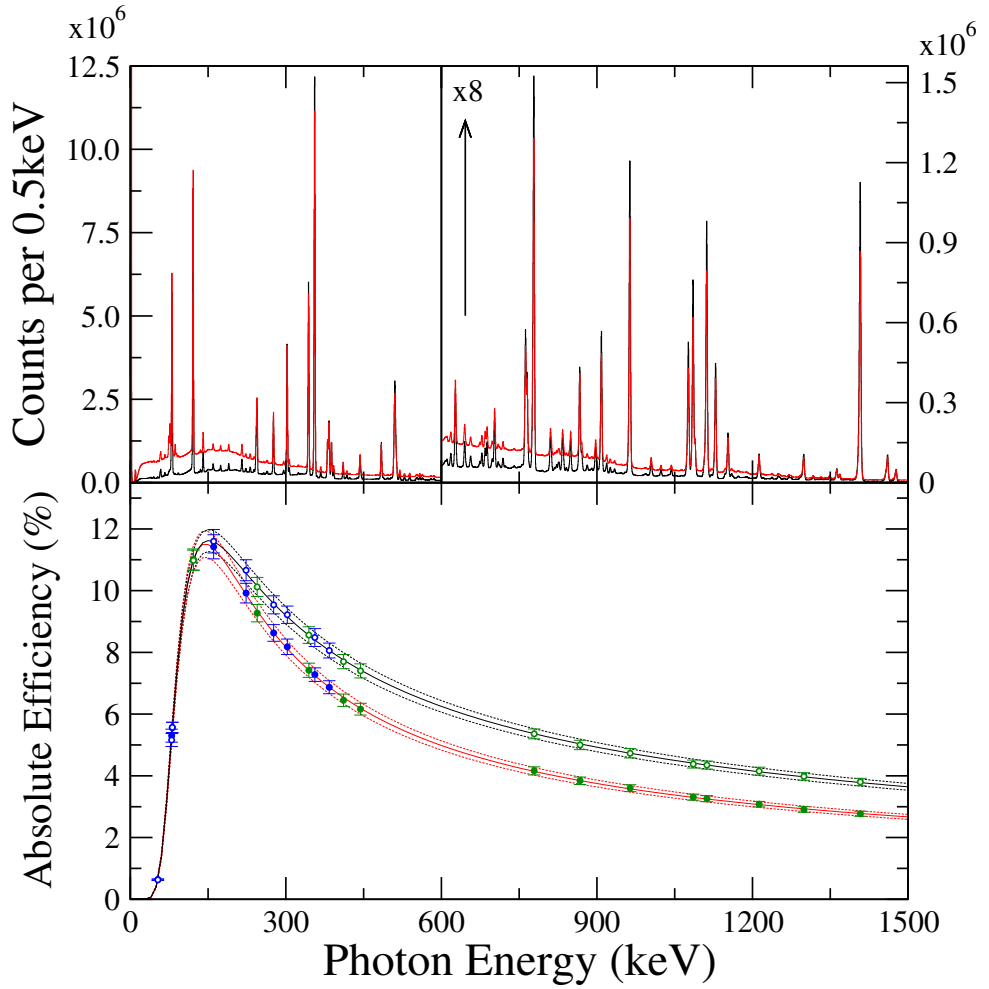

Figure 4.6: (Top) BGO suppressed JUROGAM II calibration spectrum using a ^{152}Eu +^{133}Ba mixed source, containing the add-backed uncorrected (red) and corrected (black) least squares efficiency function fit, which was obtained from using the ESCL8R software package [43]. The data were taken after the main experiment, and unfortunately contains large amounts of background photon peaks. (Bottom) Efficiency curves of JUROGAM II, when using the add-backed uncorrected (red) and corrected (black) data using the ^{152}Eu (green data points) and ^{133}Ba (blue data points) mixed source.

the measured absolute efficiency had increased from 2.8(1)% to 3.9(1)%. Literature reports place this value even larger, at 5.1%, [44] due to the fact that all rings were in use during that experiment.

4.4 Recoil Ion Transport Unit

Despite the state-of-the-art techniques employed with JUROGAM II, its detection of exotic γ radiation from the nucleus of interest will unfortunately become swamped with other γ ray events, primarily due to fission fragments, background, Coulomb excitation of the target, and other competing exit channels from the fusion evaporation process. With this in mind, it is essential to employ a system that can suppress the scattered beam, while transporting the evaporation residues, with high efficiency, to the focal plane detector chamber. Vacuum and gas filled mass separators are the current solution to the presented challenge - a series of magnets aimed at bending and focusing the recoiling particles, while filtering out the scattered beam. For gas-filled separators, the DQQ configuration is typically utilised, where the symbols D and Q represent dipole and quadrupole magnets, respectively. Vacuum mass separators generally only utilise dipole magnets. When a charged particle of charge eq, where e is the elementary charge, and velocity $\mathbf{v}$, enters a uniform magnetic field $\mathbf{B}$, it experiences a force acting perpendicular to the magnetic field lines, known as the Lorentz force, and is given by

$$\mathbf{F} = eq(\mathbf{v} \times \mathbf{B}). \tag{4.7}$$

If the particle is travelling perpendicular to the magnetic field, it will follow a circular motion. Equating the force's magnitude to the centripetal force, the equation can be simplified to give

$$F = \frac{mv^2}{\rho} = eqvB \tag{4.8}$$

$$\rho B = \frac{mv}{eq}, \tag{4.9}$$

where m is the particle's mass, ρ is the gyroradius of the particle travelling in the magnetic field's presence. One can also write this in terms of the mass number A, the proton number

Z and the number of electrons N_e contained in the recoiling nucleus to give

$$rB = \frac{uAv}{e(Z - N_e)}, \tag{4.10}$$

where u is the atomic mass unit. This consequently gives a discreet amount of bending for nuclei with different multiples of mass uA, and charge $e(Z-N_e)$, which one can exploit by utilising a position sensitive detector in the mass separator's focal plane. Some smearing will be present due to the recoil velocities having some statistical variance.

When the chamber inside the mass separator is instead filled with a gas, charge exchange occurs per particle-gas collision, which happens on the order of 100–1000 m^{-1}. When the recoils (and scattered beam for that matter) reach an equilibrium state, they have an average charge, $(Z-N_e) = \bar{q}$. Using the Thomas-Fermi atomic model, the electric charge $\bar{q}$ is only dependent on the velocity, v, and the proton number, Z; the equation can therefore be approximated as

$$\bar{q} = \left(\frac{v}{v_0}\right) Z^{1/3} \tag{4.11}$$

$$\rho B = \frac{uAv_0}{eZ^{1/3}} \approx \frac{0.0227A}{Z^{1/3}}. \tag{4.12}$$

This gives rise to having roughly the same bending trajectory, regardless of the initial charge state, or the velocity of the recoiling particle. However, their masses are still sensitive to varying bending forces; while it is now much more difficult to separate recoils that differ only by a few atomic mass units, filtering out much lighter scattered beam particles is still practical, even for symmetric reactions.

Using a gas filled separator does have its advantages over vacuum mass separators, however. For one thing, it has a large angular acceptance of roughly 10msr [45]; higher beam intensities can also be employed, due to the gas actively cooling the recoils as they travel through the multipole magnet chambers. The beam of recoil particles can be focused further by using vertically (Q_v) and horizontally (Q_h) focusing quadrupole magnets, implying a DQ_hQ_v configuration for most standard gas-filled recoil separators.

The recoil ion transport unit (RITU) was a new setup that employed a $Q_vDQ_hQ_v$

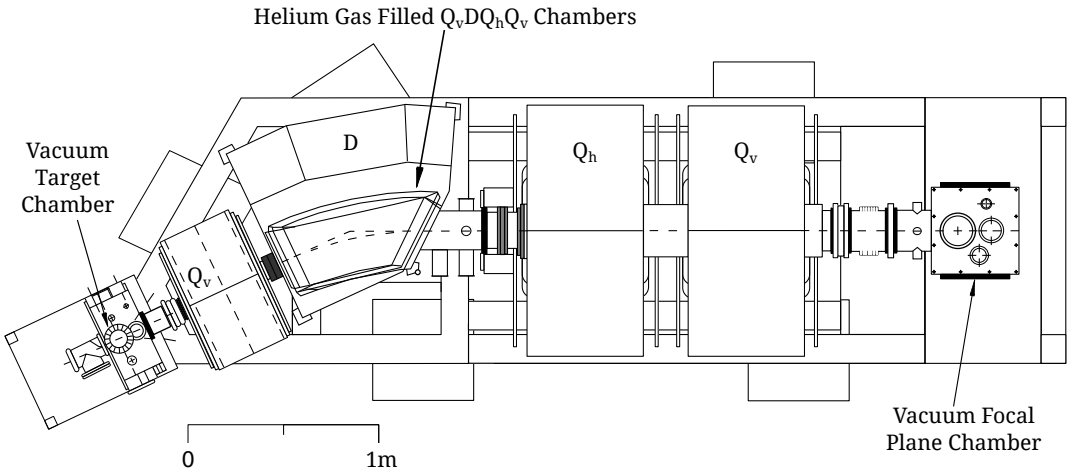

Figure 4.7: The setup for the gas filled recoil separator, RITU. It consists of a dipole magnet and 3 quadruple magnets, arranged in the configuration $Q_vDQ_hQ_v$ as the particle travels from the target chamber into the focal plane chamber. The dipole magnet was designed to separate the scattered beam particles from the evaporation residues, and the quadrupole magnets were used to focus the beam in either the horizontal axis (labelled Q_h) or the vertical axis (labelled Q_v). The JUROGAM II array is not shown at the target chamber, as well as the clover germanium detectors located in the focal plane chamber, where the GREAT (Gamma Recoil Electron Alpha Tagging) spectrometer was located.

configuration - an extra, vertically focusing quadrupole magnet located upstream from the dipole magnet, which was set to optimally match the recoils and scattered beam to the dipole magnet's emittance. This enhances the angular acceptance by roughly 30%. It also serves to suppress any fission fragments produced from the fusion reactions from travelling into RITU.

The inside of RITU is filled with helium gas at a pressure optimised to obtain the best optical resolution of the recoils, limited by the kinetic energy and the distribution of charge across all of the scattered recoils. Increasing the gas pressure reduces the spread of the charge distribution, but reduces the kinetic energies of the recoils. As a result the best pressure range is typically of the order 0.1–1mbar. This gas flow is also maintained in order to reduce its impurities. A differential pumping system is installed to separate the gas filled recoil separator from the vacuum inside the beam line; a constant pressure gradient is maintained in this section of RITU. Several atomic mass values can all be transported through the dipole chamber without adjusting the magnetic field strength, which helps preserve transportation of recoils for much weaker evaporation channels. Located just

downstream from the dipole magnet chamber is the beam stop control, which is motorised and can vary its position depending on the type of reaction used in an experiment. For symmetric reactions, it is necessary to move the beam stopper about 100mm into the chamber in order to capture the (heavier) scattered beam; in asymmetric reactions, where the beam particles are much lighter, experience a greater bending force, and so the beam stopper can be pulled further back to approximately 40mm.

The time of flight (ToF) for the recoiling nuclei can be measured by looking at the time difference between a hit in one of the JUROGAM II detectors and a hit in one of the focal plane detectors (usually the double sided silicon strip detector, described in the following section). The ToF depends on a number of factors, ranging from the target thickness, the incident beam energy, and any additional degraders that were installed. A small systematic error will arise due to the time it takes for γ rays to travel from the target chamber to one of the germanium detectors, and is of the order of a couple of nanoseconds. This is far smaller than the statistical spread of the ToF, due to the spread of the average charge, which causes slightly different paths when leaving the dipole magnet chamber, and the spread of the recoil's initial velocity. In this experiment, the ToF of the recoil leaving the target chamber and reaching the silicon strip detector has been measured to be 320(20)ns. Given the optical length of 4.8m for RITU, yields an estimation of the recoil velocity to be $0.050(3)c$. This is consistent with the more rigorous method of measuring the recoil velocity, explained in more detail in JUROGAM II Doppler-Shift Correction, chapter 5, section 3.

4.5 The GREAT Spectrometer

The Gamma Recoil Electron Alpha Tagging (GREAT) spectrometer [47], is located at the focal plane of RITU, and consists of various detectors that collectively aim to measure isomeric, ground state and fine structure decay spectroscopy for nuclei far from stability. After leaving RITU, the recoiling particles deposit some of their energy inside a multi-wire proportional counter (MWPC), before they implant into a pair of double sided silicon strip detectors (DSSD), where their decays can be measured directly. The DSSD is located at

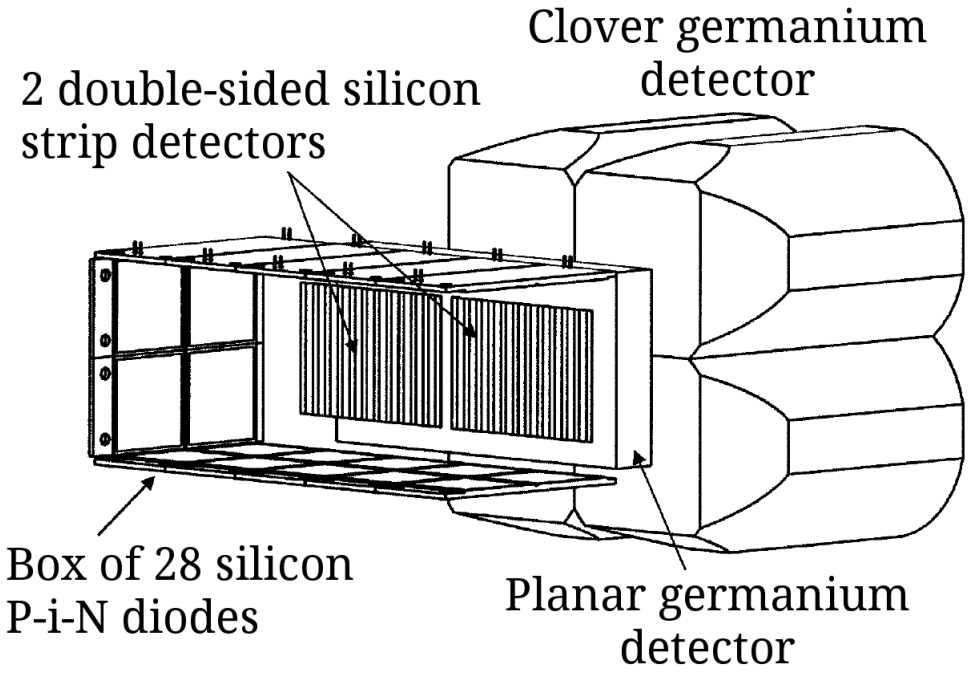

Figure 4.8: The arrangement of the GREAT spectrometer (the MWPC and the three other clover detectors are not shown in the figure). Recoiling particles approach the DSSD box from the MWPC, positioned beyond the left hand side of the diagram. Image used from [46].

the far end of a box containing silicon P-i-N diodes located on the adjacent walls, ceiling and floor. Any delayed or isomeric γ rays can be detected in either the planar germanium detector, located just behind the DSSD, or in one of the four segmented clover germanium detectors, located above, below and either side of GREAT. A sketch of this setup is outlined in figure 4.8. The half-lives of the exotic nuclei that can be studied using this setup are limited to the ToF of the recoiling particles, as well as the dead time when reading out the same channel inside the DSSD.

4.5.1 Multi-Wire Proportional Counter

Located upstream from the DSSD box, the Multi-Wire Proportional Counter (MWPC) leaves position, energy loss, and time signals of recoiling nuclei that exit out of RITU, allowing unambiguous selection of recoils to suppress background events, and it is known as *Recoil-Tagging* [48]. The standard procedure in most experiments using GREAT is to

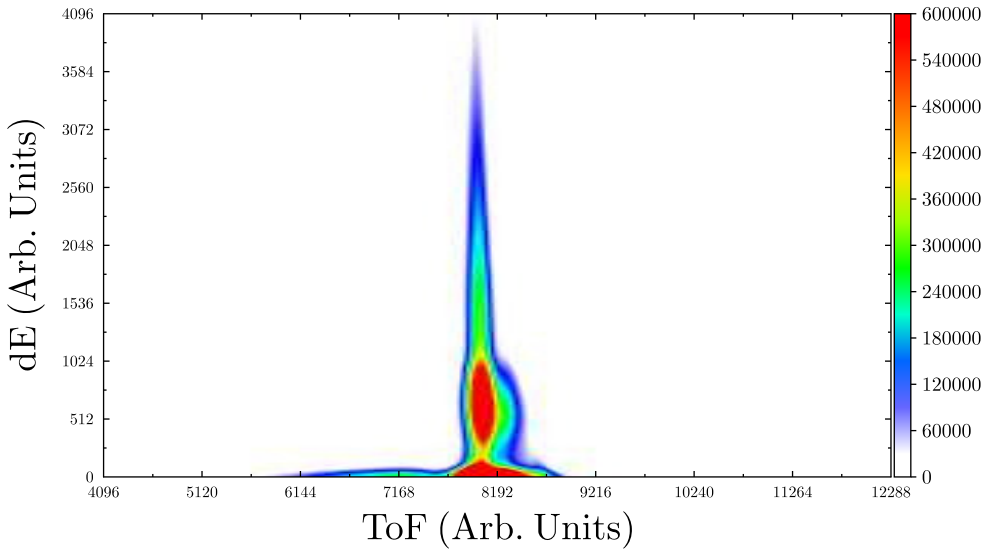

Figure 4.9: An Energy-Loss–Time-of-Flight matrix, with the time of flight increasing from right to left. The ToF seen here should not be confused with the ToF between the JUROGAM II array and the DSSD; the ToF, presented here, is an arbitrary measurement between a hit in the MWPC and a hit in the DSSD.

place a gating condition on an energy-loss–MWPC-ToF matrix, also known as *ToF-dE*, where recoils leave a distinct signal in the detector, an example from this experiment is shown in figure 4.9. It is also beneficial to tag on the recoil in the MWPC, as opposed to the DSSD, due to the higher transmission efficiency [49].

The MWPC is filled with isobutane gas to a pressure of ∼3.5mbar, which leaves an ionising track when recoils pass through it. The gas ions are then collected at wires located on all sides (except, of course, on the front and back) of the MWPC chamber, with a reported detection efficiency of nearly 100% [49]. The MWPC has an aperture size of 131mm in the horizontal direction and 50mm in the vertical direction, with the addition of a 1mm vertical strut that supports the mylar window. It is situated 0.24m upstream of the DSSD, and has a 0.9μm thick mylar entrance and exit windows, separating the isobutane gas from the helium gas in RITU and from the vacuum inside GREAT, respectively.

4.5.2 Double Sided Silicon Strip Detector

The DSSD functions both as the recoil implantation detector as well as an instrument that measures charged particle emission from the said recoils. The DSSD is sensitive to

α, β, and p emission of unstable nuclei with half-lives of the order of 10μs or greater. This lower limit is due to the time taken to process a signal pulse detected in one of its channels; during this time that channel is "dead" to other events that might take place there. The rest of the detector will still function even if one of its channels is "dead", due to the system utilising Total Data Readout (TDR), which is discussed in detail in the following section. The resolution of the detector, in the best case scenario, has a full width at half maximum (FWHM) of 20keV, although it is usually higher, due to crystal damage in the detector from the constant bombardment of heavy ions. Despite this, it allows the ability to unambiguously select the nucleus of interest by applying an energy gate on its characteristic α or p decay, within a certain time, after the additional correlation requirement of a recoil event, (which must leave a signal in the MWPC) implanting into the same pixel coordinate of the DSSD. This technique, known as *Recoil-Decay Tagging* [50], or RDT, serves as a powerful tool to filter out all but the single nucleus of interest (with the exception of multiplet energy peaks, with contributions coming from different nuclei).

The DSSD contains 2 sides of strips, with the back side having 60 vertical x-strips and the front side having 40 horizontal y-strips with a strip pitch of 1mm, giving dimensions of 60mm $\times$ 40mm. Two of these detectors, each being 300μm thick, are used, giving an effective total of 120 vertical x-strips and 40 horizontal y-strips. They are separated by a 4mm gap in the centre of the DSSD box. While silicon has a slightly larger band gap compared to germanium, with a value of $\sim$1.1eV, the detector still requires cooling in order to reduce electrical noise. Instead of using liquid nitrogen, however, alcohol cooling is sufficient. A system circulates alcohol through the DSSD cooling block, maintaining an equilibrium temperature of -20°C (253K).

By comparing the reported recoil transmission efficiencies to the MWPC and to the DSSD [49], the average recoil implantation coverage of the DSSD is 77(3)%. Inside the depletion region, the charge collection efficiency of the DSSD is roughly 100%. Neglecting the dead layer (non-depleted) on the detector's surface, the full-energy decay particle

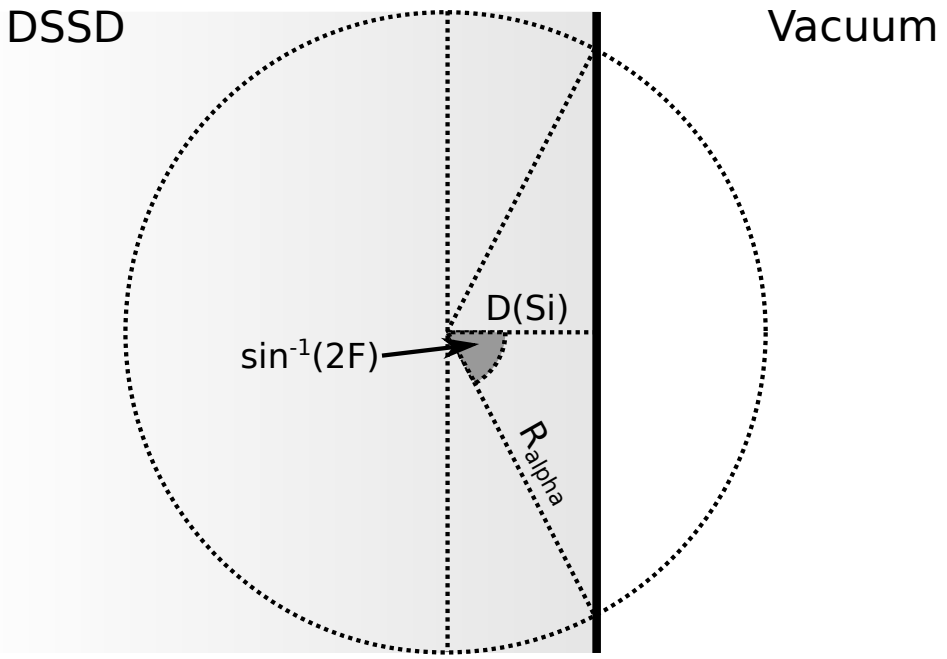

Figure 4.10: Illustration of the α particle range in silicon that is emitted from the recoil, with part of its spherical region falling outside of the DSSD.

efficiency of the DSSD can be calculated by the following function

$$\epsilon(\text{DSSD}) = 0.5\left[1 + \sin\left(\frac{\pi}{2}\frac{D(\text{Si})}{R(\alpha)}\right)\right], \tag{4.13}$$

where $R(\alpha)$ is the distance the α particle has travelled inside the material, and $D(\text{Si})$ is the recoil implantation depth. $D(\text{Si})$ is semi-empirical, and was partly by estimating the number of escaped particles from a given α-decaying isotope. Short lived, daughter α-correlated mother decays were used as there would be the least possible amount of random events and contamination. For this measurement, the α-emitters $^{168}\text{Ir}^m$ (E_α = 6323(8)keV [6]), $^{169}\text{Ir}^m$ ($E_\alpha = 6119(9)$keV [6]), ^{170}Pt ($E_\alpha = 6549(2)$keV [51]) and $^{173}\text{Au}^m$ ($E_\alpha = 6742(5)$keV [10]), correlated with their daughter α-decays within a short time gate, were selected. $R(\alpha)$ had been calculated using a model called Stopping and Range of Ions in Matter (SRIM) [52], and is used to fully determine $D(\text{Si})$. An empirical fit function was used to approximate the range of α particles, $R(\alpha)$, travelling in a pure silicon crystal, and is given by

$$R(\alpha) \approx AE_\alpha e^{BE_\alpha}\mu\text{m}, \tag{4.14}$$

where $A = 3.324(32)$ μm/MeV, $B = 0.0753(12)$ MeV^{-1}, E_α is the kinetic energy of the α particle and is valid for the energy range $(1 < E_\alpha < 10)$MeV. This was also required to estimate the recoil implantation depth, because once the escape fraction of the α particles, F, had been measured for each isotope, $D(\mathrm{Si})$ is calculated by using simple trigonometry

$$D(\mathrm{Si}) = R(\alpha)\cos\left(\sin^{-1}(2F)\right), \tag{4.15}$$

and is visualised in figure 4.10. The emission of α particles had been assumed to be isotropic and monoenergetic for a given radioisotope inside a perfect crystal constructed of pure silicon. Thus, the weighted average of the recoil implantation depth was found to be 18.5(12) μm, allowing ϵ(DSSD) to be calculated for any given α emitting isotope.

4.5.3 Planar Germanium Detector

Located 11.4mm behind the DSSD the planar germanium detector is a solid rectangular crystal of dimensions of 120mm $\times$ 60mm, and a thickness of 15mm. It has a very thin beryllium entrance window and is installed into the GREAT vacuum chamber in order to minimise any attenuation of low-energy photons. It is double sided, just like the DSSD, with 24 vertical x-strips located on the front side, and 12 horizontal y-strips located on the rear side of the detector, giving a strip pitch of 5mm. It is mounted on its own LN_2 cryostat that is refilled twice per day. Unlike other germanium detectors used in this experiment, the planar detector does not have a Compton suppression shield, partly because this would simply not fit into the current setup design, and is partly due to the fact that low energy photons mostly interact with the material via photo-electric absorption. Consequently this detector is extremely efficient in detecting low energy γ and X-rays, but it can also be used to detect β particles that punch through the DSSD.

While it is not possible to obtain an efficiency distribution of the detector experimentally (as it requires placing an extended source, distributed *inside* the DSSD, to mimic the recoil implantation distribution) Monte Carlo simulations have been performed in order to determine its absolute efficiency [46]. This plot is shown in figure 4.11, which also shows the effect of the planar detector's efficiency when one installs a silicon "punch-through"

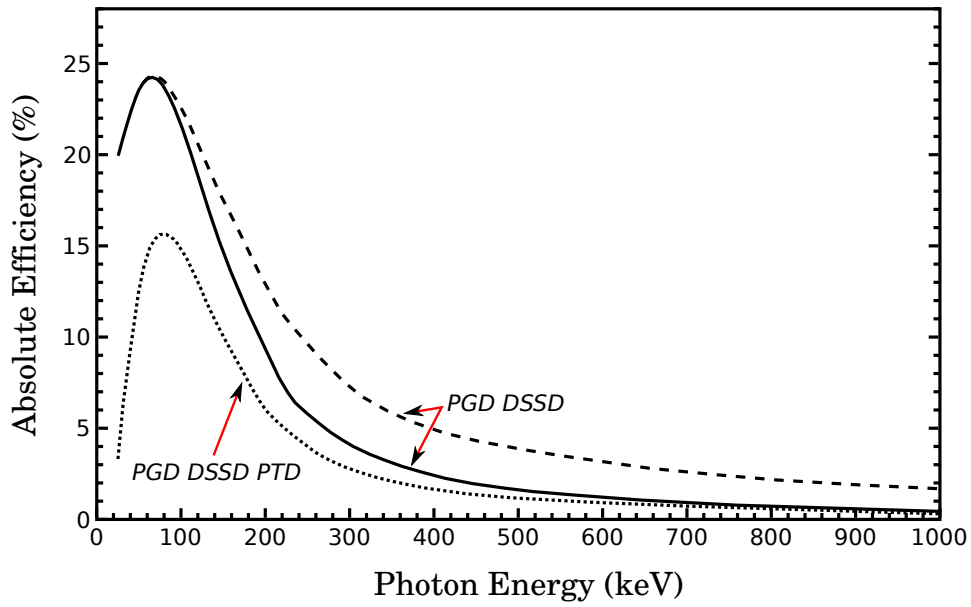

Figure 4.11: The simulated absolute efficiency of the planar germanium detector, including the effects of add-backing scattered photons, as well as adding an additional "punch-through" detector just behind the regular DSSD. Image modified from [46].

detector of thickness 475 μm just behind the regular DSSD, as well as the effect of add-backing scattered photons in the detector. No such "punch-through" detector was used in this experiment.

4.5.4 Focal Plane Clover Detectors

The GREAT spectrometer is surrounded by four clover germanium detectors, and just like the clover detectors in JUROGAM II, they are Compton suppressed coaxial detectors. Two are located above the DSSD box and two are located either side. They employ the same cooling techniques as JUROGAM II. They are more efficient in detecting higher energy photons than its planar germanium detector companion, and together are used to measure any delayed or isomeric γ-ray transitions that may take place in the focal plane. The two different detectors can also, albeit inefficiently, exploit multiple-photon coincidences between the two detector systems, allowing the possibility to observe a cascade of γ rays inside the focal plane.

4.5.5 P-i-N Diodes

The P-i-N diodes are an array of silicon detectors that surround the walls, floor and ceiling of the DSSD box, and aim to collect, or veto, escaped charged particles emanating from the DSSD, as well as measuring conversion electrons from highly-converted delayed or isomeric transitions that take place. It has a reported geometrical efficiency of about 30% [47]. Each of the 28 P-i-N diodes has an area of 28×28 mm^2 and a thickness of 500 μm. They are also connected to the same cooling block that cools the DSSD, with the circulation of alcohol keeping the detectors running at $-20°C$ (253K). This can be achieved by mounting two of the P-i-N-diodes onto a single motherboard, and having them form two rings around the inside surface of the cooling block, with the front-end components of the pre-amplifiers, housed on its own printed circuit board, connected to the motherboard's back, so the whole unit is cooled. This consequently allows the energy resolution of the P-i-N diodes to reach 5keV FWHM.

4.6 Total Data Readout

Modern experiments that are designed to look for detector correlations, particularly for highly exotic nuclei, require systems that have as little dead time as possible. This allows experiments to run with higher counting rates. Historically, setups were configured using hardware coincident gates with a certain time length, usually on the order of 10μs, in order to record the recoil implantation in the focal plane detector, measure any isomeric decays that may take place after, and include prompt γ rays emitted at the target position. This caused the whole system to become "dead" during the triggering event, which had huge diminishing returns for high count-rate experiments. This consequently had set observable limits in what could be achieved when measuring in-beam and decay properties of exotic nuclei.

The total data readout method (TDR) [53], which was introduced with the commissioning of the GREAT spectrometer, is a novel new technique employed to eliminate hardware triggers of past, utilising all of the electronics for each detector to be read out independently. This essentially eliminates dead times of the detectors, with the exception

of two events hitting the same detector channel within a very short time. All processed signals are synchronised to a global clock running at a frequency of 100MHz, where events are time-stamped to a precision of 10 nanoseconds. These events are then collected using software in the *event builder*, and temporal and spatial correlations can be realised by using either simple or complex filtering rules. For example, random γ-ray events can be suppressed by starting with a recoil implantation, and looking back in time by using a recoil time of flight gate. Software filtering requires more powerful computer resources, which have become more affordable with the advancements of CPU and memory technology. Advances in storage technology has given the possibility for writing large amounts of data, when using TDR, without much difficulty.

The new ADC timestamping and hit pattern cards, offering 32 readout channels of 14 bits each, are connected to the front-end electronics and synchronised with a global metronome. The ADC conversion and readout time are less than the pulse shaping time in the amplifiers; pileup events are the only way counts can be rejected. A pileup event is triggered during a second timestamp that is recorded during the gate width of the first timestamp in a detector. The time stamped and pattern units also read out an address to identify which detector the signals came from, as well as the type of signal recorded from that detector. This time-ordered data is sent through point-to-point data links into VME cards, where the information is buffered before transmitting to the event builder via a 1 gigabit ethernet connection.

4.7 Data Analysis

The in-house Java software package GRAIN [54] was developed to read online or offline data streams produced using the TDR acquisition system. As it is compiled and executed using java libraries, GRAIN can be opened on any operating system that supports these libraries (Windows, Solaris, Unix and Linux systems). Before any sorting is done, the software processes the time-ordered data stream from the event builder, or from an offline storage device, and assigns events to the detector channels they had originated from. This filters events that have piled-up and coincident events between a germanium crystal and

a BGO scintillator, within a time gate. The event data is then parsed, setting trigger and/or multiplicity variables depending on the configuration input file that the user can edit. A gainmatching input file is then used to apply gain coefficients to any of the detector channels specified by the user, up to second order (higher order gain-matching must be done inside the sort code). GRAIN then finally sorts the filtered data, according to the user inputted java sort code, into 1D and 2D histograms and n-tuples, which the user can manipulate via the software's GUI.

While there are no hardware triggers in use in modern experiments, GRAIN creates a virtual triggering mechanism, which behaves similar to the hardware triggering systems used in the past. The obvious difference here is the complete flexibility of the triggering conditions, which can be optimised to look for features of interest in the experiment; GRAIN can also trigger on any detector located in GREAT. In this experiment, the trigger was set to the silicon-gas time to amplitude converter TAC, and was fired when a signal sends a *"STOP"* signal to the TAC (i.e. when the recoiling particle hits the DSSD). The common parameters that were used and modified by the user were the *trigger width* and the *trigger delay*, with dimensions given as the number of clock cycles, or *ticks*. The *trigger delay* offsets the start of the triggering. It can be set either before the DSSD implantation event (< 0 ticks) or afterwards (> 0 ticks). By allowing a trigger delay before the event, one can include the MWPC and JUROGAM II detectors, as the recoil had interacted with them prior to implantation. The *trigger width* sets the size of the trigger, from the starting value set by the *trigger delay*, up to a maximum time of *trigger width*+*trigger delay* ticks. Setting the *trigger width* to large values allows isomeric and delayed transitions to be observed, at the cost of observing more random events.

A different kind of correlation mechanism was required to measure decay spectroscopy in the focal plane, as most decay half-lives greatly exceed most time window settings used for the trigger. The GRAIN DSSD tagger aims to collect all *event* information that takes place within a defined *tagger time length*; within a single pixel, or for a square of nine pixels, with the last *event* taking place in its central pixel. An *event* can be discriminated into two candidates:

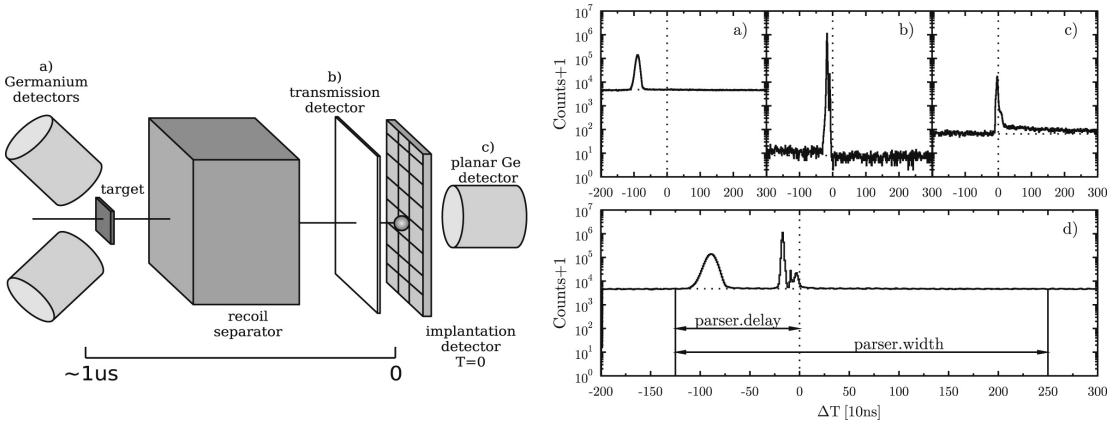

Figure 4.12: A description of the TDR setup, with the time stamps of (a) an in-beam germanium detector, (b) a transmission detector, and (c) a focal plane germanium detector, relative to the trigger event in the implantation detector. Section (d) shows the total of the three individual spectra, with the different data parser parameters shown. Image obtained from [54].

- A recoil event, which is coincident with an energy-loss signal left in the MWPC.
- A decay event, which is anti-coincident with a signal left in the MWPC.

These candidates are placed into an array, containing the x and y coordinate of the DSSD, as well as their time stamps; candidates are time stamp ordered from the earliest event to the latest event. A single pixel tagger has been utilised for this experiment, as it reduces the amount of random events interfering with signals of interest. One stresses, however, that it does not completely eliminate it, which causes systematic problems when measuring decay branching ratios or half-lives of long-lived nuclei. This is covered more in the next chapter.

Chapter 5

Experimental Techniques

Online experimental runs require additional corrections to some of the detectors that were impossible to determine just by using a stationary calibration source. These corrections were applied post-experiment at the software level, in order to provide corrected spectra, as well as minimising any systematic uncertainties.

5.1 DSSD Baseline Correction

Charged particle decays that occur a very short time after a recoil implantation may give an energy that is higher or lower than its true value. Recoils leave a very large voltage signal that does not completely decay away once the channel's pre-amplifier becomes live again. A subsequent decay will in fact "pile-up" on top of the decaying signal, giving a larger perceived energy. In addition to this, as shown in figure 5.1, the energy then overshoots the baseline, resulting in a lower energy value, before returning to the baseline. This may be due to the pole-zero setting for the front-end electronics.

One way to mitigate this effect is to apply a post-experiment correction to the data, which takes into account of how the pulse signal behaves in the electronics. In other words, an empirical fit function

$$\Delta E_{baseline} = Ae^{-Bdt^3} - Ce^{-Ddt^3} \tag{5.1}$$

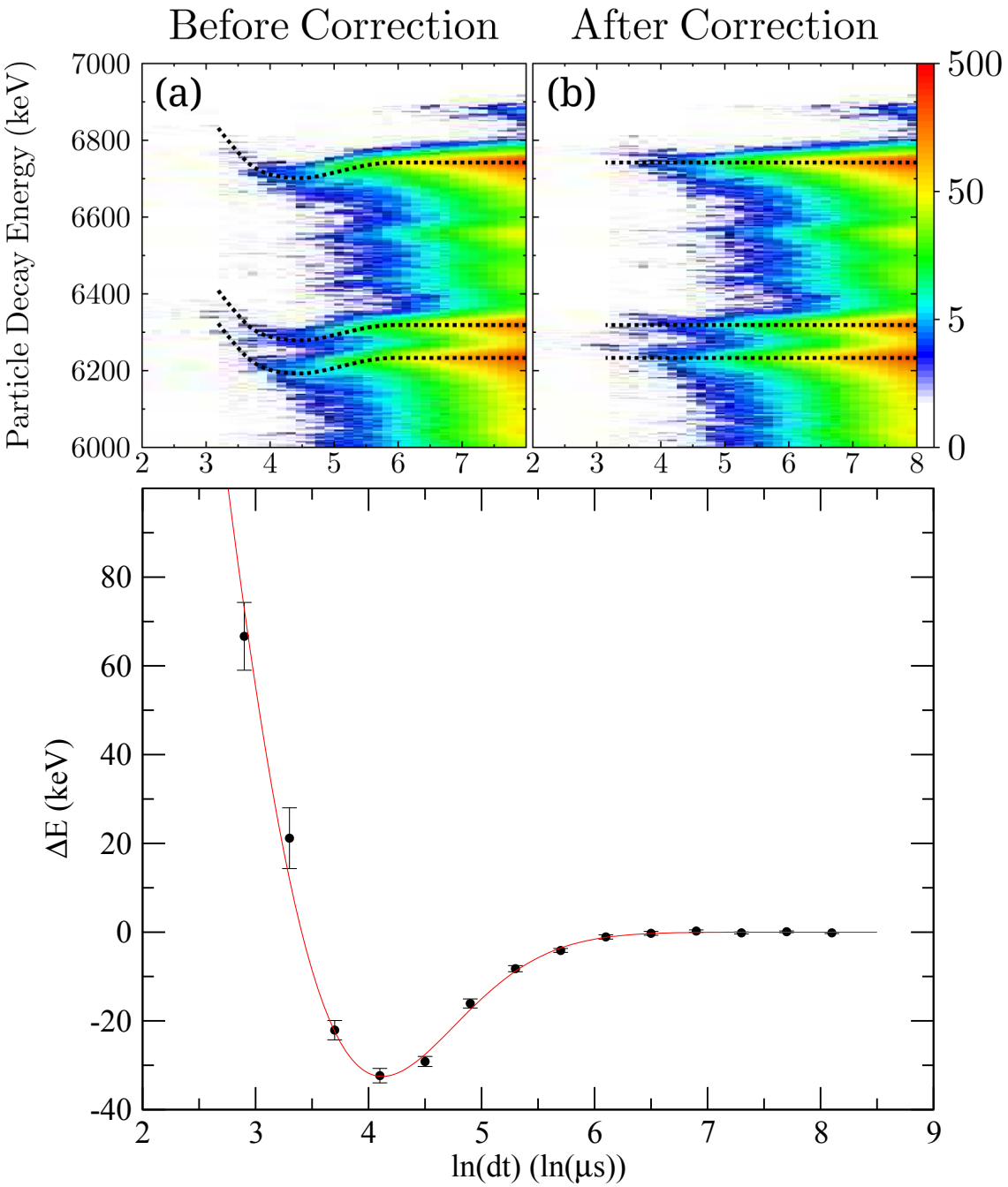

Figure 5.1: Illustration of the baseline correction, showing the before (a) and after (b) ln(dt)-E_α matrix plots. A dotted line presented on both panels is used to guide the eye. (c) Measured α energy differences as a function of the natural logarithm of the time since the recoil implantation. The data points are the average of three α-emitting nuclei. The time gate width used to create each α spectrum was 0.4 on the natural log scale.

was used to perform a least-squares fit to the averaged difference in the observed energy centroid values to the correct values, $\Delta E_{baseline}$, of several α emitters: $^{173}\mathrm{Au}^{m}$, and $^{172,173}\mathrm{Pt}$. Short time intervals were used over a large range of the $\ln(dt)$-E_α matrix plot. A noticeable reduction in the energy variance was observed after applying the correction.

5.2 DSSD Internal Calibration

There is a thin dead layer in the silicon detector that is not fully depleted when a bias voltage is applied. This consequently has the effect of no charge collection due to the electric field not penetrating this region. Should an α particle travel through it that ionises some of its silicon atoms inside the dead layer, that charge is lost. Also, the energy of the recoiling daughter nucleus cannot be measured in the 3–α source. This results in an energy offset between the measured α energy values by $E_{3-\alpha} - E_{exp} \approx -80\mathrm{keV}$, and will only be apparent when measuring α decay energies of implanted recoils, which have sufficient energies to penetrate through this dead layer, and into the depleted region of the DSSD, where any charged particle decay that subsequently happens can potentially deposit all of its energy.

This energy offset can be corrected by measuring at least three α energy peaks that were not of interest in the experiment, with one at low energy, one at medium energy, and one at high energy. If p emission was observed, one can use that energy peak instead to replace the low energy α decay, which gives a confident calibration across a larger energy range. The new gain-matching coefficients were then used instead of the ones obtained from the 3–α source.

5.3 JUROGAM II Doppler-Shift Correction

Measuring prompt γ rays from fusion evaporation residues in the target chamber will have to contend with the fact that the recoil is moving at a significant velocity to cause its photon emission to be *Doppler shifted*. The shifted energy of the photon, E'_γ, emitted from a recoil travelling at velocity $\mathbf{v}$, viewed at an angle ζ with respect to the velocity

vector, is given by

$$E'_\gamma = E_\gamma \frac{\sqrt{1-\beta^2}}{1-\beta\cos(\zeta)}, \tag{5.2}$$

where $\beta = v/c$. In the non-relativistic limit ($v \ll c$), the first order approximation reduces the above formula to give the familiar relation

$$E'_\gamma \approx E_\gamma \left(1 + \beta\cos(\zeta)\right). \tag{5.3}$$

For a large number of recoiling nuclei, the average velocity vector, $\bar{\mathbf{v}}$, generally follows the beam axis. One can then approximate the angle ζ to be the azimuthal angle of the target chamber, θ.

Due to the statistical variation of the velocity vector around the beam axis, the "approximated" angle, θ, becomes 'smeared' by $\Delta\theta = \theta - \zeta$, degrading the energy resolution. Detectors have a finite size and thus have an opening angle, $\Delta\theta$, relative to the beam axis. This causes photons emitted in a cone of angles that are incident on the detector to have varying degrees of the shifted energy, which in turn further hampers the energy resolution in the detector. Other factors include the reaction kinematics in the target as well as the spread of velocities of the recoiling nuclei [55][56]. This phenomenon is known as *Doppler broadening*, in which the energy spread, ΔE_γ, which can be derived from the above equation to get

$$\Delta E_\gamma \approx E_\gamma \beta \sin(\theta)\Delta\theta \tag{5.4}$$

is only one of the many components that degrade the photon's energy resolution in the detector. The segmented clover detector in JUROGAM II was installed in rings around 90°, because each crystal has smaller opening angle, compared to the Phase-I detectors, located at more extreme angles. With a smaller $\Delta\theta$, the Doppler broadening is reduced. Doppler broadening is not present when using a stationary calibration source.

The Doppler shift can be corrected by measuring the velocity of the recoil, β, by measuring the gradient of several γ rays as a function of the cosine of the detector azimuthal angle. The 458, 612 and 769keV transitions in ^{172}Pt [9], and the 286, 463 and 575keV transitions in ^{170}Os [57] were used to measure β, and was performed during the four

different stages of the experiment, see table 4.1.

5.4 Random Events

Experiments that use fusion evaporation reactions produce all manners of different isotopes, depending on how many particles were evaporated from the compound nucleus. Generally, the most exotic nuclei have very weak reaction channels, and so in order to maximise the detection efficiency, the TDR system was employed, allowing higher count-rate experiments to be performed without suffering from losses. The most difficult nuclei that can be produced generally have very short half lives; such properties, as well as their decay branching ratios, can be measured with confidence. However, the benefits that TDR gained has a double edged sword; higher count-rate experiments due to higher beam intensities also greatly increase the amount of *random miscorrelations* that occur, especially for much longer lived nuclei. This is particularly a problem for the DSSD, as the probability of receiving an intruder event, landing onto the same pixel where the nucleus of interest was implanted prior, is proportional to the recoil rate on the DSSD. In this experiment, the average recoil implantation rate on the DSSD was measured to be roughly 150Hz; the average recoil intrusion rate per pixel of the DSSD was thus determined to be $\lambda_{r-r} \approx 0.03$ s^{-1}. Other factors also contribute towards the total random event rate, such as α particles travelling from a neighbouring pixel. When an intruder particle leaves a signal before the decay of the interested recoil had happened, the correlation was discarded from the tagger; not only does this affect the statistics of long-lived nuclei, it affects their apparent half-lives and decay branching ratios, *biasing* them with apparent smaller values.

In order to apply a correction to the half-life and branching ratio, the distributions of these intruder events were investigated. Four possible scenarios were considered: Two recoil events and an α-recoil event taking place within the same pixel; two α events and a recoil-α event occuring in neighbouring pixels, ensuring the second event is located in a different pixel than the first. A different tagger history was created that looked for a series of events that took place both in the central and surrounding pixels. The time difference between the two events for each of the four combinations were collected, before summing

them together to give a single distribution. A least-squares fit was performed to the data, with the fit function, $f(t)$, defined as

$$f(t) = Ae^{-Bt} + Ce^{-Dt} + Ee^{-Ft} + Ge^{-Ht} + Ie^{-Jt} \tag{5.5}$$

containing ten different parameters used for the fit. Once these values were obtained, the function was then normalised across the entire distribution, giving the solution

$$N = \int_0^\infty f(t)dt = \frac{A}{B} + \frac{C}{D} + \frac{E}{F} + \frac{G}{H} + \frac{I}{J} \tag{5.6}$$

$$R(t) = \int \frac{f(t)dt}{N} = \frac{\frac{A}{B}e^{-Bt} + \frac{C}{D}e^{-Dt} + \frac{E}{F}e^{-Ft} + \frac{G}{H}e^{-Ht} + \frac{I}{J}e^{-Jt}}{\frac{A}{B} + \frac{C}{D} + \frac{E}{F} + \frac{G}{H} + \frac{I}{J}} \tag{5.7}$$

The formula for the half-life, $T_{1/2}$, was modified with the above correction formula, $R(t)$. The new formula

$$N(t) = Ae^{-\frac{ln(2)}{T_{1/2}}t} \cdot R(t) \tag{5.8}$$

had been used to measure the time difference, t, between the recoil event and the α-decaying event. A least-squares fitting procedure was used to measure the uncorrected ($T_{1/2,raw}$) and corrected ($T_{1/2,corrected}$) half-lives for four different nuclei: ^{170}Pt, ^{166,168}Os and ^{162}W and were compared to the half-life literature values. The measured decay branching ratios $b_{\alpha,raw}$ can be corrected by the following formula:

$$b_{\alpha,corrected} = b_{\alpha,raw} \cdot \frac{T_{1/2,corrected}}{T_{1/2,raw}} \tag{5.9}$$

Table 5.1 shows the measured values for $T_{1/2,raw}$ and $T_{1/2,corrected}$ for the above four nuclei, and the $b_{\alpha,corrected}$ and $b_{\alpha,raw}$ for three of the four nuclei (^{166}Os, ^{162}W, and ^{168}Os). They were chosen to give a range of different half-lives in order to test this methodology. Compared to literature reports for the same nuclei, it can be concluded that the proposed method is in good agreement with previously measured values.

	This Work		Literature	
Nucleus	$T_{1/2,raw}$ (ms)	$T_{1/2,corrected}$ (ms)	$T_{1/2}$ (ms)	σ
^{170}Pt	13.97(24)	14.02(24)	14.0(2) [51]	0.06
^{166}Os	199(7)	207(9)	220(7) [6]	1.1
^{162}W	1193(43)	1477(69)	1390(40) [58]	1.1
^{168}Os	1608(11)	2150(54)	2100(100) [6]	0.4
	This Work		Literature	
Nucleus	$b_{\alpha,raw}$ (%)	$b_{\alpha,corrected}$ (%)	b_α (%)	σ
^{166}Os	72(4)	75(6)	72(13) [59]	0.21
^{162}W	40(6)	49(8)	45.2(16) [6, 59, 60]	0.47
^{168}Os	33.7(16)	45.1(24)	44(4) [6, 61]	0.24

Table 5.1: Measured, corrected and literature values of $T_{1/2}$ and b_α for the above presented nuclei, and the number of standard deviations between the corrected measured values in this work to its corresponding literature value. The weighted mean was calculated for literature values where there was more than one reference.

5.5 Electronic Drifting

Over long periods of time, it was found that the gain amplifiers for some of the detector channels were slowly varying. The resulting shifts in the energy peaks were small, and only noticed when comparing the calibration data on either end of the experiment. The problem with electronic drifting can sometimes cause the gain amplifier to fluctuate, making correcting for such chaotic behaviour immensely difficult. In other situations, the drifting remains constant, resulting in a straight diagonal line that can be easily accounted for. This was the case for all of the detector channels that showed signs of electronic drifting. The effect was also linearly proportional to the detector's energy, and so in order to correct for the long term offset, the following equation, $\Delta E_{drifting}$, was added to the drifted energies:

$$\Delta E_{drifting} = (AE_0 + B)\frac{t_n}{T} \tag{5.10}$$

where t_n was the n^{th} run file, T was the total number of run files, E_0 was the uncorrected energy and A and B were coefficients that varied from channel to channel. An example of drifting observed in both the x and y strips of the planar germanium detector is shown in figure 5.2.

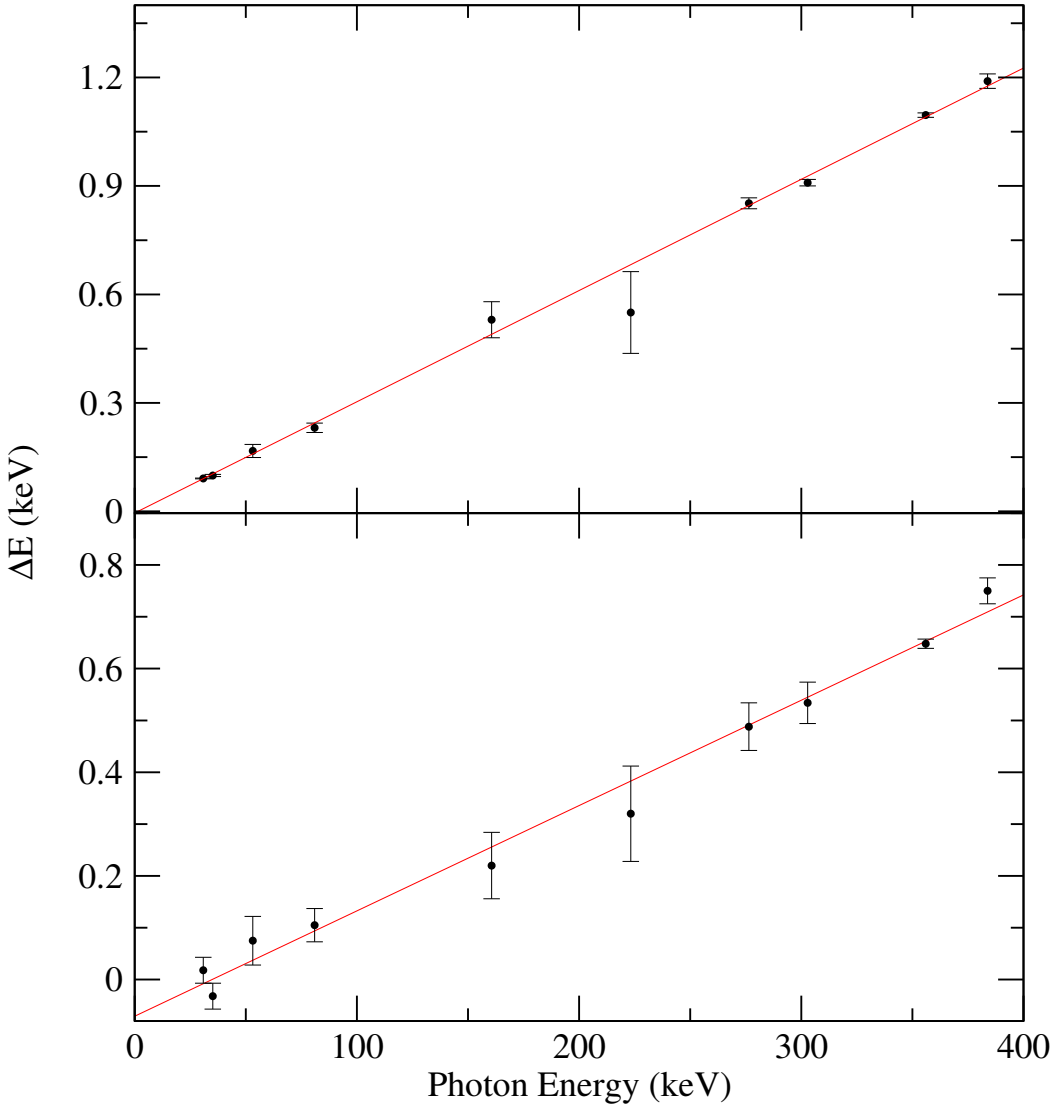

Figure 5.2: The measured amount of electronic drifting in the x-side (top) and the y-side (bottom) of the planar germanium detector. The energy difference between the two calibration sets on either end of the experiment was displayed, along with the least-squares fit function.

Chapter 6

Spectroscopy of Proton Unbound ^{173}Au and its α-decay Descendants

The amount of recoil correlated ^{173}Au α events collected from this experiment yielded approximately an order of magnitude more than was previously obtained by Kondev, *et al.* [4]. This had been made possible due to the long running time of the experiment; the conditions used to synthesise the ^{173}Au recoils were the same as what Kondev reported, although the running time of Kondev's experiment was not disclosed.

The recoiling ^{173}Au nuclei were produced via the $1p2n$ evaporation channel from the compound formation of ^{176}Hg*. Approximately 2×10^5 correlated ^{173}Au recoil-α events were recorded. The transmission efficiency in RITU to the DSSD had been reported to be 49.0(10)%, which utilised a similar reaction to this experiment [49]. The α full-energy peak ratio of ^{173}Au was measured to be 59.0(7)%, consistent to the calculated value of 57(4)%. The α-decay branching ratio for the high-spin decay and for the low-spin decay of ^{173}Au was reported to be 92(13)% and 94(19)%, respectively [5]. The production cross section, when folding in the above α branching ratios and efficiencies, was estimated to be 6.1(10)μb at E_{beam} = 392MeV and 3.3(5)μb at E_{beam} = 400MeV from this reaction. Some of the results shown in this chapter are also presented in reference [62].

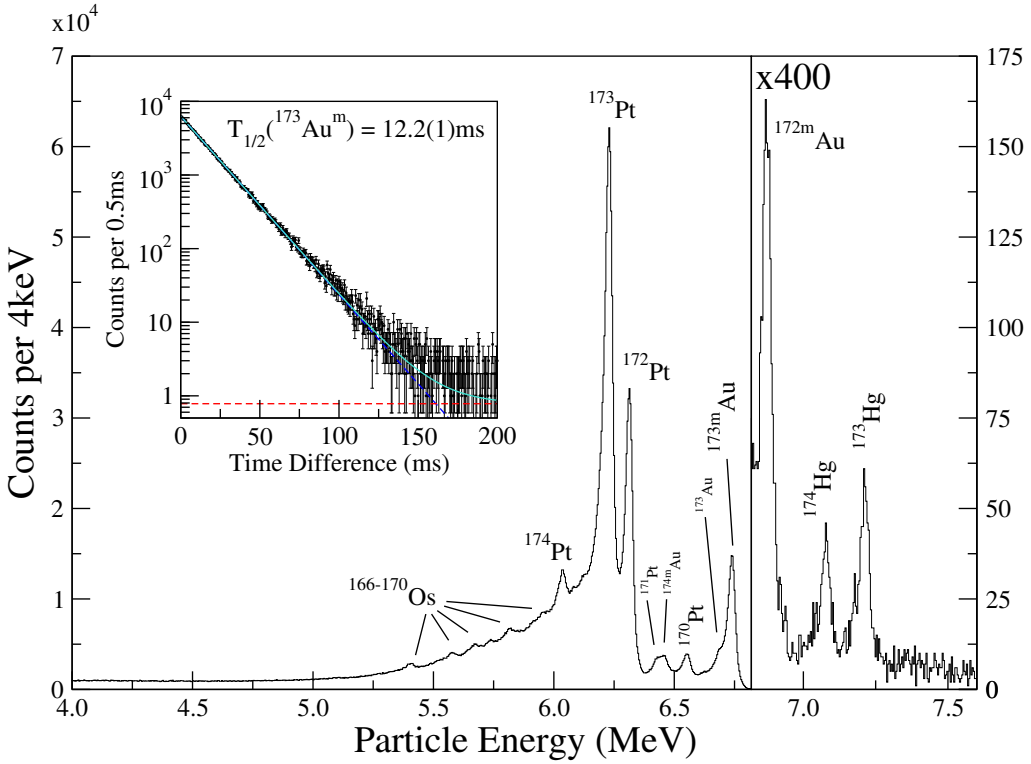

Figure 6.1: Correlated recoil-α spectrum showing decays that required a prior recoil implantation that took place within 100ms, which occurred within the same pixel of the DSSD. The inset shows the time difference between the recoil implantation and the subsequent charged particle decay when tagging on the α decay energy of ^{173}Au^{m} in the same pixel. A solid cyan line shows a least-squares fit to the data, along with the contributions due to the background (dashed red) and the nucleus of interest (dashed blue).

6.1 In-beam Spectroscopy using RDT Techniques

Figure 6.1 shows a spectrum of the vertical strips of the DSSD y-strips that shows all decays that take place within 100ms of a recoil implantation in the same pixel. This short time condition has suppressed much longer lived nuclei, without greatly affecting the nucleus of interest (see figure 7.1 for comparison); indeed this also had reduced the amount of random *mis-correlations* that contribute to the spectrum's background and false energy peaks.

The energy of the α decay of ^{173}Au^{m} was measured to be 6739(4)keV, which is consistent with previous measurements [47]. The corrected half-life of this state was also measured using a least-squares fitting tool, and was found to give 12.2(1)ms, which is much more precise than the previously reported value of 14(1)ms [4]. By tagging on the

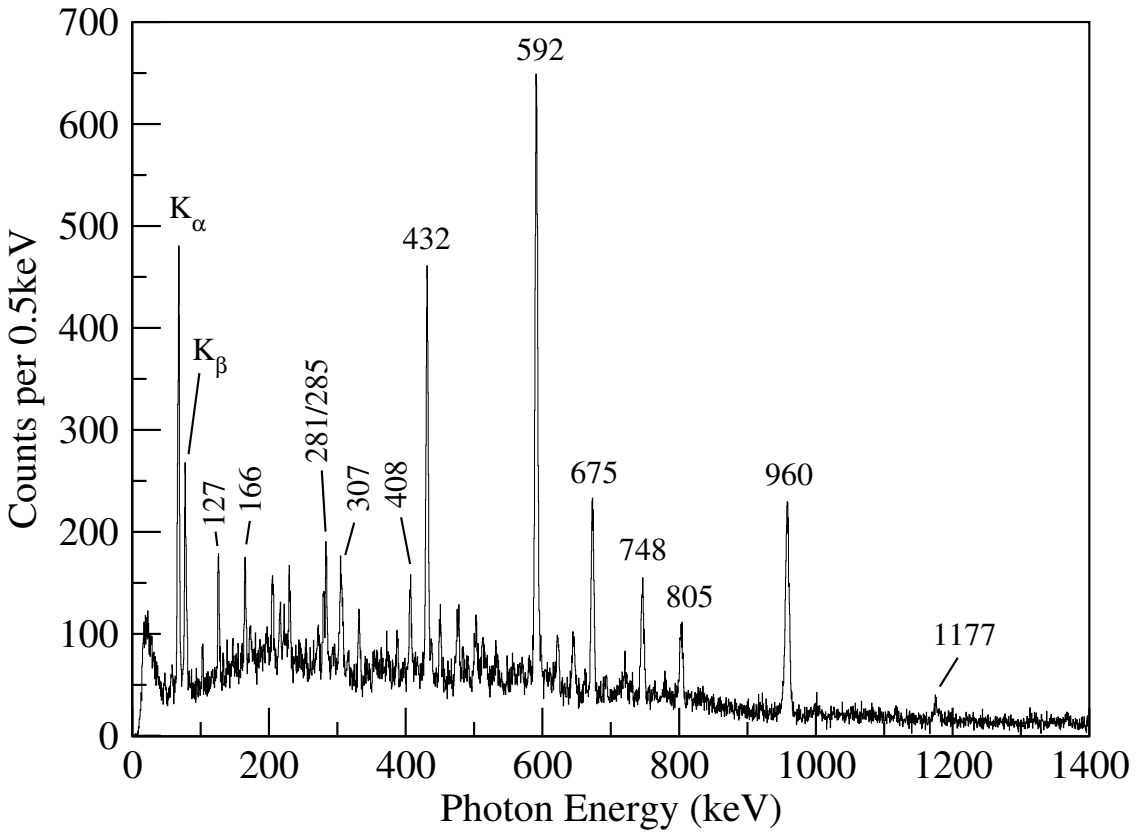

Figure 6.2: Prompt single photon emission detected in JUROGAM II, which was RDT with an isomeric state of ^{173}Au^m (E_α = 6739(4)keV). Photon emission correlated with the ground state α decay of ^{173}Au (E_α = 6688(4)keV) was subtracted from this spectrum, which had a very subtle effect in suppressing the γ rays feeding ^{173}Au^g.

recoil-α decay of ^{173}Au^m, prompt γ radiation that feeds this particular state was selected, and shown in figure 6.2.

Kondev *et al.* had reported six γ rays that feed this isomeric state of ^{173}Au^m. The spin of this state was assumed to have the configuration $\pi^{-1}(h_{11/2})$, based from proton and α decay measurements of ^{173}Au's α-emitting parent nuclide, ^{177}Tl^m [5], as well as systematic trends of heavier gold isotopes (see the Discussion chapter for details). In this work, a total of 46 γ rays were found in delayed coincidence with the α decay of ^{173m}Au, along with a further 8 tentative decays. These are listed in table 6.2, along with their relative intensities, the transition's initial I_i^π and final I_f^π state, if known, and the intensity angular ratios between JUROGAM II's rings. In this work, the angular intensity ratio, R_A, is given

Type	E_{expt} (keV)	$E_{literature}$ (keV)	I_{expt} (%)	$I_{literature}$ (%)
K_{α_1}	68.75(15)	68.81	55(8)	48.8(12)
K_{α_2}	66.79(19)	66.99	23(4)	28.9(7)
$K_{\beta_1,\beta_3,\beta_5}$	77.79(16)	77.85	16.1(16)	17.4(3)
$K_{\beta_2,\beta_4,O_{1,2}}$	80.03(23)	80.21	5.9(9)	4.78(12)

Table 6.1: Comparison between the measured and documented X-ray energy and relative intensities when tagging on the decay of ^{173}Au^m. Literature values were obtained from the Table of Isotopes [24].

by

$$R_A = \frac{I_{\gamma,133.57^\circ}(E_\gamma)}{I_{\gamma,90^\circ}(E_\gamma)}, \tag{6.1}$$

where $I_{\gamma,133.57^\circ}(E_\gamma)$ and $I_{\gamma,90^\circ}(E_\gamma)$ are the γ ray intensities, of energy E_γ, detected in ring 2, and in rings 3 and 4 of JUROGAM II, respectively. Ring 1 was not in use in this experiment. In order to obtain typical stretched quadrupole and stretched dipole transition values, the angular intensity ratios of ^{170}Os were measured in this experiment. Performing this was made with difficulty, due to significant contamination from other α decaying isotopes of similar energy, along with a long half-life (9(1) s [6]) and low branching ratio (8.6(6)% [6]). When utilising the RT technique, it became clear that ^{170}Os was as strongly populated as ^{173}Pt, and was most likely formed via the ^{92}Mo(^{84}Sr, $\alpha 2p$)^{170}Os reaction. Thus, the angular intensity ratios were measured; the strongest stretched dipole ($E1$) (947keV, $5^{(-)} \rightarrow 4^+$ [57]) transition had a ratio of 0.63(3), and the stretched quadrupole $E2$ (463keV, $4^+ \rightarrow 2^+$ [57]) γ transition had a ratio of 0.88(3). It must be noted however, that the ratios for unstretched dipole transitions are very similar to that of stretched quadrupole transitions.

The measurement of the energies and the relative intensities of the Au X-rays was performed, and is summarised in table 6.1. It was found that the measured energies and intensities were consistent with the documented values [24], implying that no evidence of γ rays of similar energy were present.

Multiple coincidence events taking place in JUROGAM II was investigated. Approximately 1.2×10^5 recoil-α(^{173}Au^m)-tagged $\gamma\gamma$ coincidences were collected within an α decay search time of 100ms, and sorted into a $E_{\gamma 1}E_{\gamma 2}$ matrix using the GRAIN software package

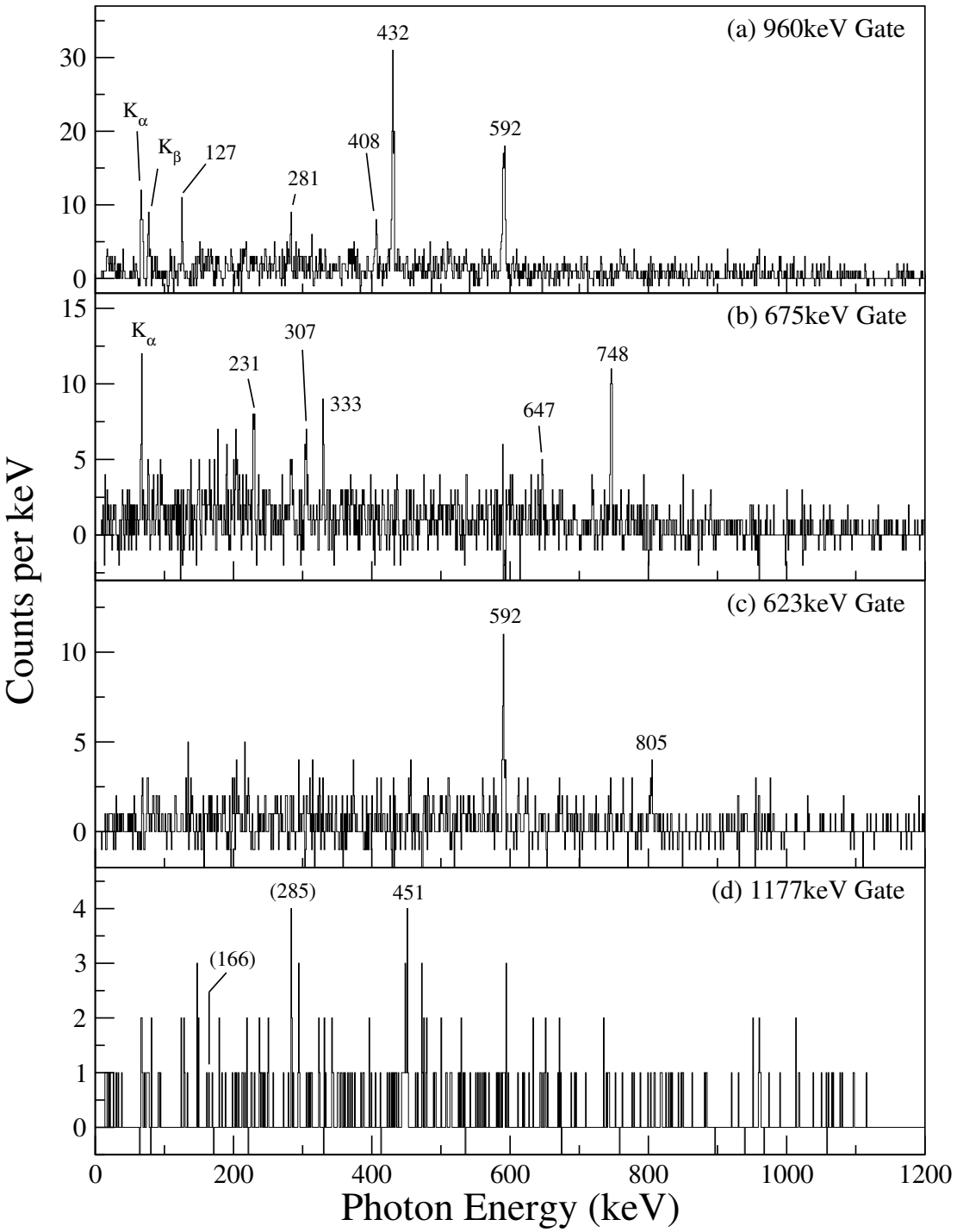

Figure 6.3: Background subtracted γ-ray coincidence spectra correlated with the RDT of ^{173}Au^{m}. (a) The projection of the 960-keV γ gate, showing all of the yrast transitions. Non-yrast transitions were presented utilising three different γ gates: (b) Coincidences with the 675-keV transition, (c) the 623-keV transition, and (d) the 1177-keV transition.

[54], before being analysed using the ESCL8R RadWare software package [43]. The search time was chosen to maximise the statistics, and the background was sufficiently low within this time range. Coincidences between two germanium detectors were satisfied when the time difference between the two hits was within ±120ns, in order to minimise random coincidences. By analysing the coincidences between various γ decays, a level scheme was able to be constructed, shown in figure 6.6; the increased amount of statistics available had led the expansion of the level scheme further than was previously reported.

Table 6.2: A list of γ ray energies, E_γ, their initial (E_i) and final (E_f) excitation energies, their angular intensity ratio R_A, their intensity I_γ, and their spin and parity assignments that feed the $h_{11/2}$ isomer of $^{173}\mathrm{Au}^m$. The γ intensities were measured from the $\alpha(^{173}\mathrm{Au}^m)$-tagged γ spectrum. All of the above transitions, including tentative γ rays, were included, even if they were not placed in the level scheme.

E_γ (keV)	E_i (keV)	E_f (keV)	I_γ (%)	R_A	$I_i^\pi \rightarrow I_f^\pi$
103.6(3)			1.9(4)		
126.97(17)	2606	2479	6.9(5)	0.58(14)	$(23/2^+) \rightarrow (21/2^+)$
165.94(18)			6.0(5)	1.02(25)	
173.3(3)			2.3(4)		
180(1)			∼1		
187(1)			∼1		
191(1)			∼1		
198.1(4)			1.8(5)	1.0(6)	
205.82(21)			6.2(6)	0.80(20)	
216.85(25)			3.8(5)	0.9(4)	
224.1(3)			2.9(5)	1.3(6)	
230.82(20)	(1868)	1636	7.6(6)	1.03(27)	$(19/2^-) \rightarrow (15/2^-)$
245.8(4)			1.9(4)		
254(1)			∼1		
272.6(3)			3.4(6)	1.5(6)	
281.1(4)	2479	2198	5.4(8)	0.58(13)	$(25/2^+) \rightarrow (23/2^+)$
284.53(25)			8.2(9)		
295.5(4)			2.4(5)		
306.70(19)	(1943)	1636	11.2(8)	0.80(17)	
316.5(4)			2.5(5)		
332.84(21)	(1868)	1535	6.3(6)		$(19/2^-) \rightarrow (17/2^-)$
343.2(4)			2.1(5)		
357.8(4)			2.7(5)		

Continued on the next page

Table 6.2 – *Continued from the previous page*

E_γ (keV)	E_i (keV)	E_f (keV)	I_γ (%)	R_A	$I_i^\pi \rightarrow I_f^\pi$
366(1)			∼1		
373.3(4)			2.6(5)		
388.1(3)			3.3(5)		
407.78(20)	2606	2198	9.5(8)	0.86(20)	$(25/2^+) \rightarrow (21/2^+)$
432.34(15)	2198	1766	46.6(24)	0.75(7)	$(21/2^+) \rightarrow (19/2^-)$
438.7(3)			4.3(6)	1.4(7)	
451.39(21)	(1843)	(1391)	7.6(7)	1.1(4)	
477.43(24)			9.2(8)	0.87(25)	
484.7(5)			3.4(7)		
491.7(6)			2.6(6)		
503.4(3)			6.7(8)	0.53(18)	
513.9(3)			6.4(7)	0.8(3)	
533.9(7)			2.3(6)		
558.4(6)			2.4(7)		
571.3(5)			3.2(7)		
583.1(4)			4.2(7)		
592.30(15)	806	214	100(5)	0.82(6)	$(15/2^-) \rightarrow (11/2^-)$
598.5(6)			4.2(9)		
623.06(28)	(2234)	1611	8.2(9)	0.85(24)	
646.86(25)	1535	889	9.9(9)	1.2(3)	$(17/2^-) \rightarrow (13/2^-)$
664.1(5)			3.6(7)		
674.63(16)	889	214	36.4(21)	0.96(11)	$(13/2^-) \rightarrow (11/2^-)$
693.1(5)			3.2(7)		
720.5(5)			4.1(7)		
747.81(19)	1636	889	22.2(14)	0.62(13)	$(15/2^-) \rightarrow (13/2^-)$
782(1)	(2393)	1611	∼1		
804.81(22)	1611	806	14.7(11)	0.92(20)	$(17/2^-) \rightarrow (15/2^-)$
959.86(16)	1766	806	69(4)	0.91(8)	$(19/2^-) \rightarrow (15/2^-)$
1001(1)			∼3		
1026(1)			∼2		
1177.5(6)	(1391)	214	7.9(9)	0.7(4)	

The yrast structures had been extended to an excitation energy of 2606keV and a tentative spin assignment of $(25/2^+)$, when taking into account of the reported excitation energy of 214(13)keV for the $h_{11/2}$ isomer [5]. Tentative evidence of inter-structure transi-

tions was found with the 280- and 126-keV γ rays, with angular intensity ratios consistent to that of stretched dipole character, forming an alternative decay path than the more direct 408-keV γ ray, consistent to be that of a stretched quadrupole transition, though with a large uncertainty. Summation of the two γ-ray energies yielded a value consistent to the lone 408-keV transition; both decay paths were also in coincidence with the 432-, 960- and 592-keV γ-ray cascade.

Figure 6.3 shows some of the background subtracted E_γ projections when gating on certain γ ray energies. Coincidence relationships reveal that the 592- and 675-keV transitions were not in coincidence with each other, confirming this observation made in previous work [4]. Further to this, no evidence of collective structure feeding the $h_{11/2}$ state was found, illustrating the marked transition towards single-particle spherical excitations taking place in the nucleus.

It ought to be noted that, when compared to Kondev's work, a few differences have been observed after analysing and interpreting this work. Owing to the limited amount of statistics in the author's experiment, spin assignments of the excited states feeding the $h_{11/2}$ isomer were assumed, and parity assignments were not disclosed. In this work, more data available allowed one to see similarities to the level-scheme structure in heaver even-N isotopes of Au, coupled with measurements of the angular intensity ratios. Most transitions, however, still have large uncertainties with the values of R_A, and thus the multipolarity of these transitions could not be decided conclusively.

The 804-keV transition was found to be in coincidence with the 592-keV transition, but not with the 960-keV transition. Angular intensity ratios suggest this γ decay is of quadrupole character, though due to the lack of statistics, the possibility of this transition being a stretched dipole could not have been eliminated. That said, based on the systematics of heavier, spherical-like isotopes of gold, such as ^{195}Au [63], the spin and parity of the state has been tentatively assigned to $(17/2^-)$. Two other, much weaker, independent transitions were found to be feeding this $(17/2^-)$ state, though the characteristics of these transitions could not have been established.

Coincidence analysis with the 675-keV γ ray revealed five new feeding transitions;

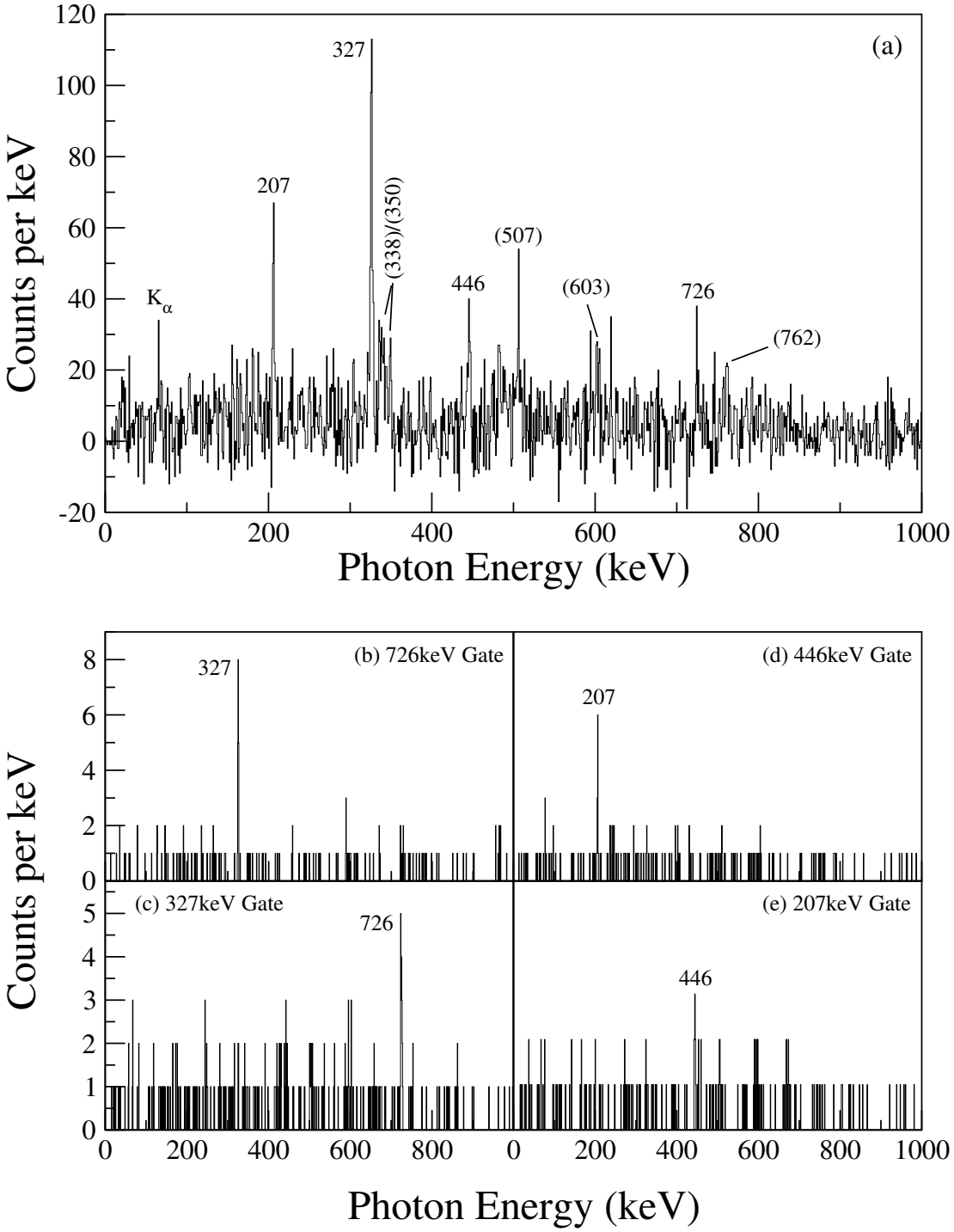

Figure 6.4: (a) High-spin α-decay subtracted γ-ray spectrum correlated with the RDT of $^{173}Au^{g}$ between the time-difference conditions of 20–200ms. All transitions, including tentative ones, are indicated here. The projections of the (b) 726-keV γ gate, (c) the 327-keV γ gate, (d) the 446-keV γ gate, and (e) the 207-keV γ gate.

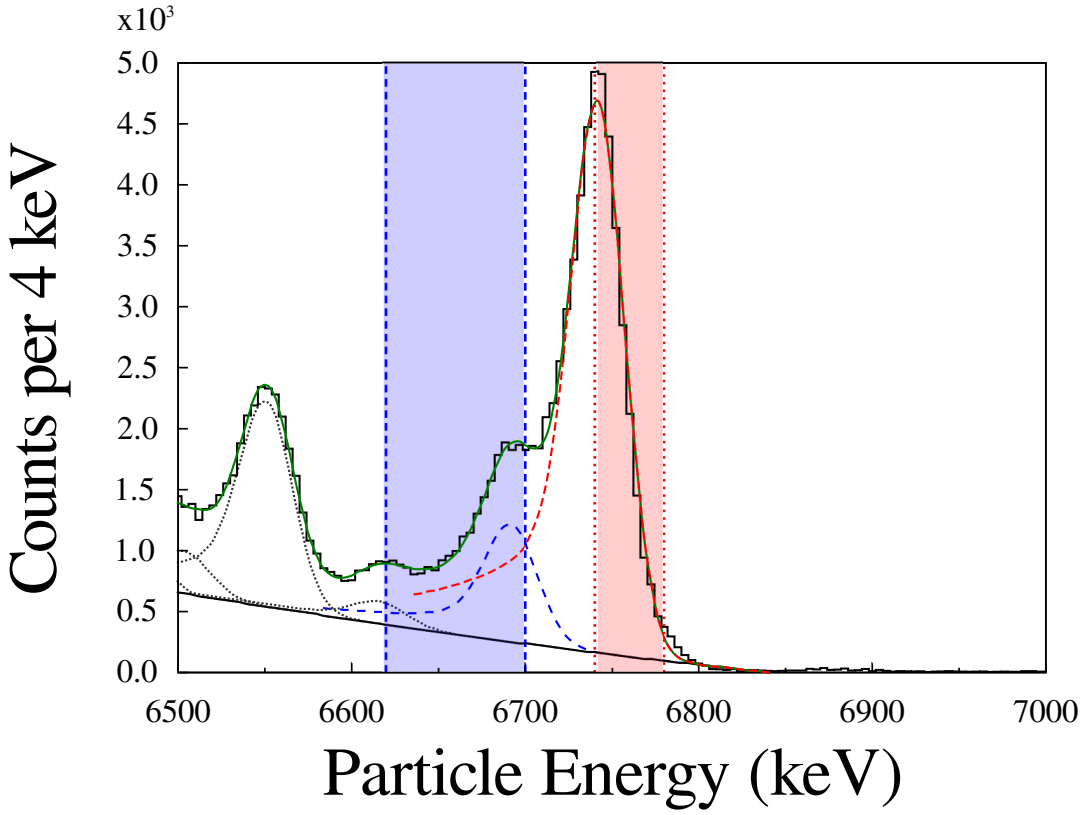

Figure 6.5: Illustration of the gating technique used to produce γ-ray spectra feeding the low-spin state of ^{173}Au. The individual peaks are given in dashed lines with the high-spin and low-spin energy peaks corresponding to the red and blue lines, respectively. The total summation is indicated by the solid green line. The projection and background gates are given by the shaded blue and red regions, respectively.

detailed analysis had shown that the 748- and 647-keV transitions were not mutually coincident, and neither were the 333-, 231- and 307-keV transitions. It is worth noting, however, that the statistics were very limited; the proposed sequence of transitions of the latter three γ rays are therefore tentative at best. Observations of the 307-keV transition in coincidence with the 647-keV γ ray suggests an extra decay path connecting the $(15/2^-)$ state to the $(17/2^-)$ state, yielding an anticipated γ energy of 102keV, in which no evidence was found. For an $M1$ transition, this decay is highly converted; the calculation using *BrIcc* (Band *et al.* [64] and Raman *et al.* [65] Internal conversion coefficients) [66] gives an internal conversion coefficient to be roughly $\alpha_{ICC} \approx 7$, explaining the γ-ray's absence in the spectrum. It is assumed, based on similar studies of the heavier gold isotope ^{189}Au [67], that the 675-keV γ ray is mixed, emanating from a tentatively-assigned

E_γ (keV)	E_i (keV)	E_f (keV)	I_γ (%)	$I_i^\pi \rightarrow I_f^\pi$
207.19(17)	207	0	2.0(3)	$(3/2^+) \rightarrow (1/2^+)$
326.97(17)	327	0	6.6(8)	$(5/2^+) \rightarrow (1/2^+)$
338(1)			2.2(3)	
350(1)			1.2(2)	
446.31(22)	654	207	2.7(4)	$(7/2^+) \rightarrow (3/2^+)$
484(1)			1.5(3)	
507.0(3)			2.7(4)	
603(1)			1.7(3)	
725.83(24)	1053	327	1.9(3)	$(9/2^+) \rightarrow (5/2^+)$
762(1)			1.7(3)	

Table 6.3: A list of γ ray energies, E_γ, their initial (E_i) and final (E_f) excitation energies, singles intensity I_γ, and their spin and parity assignments that feed the $s_{1/2}$ state of ^{173}Au.

$(13/2^-)$ state. Angular intensity ratios have tentatively placed the 748-, 647-, 231- and 333-keV transitions coming from the $(15/2^-)$, $(17/2^-)$ states, respectively, and the latter two transitions from the $(19/2^-)$ state.

Other notable coincidences include the 451-keV and the 1177-keV transitions; the very low statistics for this pair of γ rays have prevented further analysis beyond the identification of the cascade. It is assumed therefore, that the lack of other transitions in the spectra suggests that this cascade also feeds the isomer directly. It has also been noted that two other transitions, the 166- and 284-keV γ rays, are in mutual coincidence, and incidentally, the summation of these two energies yields the 451-keV γ ray. These two transitions have been tentatively assigned to feed the 1177-keV state. however, there were insufficient data in the γ-γ projection of the 1177-keV transition to cleanly observe coincidences between these transitions.

Transitions that feed the low-spin structure of ^{173}Au were also investigated. The RDT technique was employed to search for γ decays in JUROGAM II that were correlated with the low-spin α decay of ^{173}Au ($E_\alpha = 6690(5)$keV [10]). The challenge was to make this unambiguous selection without contamination from the more dominant high-spin α decay. As the high-spin decay has the larger energy, significant contributions from its low-energy tail were present, along with the small energy separation between the two decay energies of these two states. This was mitigated by "background" subtracting the

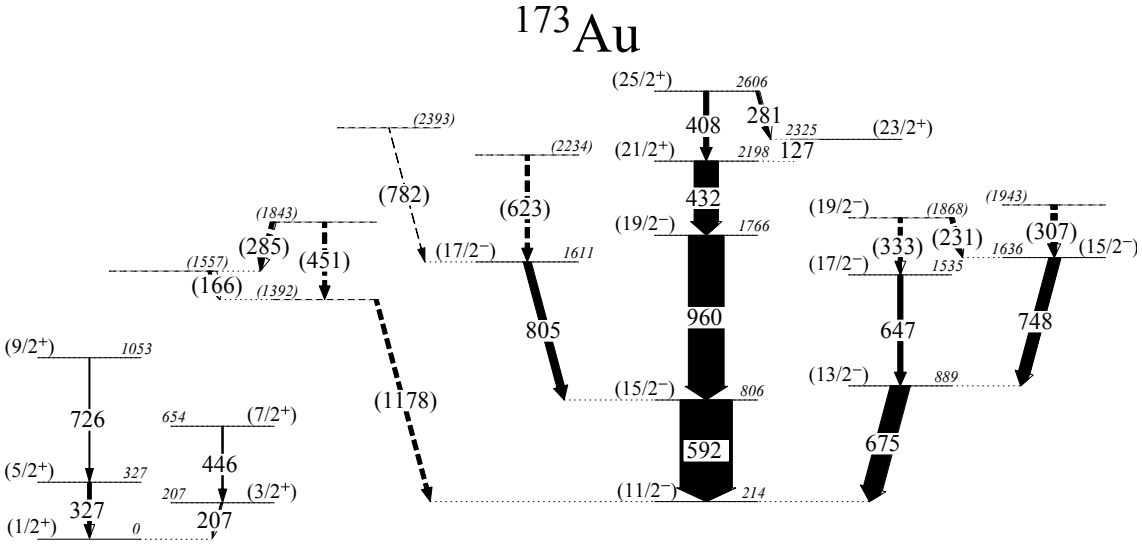

Figure 6.6: Level scheme of ^{173}Au, showing transitions feeding the high-spin isomer and the low-spin ground state. No collective behaviour was observed. The arrow widths are proportional to the intensities of the γ rays. Tentative assignments are marked in parentheses.

high-spin decay γ decays from the RDT low-spin spectrum in JUROGAM II, making sure that the "background" gate does not cover any part of the low-spin α decay peak. An illustration of this gating technique is shown in figure 6.5. In addition, the longer lifetime of the low-spin state ($T_{1/2}$ = 25(1) ms [4]) allows a cut-off time gate to be imposed that only permits decay events to proceed if the time difference was larger than 20ms, which cuts out a larger fraction of the high-spin decay than it does for the low-spin state. The upper limit of this time gate was set to 200ms.

Figure 6.4(a) shows the high-spin decay subtracted γ-singles spectrum taken in delayed coincidence with a recoil-α event corresponding to the decay of ^{173}Au^{g}; the reported transitions, which were not previously observed, are summarised in table 6.3. Due to the lack of statistics, a more relaxed time gate (between 0–200ms) was utilised when producing a $E_{\gamma 1}E_{\gamma 2}$ matrix. The subtraction gate was not used here, as it had little impact on the quality of the final spectra. The coincidence spectra are presented in figures 6.4(b–e); the two left panels show the coincidence between the 327-keV and the 726-keV γ rays, and the two right panels show the coincidence between the 207-keV and the 445-keV γ rays. The ordering of the transitions were based on their singles intensity, and is presented in

the level scheme, alongside the high-spin feeding transitions of ^{173}Au, shown in figure 6.6.

6.2 The high- and low-spin α-decay Chain of ^{173}Au

With the low production cross sections of ^{173}Au, coupled with the low α-decay branching ratios of its descending nuclei, long experimental runs were required in order to produce sufficient quantities of this nucleus. There were also considerable experimental challenges in establishing clean decay correlations with multiple descending nuclei; correlations containing relatively long-lived α-decaying isotopes can become obscured by other processes, such as recoil intrusion and charged-particle decays coming from more dominant reaction channels.

In this work, with the level of statistics available, the decay chains of four isotopes have been successfully correlated, starting from the high-spin α decay of ^{173}Au^m. However, contamination from the α decay of the strongest reaction channel, ^{173}Pt, was present, and could be considered to be *mis-correlations*. This could be mitigated by reducing the search time of the DSSD tagger; however, the long-lived nuclei towards the end of this decay chain have limited this possibility. A compromise was made, with the tagger-window set to be 15s in order to unambiguously correlate decays of up to four generations of nuclei. Finally, all of the subsequent α decays must be observed inside the same pixel as the recoil event.

Figure 6.7 presents the high-spin α decay chain. The "mother" α decays (recoil-α) were selected within a 100ms time gate since its recoil implantation, and is presented in figure 6.7(a). The decays that were observed following the correlated recoil-α decay of ^{173}Au^m are shown in figure 6.7(b). The "daughter" decays (recoil-α-α) were selected provided that the "mother" decay event had passed an additional energy gate consistent to the α energy peak of ^{173}Au^m, while careful to not include the low-spin α decay peak. No additional time gate was utilised; it was found that it harmed the statistics more than it did suppressing the main contaminant, ^{173}Pt, which arises due to mis-correlated events with the ^{173}Au^m decay taking place inside a DSSD pixel.

The measured decay peak energy of the daughter was consistent to previous observations of the α decay of ^{169}Ir^m. The half-life of this decay was taken as the time difference

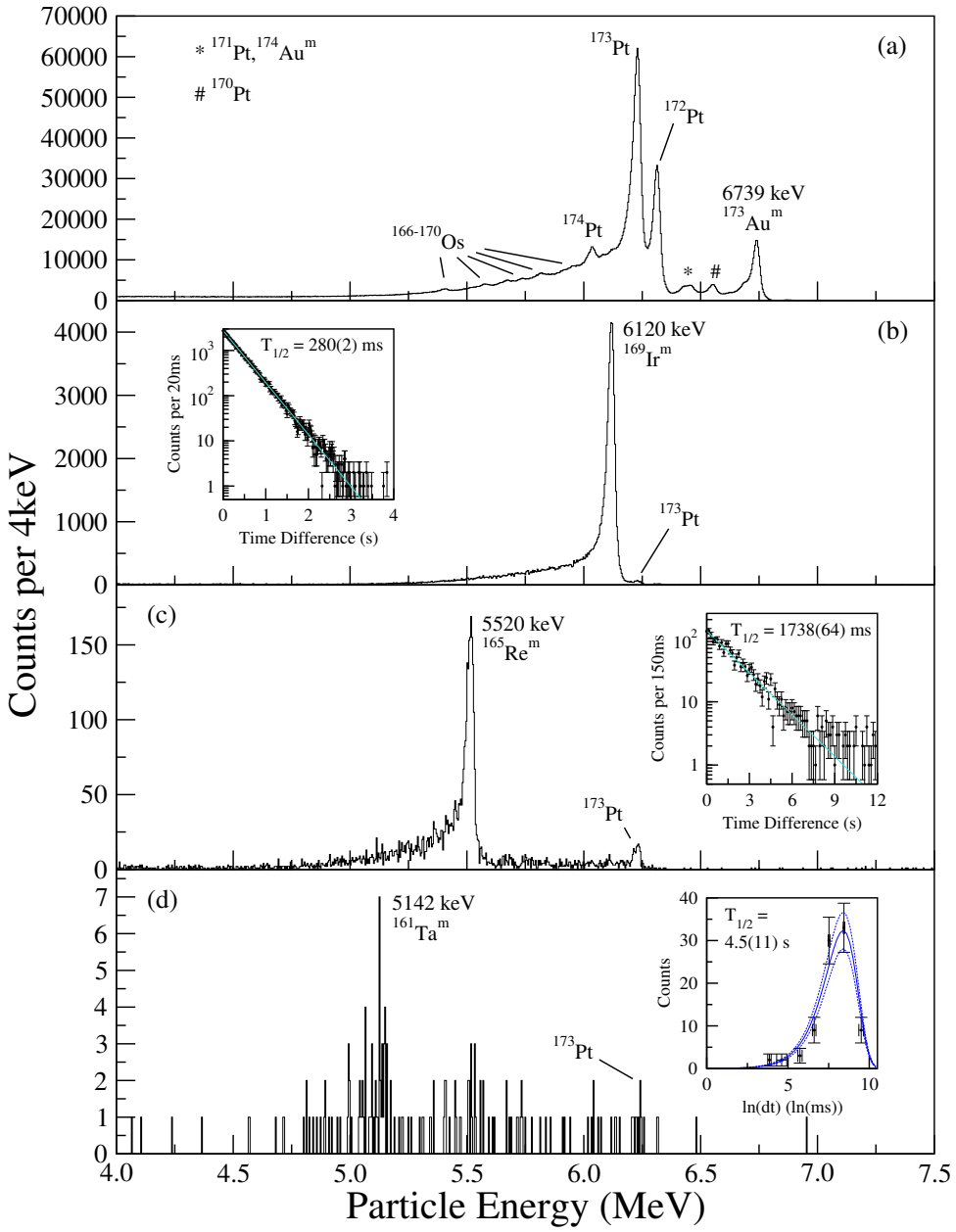

Figure 6.7: Spectra showing (a) all decays observed in the DSSD following a recoil implantation within 100ms of the decay, taking place in the same pixel of the DSSD; (b) all second generation decays following the detection of the α decay of ^{173}Au^m that occur in the same pixel with the aforementioned time gate; (c) all third generation decays following the detection of the α decays of both ^{173}Au^m and ^{169}Ir^m, occurring in the same pixel and aforementioned time gate; (d) all fourth generation decays following the detection of the α decays of ^{173}Au^m, ^{169}Ir^m and ^{165}Re^m, occurring in the same pixel and aforementioned time gate. The insets in each panel correspond to the energy-gated time-difference spectra for each of the nuclei of interest, and also include least-squares fits (solid cyan and blue lines) for each data set.

between the mother decay and the daughter decay events, and was corrected for random correlations (described in Random Events, chapter 5, section 4). The α-decay branching ratio, b_α, was measured by acquiring the total volume of the full-energy daughter α-decay peak, in addition to the estimation of escaped α particles, V_D, before dividing this value by the integration of the mother α decay peak of interest, within the confines of a predetermined energy gate, V_M. As the number of escaped α particles have been accounted for, the DSSD efficiency reduces to its charge collection component, which has been assumed to be 100% inside the depletion region (*i.e.* $\epsilon_{\mathrm{DSSD}} = 1$). The result was then corrected for mis-correlated events, which is given by the ratio between the corrected and measured half-lives of the interested nucleus. The complete formula can be expressed as

$$b_\alpha = \frac{V_D}{V_M} \cdot \frac{T_{1/2,corrected}}{T_{1/2,measured}} \cdot \frac{1}{1-F}, \tag{6.2}$$

where the α escapes ratio, F, can be ignored when including the number of escapes in V_D. The results of the decay energy, half-life and branching ratio for each nuclide are presented in table 6.4, and were found to be consistent to previous reports for the half-life and branching ratio of $^{169}\mathrm{Ir}^m$.

No further time gates were applied either to both the "grand-daughter" (recoil-α-α-α) or the "great grand-daughter" (recoil-α-α-α-α) spectra, presented in figures 6.7(c) and 6.7(d), respectively. The "grand-daughter" decays had the additional condition that an energy gate overlapping the α peak of $^{169}\mathrm{Ir}^m$ was passed, in addition to the above described gates. Measurements of its energy, corrected half-life and α-decay branching ratio were consistent to the decay of the high-spin isomer of $^{165}\mathrm{Re}^m$. The "great grand-daughter" decays had a fourth condition, in that an energy gate overlapping the α decay peak of $^{165}\mathrm{Re}^m$ must also be passed. A peak with the aforementioned measurements being consistent to previous work [68, 6], the α decay had been unambiguously assigned, for the first time, to the high-spin decay of $^{161}\mathrm{Ta}^m$. The limits of observation have started to become apparent here; the low α branching ratios of $^{165}\mathrm{Re}^m$ and $^{161}\mathrm{Ta}^m$ had substantially reduced the amount of statistics for these two spectra. It is also worth noting that the background in the $^{161}\mathrm{Ta}^m$ spectrum is proportionally larger than earlier generations, and

	This Work			Literature		
Nucleus	E_α(keV)	$T_{1/2}$(ms)	b_α(%)	E_α(keV)	$T_{1/2}$(ms)	b_α(%)
^{173}Au^m	6739(4)	12.2(1)		6737(4)[10]	14(1)[4]	92(13)[5]
^{169}Ir^m	6120(4)	280(2)	78(6)	6119(9)[6]	308(22)[6]	84(8)[5]
^{165}Re^m	5520(6)	1738(64)	13(1)	5518(5)[6]	2000(300)[6, 59]	13(3)[6]
^{161}Ta^m	5142(6)	4500(1100)	7(3)	5148(5)[68]	2870(120)[69, 70]	5*[7]

Table 6.4: A list of measurements of the α decay energy, half-life and decay branching ratio of the decay chain originated from the high-spin state of ^{173}Au, along with literature values obtained from previous work. *This value was calculated using theoretical partial half-lives of the α and β^+-EC decay of ^{161}Ta^m.

can be attributed to the longer-lived "great grand-daughter" nucleus.

The half-life of ^{161}Ta^m was measured using the maximum-likelihood method [71], due to the lack of statistics. Instead of fitting the time difference distribution over a linear scale (shown as insets in figures 6.7(b) and 6.7(c)) using the radioactive decay formula

$$N(t) = N_0 e^{-\lambda t}, \tag{6.3}$$

the data were sorted into a logarithmic time scale, and the equation becomes

$$\frac{dN}{d\theta} = n\lambda e^{\theta} e^{-\lambda e^{\theta}}, \tag{6.4}$$

where $\theta = \ln(t)$. The decay curve instead gives a peak with a shape independent of the half-life; the most probable value, the peak centroid, is given by $\ln(\tau)$. This is shown in figure 6.7(d). Corrections due to random events were then applied to the measured half-life, by using an empirically determined relation used, which shows, to an approximation, the correlation between the measured and the corrected half-lives of short- and long-lived nuclei:

$$R(T_{1/2}) = x \cdot e^{ax}, \tag{6.5}$$

where $a = 1.79(10) \times 10^{-4}$ ms^{-1}. A plot of this function over some least-squares fitted half-lives in this work is shown in figure 6.8.

Decay spectroscopy emanating from the low-spin state of ^{173}Au was also investigated.

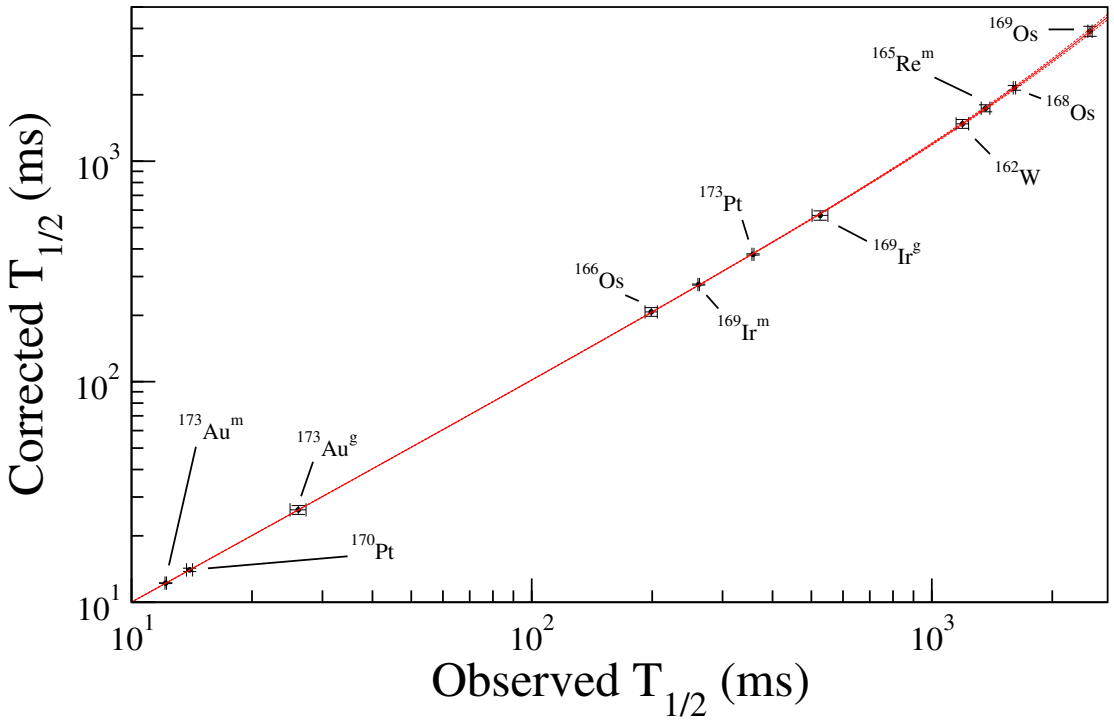

Figure 6.8: A comparison between the least-squares fitted raw half-life measurements to the corrected half-life versions. An empirical fit function is shown as the solid curve.

Unfortunately, due to the much stronger populated high-spin α decay of ^{173}Au, where its low energy tail overlaps the energy of the low-spin state, acquiring clean spectra was not possible due to this contamination. This was particularly challenging in terms of measuring a reliable half-life and α-decay branching ratio for these states. However, for the case of the half-life measurements, one can use a two-exponential least squares fit to the time difference spectra, and fixing the half-life of one of the terms to that measured in the high-spin decay spectra

$$N_{h.s}(t) + N_{l.s}(t) = N_{0,h.s}e^{-\lambda_{h.s}t} + N_{0,l.s}e^{-\lambda_{l.s}t}, \tag{6.6}$$

where $h.s$ and $l.s$ correspond to the high-spin and low-spin contributions, respectively. In the case of the α-decay branching ratio, the relative intensities of the low-spin and high-spin α decay peaks in the gated spectrum were compared in order to estimate the number of escapes that correspond to each decay.

The contamination due to the high-spin α decay was mitigated by imposing an addi-

tional condition that γ rays feeding the low-spin state of ^{173}Au were selected in JUROGAM II. This technique was used before [72] in order to produce clean spectra of the nucleus of interest in the DSSD. Gating on the 327- and 726-keV transitions gave the cleanest results, as the 207-keV γ ray is a multiplet, with one feeding the high-spin state of ^{173}Au, and the other transitions were too weak to enhance the low-spin α decay of ^{173}Au. The one exception was for the half-life measurements of ^{169}Ir^{g} and ^{173}Au^{g}, which did not use the γ-gated technique, but the former still had an energy gate overlapping the α decay peak of ^{173}Au^{g}. The reasoning for this is that the above technique could be used with much more statistics; γ gating suppresses a large amount of statistics, due to the relatively low efficiency of JUROGAM II.

Figure 6.9 shows the 327- and 726-keV γ-gated DSSD spectra corresponding to the "mother" decay (figure 6.9(a)), the "daughter" decay (figure 6.9(b)) and the "grand-daughter" decay (figure 6.9(c)), with all requiring a recoil-α time gate of between 7ms and 100ms. The "daughter" decay was selected by imposing an energy gate overlapping the α decay peak of ^{173}Au^{g}, in addition to the aforementioned gates, showing the decay peaks coming from both the low-spin and high-spin states of ^{169}Ir. The "grand-daughter" decay had an additional energy gate that included the decay of the low-spin state of ^{169}Ir, as well as the region of escaped α particles. A new energy peak was observed that had a larger energy than that of the high-spin α decay of ^{165}Re, which is now barely visible in the spectrum. Thus, for the first time, the new α decay peak has been assigned as the low-spin α decay of ^{165}Re. Measurements of these three α decays are presented in table 6.5; the measurements of ^{173}Au^{g} and ^{169}Ir^{g} were found to be consistent with values measured in previous work.

In order to rule out the possibility that any of these α decays exhibit fine structure, or if ^{173}Au has any isomers, spectra from the germanium detectors located in the focal plane were analysed. γ decays in the planar and clover germanium detectors that were in coincidence with each α decay of the high-spin or low-spin states, and of each generation, were investigated. Various trigger widths were utilised, including long widths in excess of 1ms, in order to see if any long-lived isomers existed. However, no evidence of any delayed

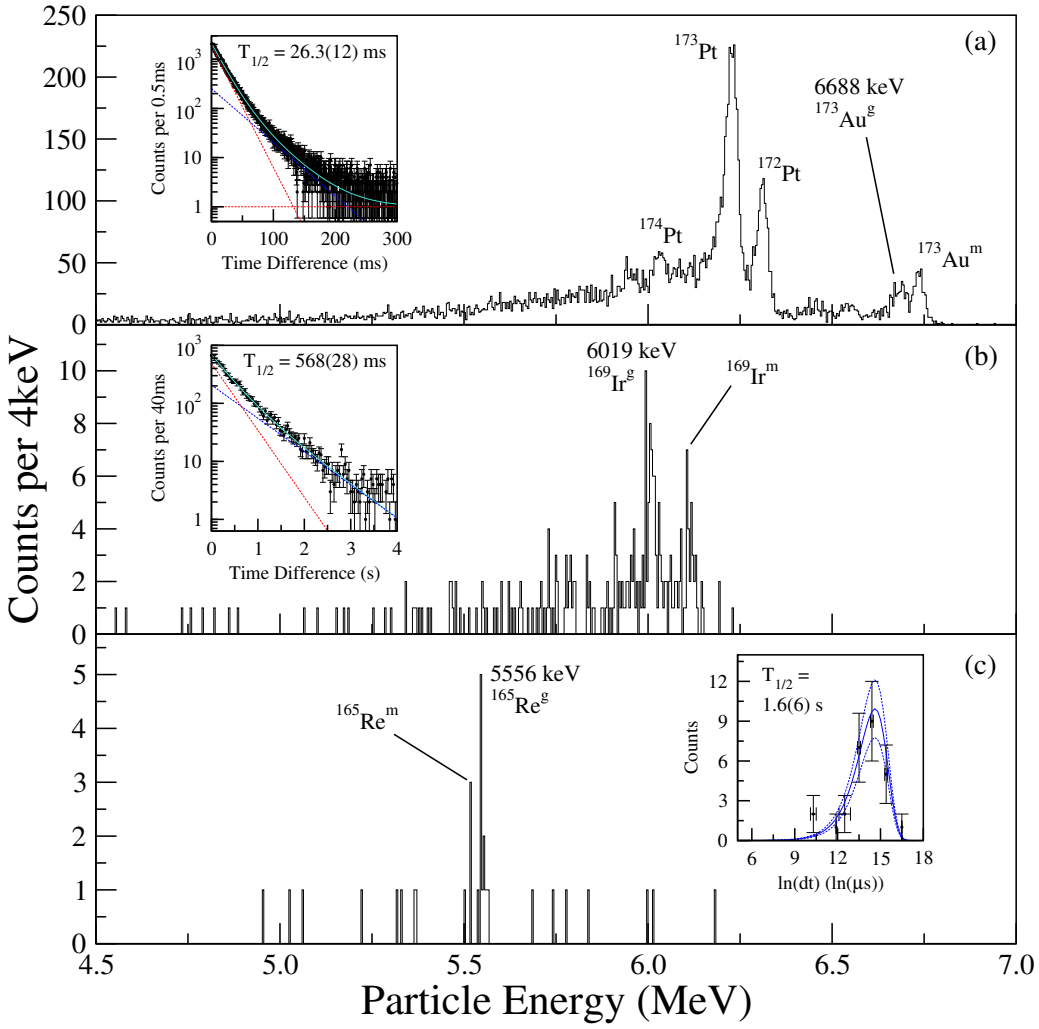

Figure 6.9: Spectra showing (a) all decays observed in the DSSD that took place between 7ms and 100ms after the recoil implantation into the same pixel of the DSSD, as well as an additional condition of being in coincidence with either the 327- or 726-keV γ rays in JUROGAM II; (b) all second generation decays following the detection of the α decay of ^{173}Au^{g} that occur in the same pixel with the aforementioned gating conditions; (c) all third generation decays following the detection of the α decays of ^{173}Au^{g}, ^{169}Ir^{g}, and all escaped charged particles in the second generation spectrum, occurring in the same pixel as well as all other aforementioned gating conditions. The insets in each panel correspond to (a) the energy-gated time-difference spectra of ^{173}Au^{g}, containing the high-spin decay component, without using any γ gates; (b) the energy-gated time-difference spectra of ^{169}Ir^{g}, containing the high-spin decay component, without using any γ gates, but still includes the ^{173}Au^{g} energy gate; (c) the maximum likelihood time-difference spectra of ^{165}Re^{g}, which was γ gated, and includes all of the other aforementioned gates. All of the insets have had a two-component least-squares fits performed to the data (solid cyan lines), with the high-spin and background component shown as dotted red lines, and the low-spin contribution presented as dotted blue lines.

	This Work			Literature		
Nucleus	E_α (keV)	$T_{1/2}$ (ms)	b_α (%)	E_α (keV)	$T_{1/2}$ (ms)	b_α (%)
^{173}Au^g	6688(4)	26.3(12)		6683(9)[5, 10]	25(1)[4]	94(19)[5]
^{169}Ir^g	6019(4)	568(28)	57(9)	6005(8)[5]	640^{+460}_{-240}[5]	50(18)[5]
^{165}Re^g	5556(6)	1600(600)	14(8)			

Table 6.5: A list of measurements of the α decay energy, half-life and decay branching ratio of the decay chain originated from the low-spin state of ^{173}Au, along with literature values obtained from previous work. The decay of ^{165}Re^g is a newly reported transition in this work.

or isomeric γ decay was observed in either the clover detector, or the planar detector. This is not conclusive evidence for the late generation α decays, such as ^{165}Re and ^{161}Ta, due to the very low amount of statistics available, and therefore the possibilities of fine-structure could not have been eliminated.

6.2.1 Searching for the p-emission of ^{173}Au

The possibility for the observation of p-emission emanating from the low-spin state of ^{173}Au was investigated. Both the high-spin and the low-spin states of ^{173}Au are proton unbound, with the proton separation energy for the low-spin state to be measured at $-993(22)$keV and $-1206(18)$keV for the high-spin isomer [5]. However, as the decay process requires a change of angular momentum by 5 units, along with a parity change, the unbound proton experiences a large centrifugal potential on top of the Coulomb barrier that it must penetrate. Therefore, finding decays corresponding to the low-spin state may be possible.

The analysis was performed by looking for recoil-p-α correlations, using the α decay of ^{172}Pt ($E_\alpha = 6314(4)$keV [73]) as if it was the "daughter" decay. As the emission of the proton will have an energy that overlaps the escaped region, decays were vetoed with the P-i-N diode detectors in order to suppress escaped events. Figure 6.10 shows this spectrum, expanded to look at the energy region of interest. It can be noted that no p-emission events were observed. However, with the separation energy known, its partial half-life can be estimated using empirical methods.

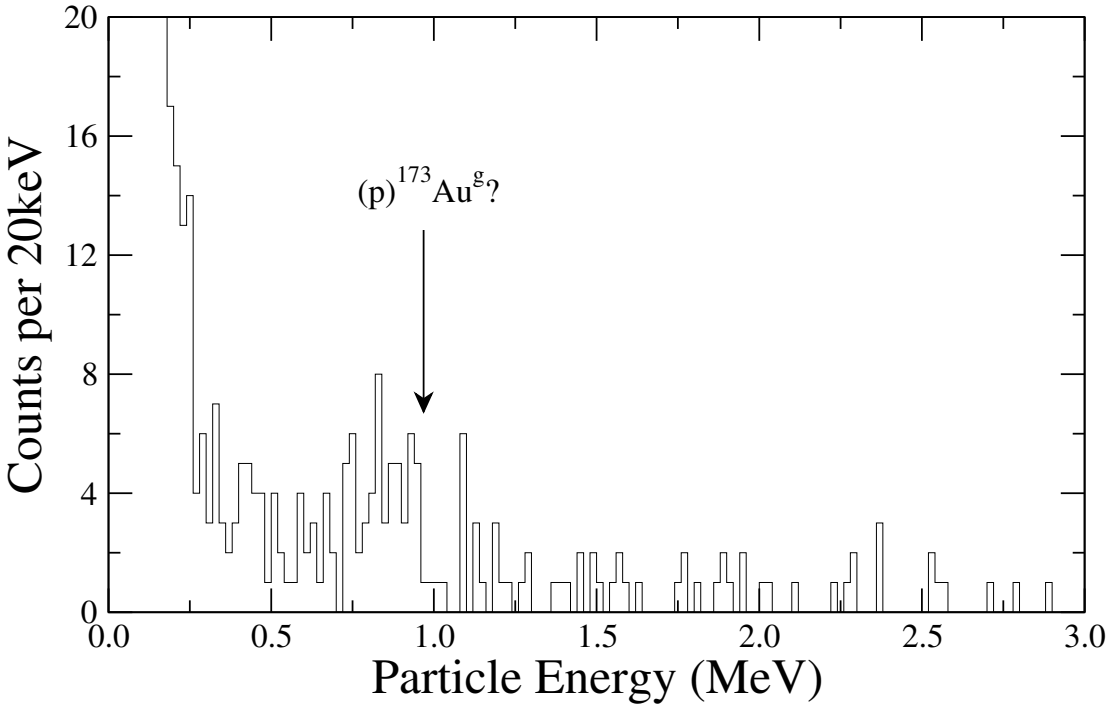

Figure 6.10: "Mother" decay spectrum showing the P-i-N vetoed particle decays that have been correlated within 300ms of the proceeding α decay of ^{172}Pt, and preceded, within 100ms, by a recoil implantation. All correlations must take place within the same pixel in the DSSD.

Assuming that ^{173}Au is spherical, and using the empirical formula shown in Proton and Neutron Emission (chapter 3, section 5) the partial half-life of the p emission of the low-spin state of ^{173}Au has been estimated to be 12^{+8}_{-5} s. Similarly, the high-spin partial p-emission half-life has also been determined to be 468^{+303}_{-184} s. When compared to the α decay branch, the p-emission branching ratio is exceedingly small, even for the low-spin state of ^{173}Au, which would explain the lack of any evidence of p-emission.

Chapter 7

Spectroscopy of the Neutron Deficient Nucleus ^{173}Pt

Like its neighbouring isobar ^{173}Au, the amount of recoil-correlated α events coming from ^{173}Pt, also had yielded approximately an order of magnitude more than was previously obtained by Joss *et al.* [9].

The recoiling ^{173}Pt nuclei were produced via the $2p1n$ evaporation channel from the compound formation of ^{176}Hg*. Approximately 1×10^{7} correlated ^{173}Pt recoil-α events were recorded. Using the reported transmission efficiency of RITU that was given as 49.0(10)%, along with the measured full energy α peak ratio of 53.2(6)% (consistent to the calculated value of 59(6)%) and the α-decay branching ratio of 86(4)% for ^{173}Pt [74, 6, 10], the production cross section was estimated to be 280(32)μb at E_{beam} = 392MeV, and 216(25)μb at E_{beam} = 400MeV.

7.1 In-beam Analysis

Owing to the larger production cross section of ^{173}Pt compared to ^{173}Au, much more recoil-α(^{173}Pt) decay tagged statistics were collected. Figure 7.1(a) shows the total decay spectrum occurring within 1.5s of a recoil implantation in the same pixel in the DSSD. An additional energy gate was placed that overlapped the characteristic α decay of ^{173}Pt; the measurement of this energy peak in this work was found to be 6235(4)keV, which was

Type	E_{expt} (keV)	E_{lit} (keV)	I_{expt} (%)	I_{lit} (%)
K_{α_1}	67.00(15)	66.83	51(4)	49.0(12)
K_{α_2}	65.34(17)	65.12	24.8(24)	28.9(7)
$K_{\beta_1,\beta_3,\beta_5}$	75.75(15)	75.63	18.1(11)	17.4(3)
$K_{\beta_2,\beta_4,O_{1,2}}$	78.31(16)	77.90	6.0(4)	4.73(12)

Table 7.1: Comparison between the measured and documented X-ray energy and relative intensities of Pt. An inconsistency was noticed when comparing the intensities of the $K_{\beta_2,\beta_4,O_{1,2}}$ X-rays, indicating the possibility of an overlapping γ ray of similar energy.

consistent to the previous reported value of 6232(4)keV [10]. The resulting spectrum in figure 7.1(b) show γ-ray singles in delayed coincidence with the α decay of ^{173}Pt, which had been background subtracted from the main contaminant coming from ^{172}Pt, due to the overlapping of its low-energy tail in the energy gate. The same energy gate, but without using any background subtraction, was used to produce a time-difference spectrum between the recoil implantation and the α decay occurring in the same pixel. Several decay curves were required to be used in order to include the contaminants of ^{172}Pt and even ^{173}Au in the least-squares fit. The resulting fit function, and its individual contributions, are shown as an inset to figure 7.1(a). The corrected half-life measurement of ^{173}Pt was found to be 378(3)ms, which was consistent with the previous value of 382(2)ms [10].

A list of all γ-ray transitions measured in ^{173}Pt, including tentative and unplaced γ rays, are presented in table 7.2. A total of 92 γ rays were identified, which include confirmed doublets for the 547-, 634- and 662-keV γ rays and a confirmed triplet for the 530-keV γ ray in the γ-γ analysis, greatly expanding from the previously reported number of 29 γ rays (including reported confirmed doublets) by Joss *et al.* [9]. The intensities and energies of the X-rays were also measured, and are presented in table 7.1. Tentative evidence of an overlapping γ ray with an energy roughly to that of the K_β X-ray may be present, based off the comparison of the relative intensities of the documented K_β X-rays [24] to their measured values in this work. However such γ rays that overlap in energy with the X-rays can only be tentatively assigned, and requires γ-γ analysis to select them with less ambiguity.

Multiple γ-ray coincidence events were investigated. Approximately 2×10^6 γ-γ events

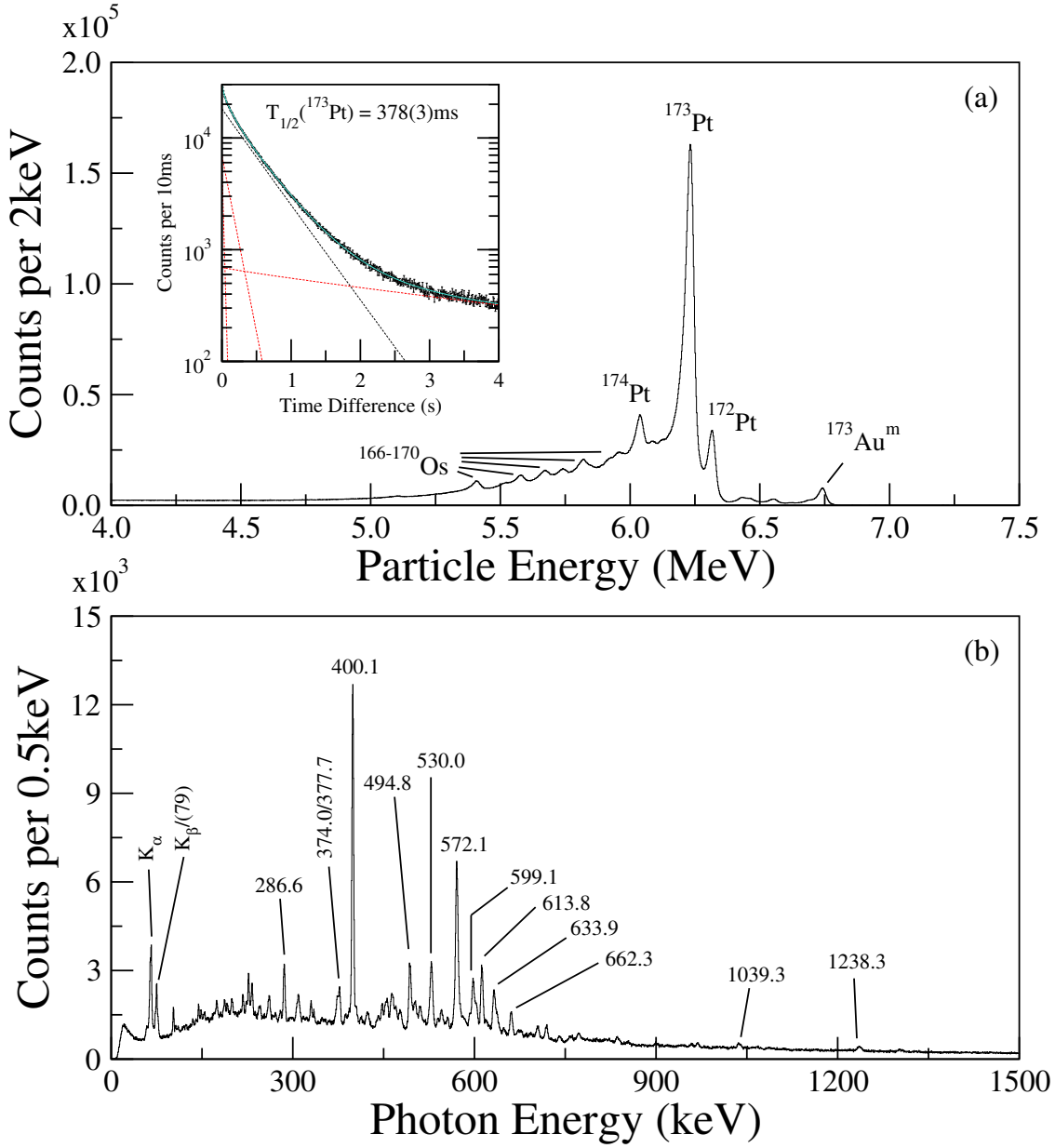

Figure 7.1: (a) Total decay spectrum occurring within 1.5s of a recoil implantation taking place in the same pixel of the DSSD. The inset shows the time difference spectra between the recoil and the α-decay event of ^{173}Pt, showing contributions due to contaminants in the least-squares fit that was performed to the data. (b) ^{173}Pt RDT singles spectrum in JUROGAM II, which was background subtracted from its main contaminant ^{172}Pt. The inset in panel (a) shows the time-difference spectrum when gating on the α-decay peak of ^{173}Pt, as well as a least-squares fit that was performed to the data (solid cyan line), along with the following components to the fit: The nucleus of interest (dotted blue), the two contaminants (dotted red) and the background (dotted red, smaller gradient).

were recorded when tagging on the α decay of ^{173}Pt, which was background subtracted from its main contaminants. An $E_{\gamma 1}$-$E_{\gamma 2}$ matrix was sorted using the aforementioned conditions, as well as a time gate between each coincident event in JUROGAM II. The method of constructing a level scheme for ^{173}Pt remains the same as that described in the in-beam ^{173}Au analysis.

DCO ratios were able to be measured due to the increased amount of statistics available in ^{173}Pt. Compared to utilising angular intensity ratios for γ-ray singles, DCO ratios give a better indication of the transition's multipolarity, without requiring reference values of confirmed stretched dipole and stretched quadrupole transitions. A high degree of orientation is required in order to obtain reliable results; a γ gate was placed on the transition above the decay of a state, therefore, before taking measurements on the transition of interest. This was performed using a $E_{\gamma_{133.57^\circ}}$–$E_{\gamma_{104.5^\circ+75.5^\circ}}$ matrix, where $\gamma_{133.57^\circ}$ and $\gamma_{104.5^\circ+75.5^\circ}$ correspond to detections in JUROGAM II's second ring and the combined pair of JUROGAM II's third and fourth ring, respectively. The DCO ratio is given by

$$R_{DCO} = \frac{V\left(\gamma 2_{133.57^\circ}\right) \text{gated on } \gamma 1\left(104.5^\circ + 75.5^\circ\right)}{V\left(\gamma 2_{104.5^\circ+75.5^\circ}\right) \text{gated on } \gamma 1\left(133.57^\circ\right)} \cdot \epsilon, \tag{7.1}$$

where $V(\gamma 2)$ is the total number of counts of the γ-ray transition of interest in the projected spectrum, when gating on a transition $\gamma 1$ in the other ring(s) in JUROGAM II. The efficiency correction factor, ϵ, is given by

$$\epsilon = \frac{\epsilon_{\gamma 2}^{projection}\left(104.5^\circ + 75.5^\circ\right) \cdot \epsilon_{\gamma 1}^{gate}\left(133.57^\circ\right)}{\epsilon_{\gamma 2}^{projection}\left(133.57^\circ\right) \cdot \epsilon_{\gamma 1}^{gate}\left(104.5^\circ + 75.5^\circ\right)}, \tag{7.2}$$

where $\gamma 1$ and $\gamma 2$ represent the gated and projected transition, respectively.

Typical values of the γ-gated DCO ratios are $\sim$ 1.0 for pure stretched quadrupole transitions (or pure unstretched dipoles) and $\sim$ 0.6 for pure stretched dipole transitions. Mixed multipole transitions, depending on the mixing coefficient δ_{mix} results in DCO ratios varying between roughly these two extremes. The values for the two DCO ratio extremes depend on the angular geometry of the spectrometer used. With a similar angular setup of JUROGAM II to that of the NORDBALL array [75], these above values can be assumed to

give benchmark properties of γ transitions with different multipolarities. The measured DCO ratios, R_{DCO}, in this work are presented in table 7.2.

Table 7.2: A list of γ ray energies, E_γ, their initial (E_i) and final (E_f) excitation energies, their DCO ratio R_{DCO}, their intensity I_γ, and their spin and parity assignments that were measured from the $\alpha(^{173}\text{Pt})$-tagged γ spectrum of ^{173}Pt. All transitions were included, even if they were not placed in the level scheme.

E_γ (keV)	E_i (keV)	E_f (keV)	I_γ (%)	R_{DCO}	$I_i^\pi \rightarrow I_f^\pi$
∼79					
103.40(14)	103	0	4.5(2)	0.45(20)	$(9/2^-) \rightarrow (7/2^-)$
107.17(16)			1.2(1)		
111.00(23)			0.5(1)		
120.15(21)			0.5(1)		
140.55(19)			0.7(1)		
145.16(15)	(2369)	(2224)	2.6(1)	0.4(4)	$(25/2^-) \rightarrow (23/2^-)$
149.06(15)	(2036)	1887	1.9(1)	0.4(4)	$(21/2^-) \rightarrow (19/2^-)$
154.82(18)			0.8(1)		
170.6(3)			0.5(1)		
173.0(3)			0.7(1)		
175.35(23)			0.7(1)		
188.10(16)	(2224)	(2036)	2.7(2)	0.8(5)	$(23/2^-) \rightarrow (21/2^-)$
193.30(22)			1.0(1)		
199.90(19)			1.3(1)		
218.58(15)			3.3(2)		
224.05(20)			1.4(1)		
228.38(18)			1.9(1)		
233.48(14)	(2603)	(2369)	7.3(3)	0.7(4)	$(27/2^-) \rightarrow (25/2^-)$
238.0(3)			0.7(1)		
245.70(23)			1.0(1)		
259.9(3)			1.1(2)		
262.7(3)			1.1(2)		
279.3(4)			0.5(1)		
286.63(15)			5.9(3)		
298.1(3)			0.7(1)		
307.2(4)			0.7(1)		
310.89(19)	(1532)	1221	4.7(3)	0.6(4)	
313.5(4)			1.4(3)		
324.10(26)			0.9(1)		
331.19(15)	580	249	5.3(3)	0.54(18)	$(11/2^+) \rightarrow (13/2^+)$

Continued on the next page

Table 7.2 – *Continued from the previous page*

E_γ (keV)	E_i (keV)	E_f (keV)	I_γ (%)	R_{DCO}	$I_i^\pi \rightarrow I_f^\pi$
335.60(19)			2.0(2)		
348.7(3)			0.8(1)		
354.8(3)			0.7(1)		
360.25(15)			0.5(1)		
373.96(18)	1022	649	3.0(2)	0.40(26)	$(15/2^+) \rightarrow (17/2^+)$
377.69(17)			3.2(2)		
388.5(4)			0.7(2)		
394.56(17)			3.4(2)		
400.08(16)	649	249	100(4)	1.09(7)	$(17/2^+) \rightarrow (13/2^+)$
405.38(15)	(2467)	(2062)	5.6(3)	1.1(7)	
413.8(3)			0.8(2)		
425.35(21)			2.7(2)		
442.52(17)	1022	580	5.1(3)	1.2(7)	$(15/2^+) \rightarrow (11/2^+)$
449.60(26)			2.8(2)		
455(1)			10(1)		
466.00(15)	1488	1022	10.3(6)	1.1(4)	$(19/2^+) \rightarrow (15/2^+)$
478.85(20)			3.5(3)		
494.83(14)	598	104	29.6(13)	1.01(21)	$(13/2^-) \rightarrow (9/2^-)$
503.26(15)			10.8(5)		
511.18(15)	2936	2424	8.7(4)	1.2(3)	$(29/2^-) \rightarrow (25/2^-)$
529.99(23)	2424	1895	13.5(18)	1.23(29)	$(25/2^-) \rightarrow (21/2^-)$
529.84(24)	(2062)	(1532)	11(3)	1.3(5)	
∼530			6(4)		
542.1(3)			1.9(2)		
∼546	1369	(824)	2.3(10)	1.1(6)	$(19/2^+) \rightarrow (15/2^+)$
546.4(8)	2510	1963	5.4(9)	1.1(6)	$(27/2^+) \rightarrow (23/2^+)$
556.45(19)			3.7(3)		
568.1(3)			4.2(6)		
572.12(27)	1221	649	81(4)	1.09(15)	$(21/2^+) \rightarrow (17/2^+)$
∼575	(824)	249	∼2		$(15/2^+) \rightarrow (13/2^+)$
577.89(19)			7.3(4)		
583.75(19)			4.6(4)		
593.65(19)	1963	1369	5.5(4)	1.2(6)	$(23/2^+) \rightarrow (19/2^+)$
599.10(15)	2434	1835	22.4(10)	1.2(4)	$(29/2^+) \rightarrow (25/2^+)$
604.31(16)	3038	2434	11.8(6)	1.2(5)	$(33/2^+) \rightarrow (29/2^+)$
613.78(14)	1835	1221	27.0(12)	1.02(19)	$(25/2^+) \rightarrow (21/2^+)$
632.8(3)	3672	3038	6.5(10)	1.2(3)	$(37/2^+) \rightarrow (33/2^+)$
633.95(18)	1232	598	20.2(22)	1.2(3)	$(17/2^-) \rightarrow (13/2^-)$

Continued on the next page

Table 7.2 – *Continued from the previous page*

E_γ (keV)	E_i (keV)	E_f (keV)	I_γ (%)	R_{DCO}	$I_i^\pi \rightarrow I_f^\pi$
639.30(17)			9.7(5)		
649.2(3)			1.6(2)		
660.7(9)	4334	3672	1.6(6)		$(41/2^+) \rightarrow (37/2^+)$
661.63(22)	1895	1232	12.0(16)	1.3(4)	$(21/2^-) \rightarrow (17/2^-)$
673.15(29)			2.7(3)		
678.15(28)			2.9(3)		
694.95(28)			2.1(2)		
706.15(16)	(2768)	(2062)	6.2(3)	0.67(29)	
720.36(16)	1369	649	7.6(4)	0.7(4)	$(19/2^+) \rightarrow (17/2^+)$
741.90(22)	1963	1221	3.3(3)	0.9(6)	$(23/2^+) \rightarrow (21/2^+)$
760.70(28)			2.2(2)		
774.20(21)	1022	249	3.8(3)	0.8(6)	$(15/2^+) \rightarrow (13/2^+)$
838.35(22)	1488	649	4.5(3)		$(19/2^+) \rightarrow (17/2^+)$
854.50(29)	(2087)	1232	2.5(2)		
902.6(4)	(1551)	649	1.9(2)		
960.5(4)			2.1(2)		
970.70(25)	2192	1221	3.3(2)		
1039.30(24)			5.5(3)		
1067.9(4)	(2289)	1221	3.2(2)		
1089.9(5)			2.4(2)		
1112.3(7)			1.4(2)		
1238.30(24)	1887	649	6.1(3)	0.4(3)	$(19/2^-) \rightarrow (17/2^+)$
1305.8(3)	1955	649	3.3(2)		
1330(1)			1.0(2)		

γ-γ coincidence spectroscopy was performed by analysing a $E_{\gamma 1}$-$E_{\gamma 2}$ matrix, which was tagged on the α decay of ^{173}Pt, and was background subtracted. By placing an energy gate on the 604-keV γ ray, one was able to reproduce the previously reported yrast band, and is shown in figure 7.2(a). This band has been assumed to be based on the $\nu i_{13/2}$ configuration, which comprises of the 400-, 572-, 614-, 599-, 604-, 634- and 662-keV transitions.

A second band was also reported by Joss *et al.*, but the sequence of transitions were unplaced in the level scheme of ^{173}Pt. Figure 7.2(b) presents the projection when gating on

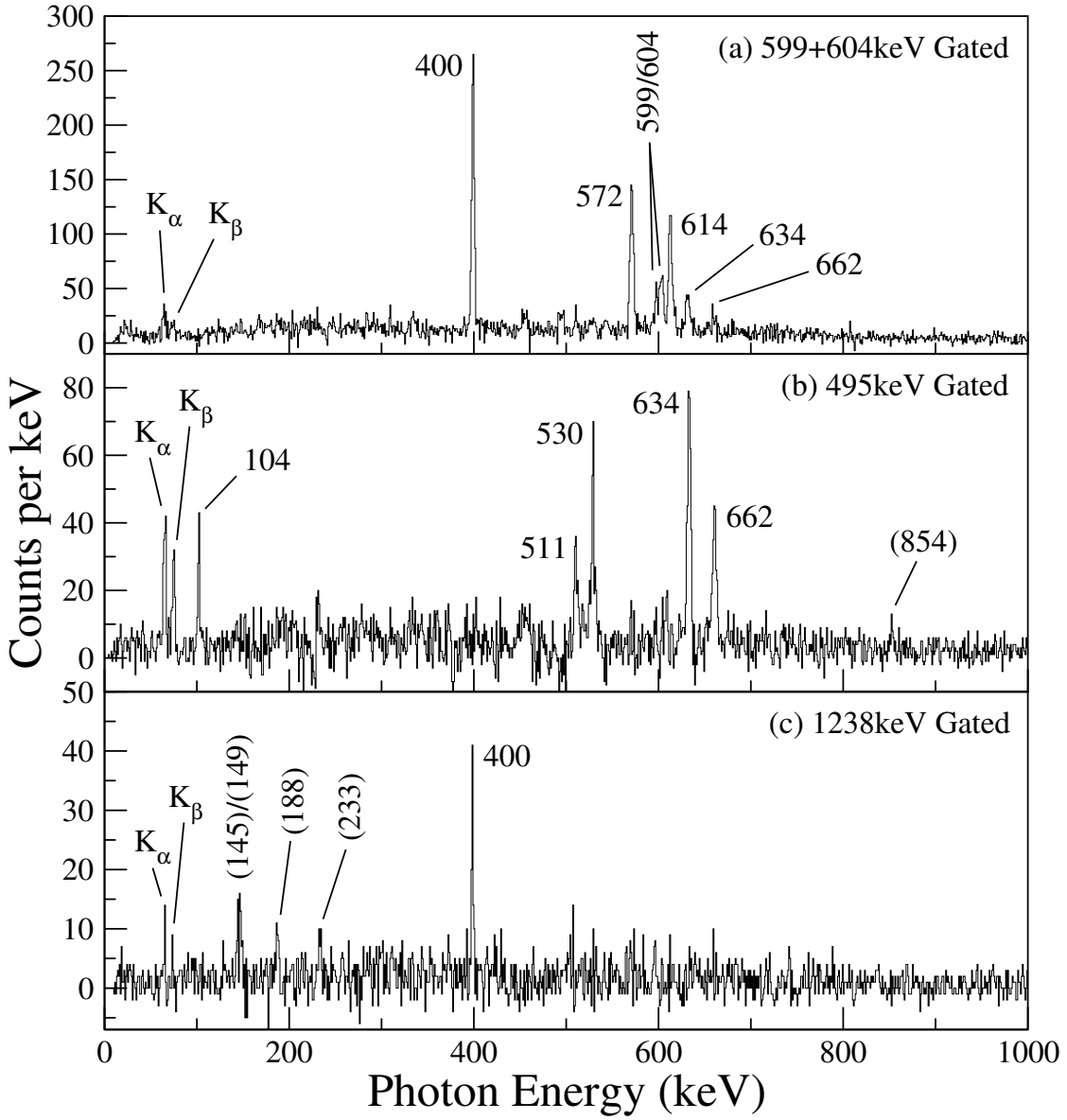

Figure 7.2: Background subtracted γ-ray coincidence spectra correlated with the RDT of ^{173}Pt. (a) The projection of the 599- and 604-keV γ gates, showing all of the yrast transitions. (b) The projection of the gated 495-keV transition, showing a non-yrast band, and includes a low energy 104-keV γ ray. (c) Coincidences with the 1238-keV dipole transition, showing exotic, non-yrast transitions feeding it.

the 495-keV transition. The 634-, 662-, 530- and 511-keV γ rays were observed, along with a weaker, 854-keV transition that was found to be in coincidence with the 634- and 495-keV transitions, and a low-energy γ ray of 104-keV, which was also previously unreported. Gating on this transition reproduces this band, albeit with much lower statistics; the additional analysis in the focal plane was required in order to determine this band's decay

path, as no evidence of yrast transitions were present in this spectrum.

Weaker, non-yrast structures were also found. One particular decay sequence of note was the high-energy 1238-keV dipole transition; coincident γ rays when gating on this transition are shown in figure 7.2(c), and shows the 400-keV γ ray, along with non-yrast transitions. The 149-, 188-, 145- and 233-keV γ rays were found to be mutually coincident, with the 145- and 233-keV γ rays also in coincident with another high-energy 1306-keV transition, which has been assumed to be of dipole nature also. No evidence of other feeding transitions were found. Despite these findings, reliable placements in the level scheme have been challenging, due to the insufficient statistics available, as well as no observable evidence of an inter-linking transition feeding the state that decays via a 1306-keV γ ray. The presented placements and ordering in the level scheme, therefore, are only tentative.

Additional, side-feeding bands have been established for the first few levels. The first tentatively exhibits multiple transitions from a single state, which may indicate another positive parity band. The 466- and 443-keV γ rays were found to be de-exciting to states within this band, along with the inter-band 774- and 331-keV γ rays. An additional 840- and 374-keV transitions were also found, but due to the low statistics, their placement are tentative. A second band de-excites via inter-band 742-, 720 and 575-keV transitions that feed the yrast band, which compete with the self-coincident 547-keV and 594-keV transitions that de-excite within the band.

7.2 Focal Plane Spectroscopy of ^{173}Pt

Possible isomeric transitions taking place in ^{173}Pt were investigated. This was performed in the focal plane detector chamber, where spectroscopic studies can be performed for states with half-lives comparable to, or greater than, the recoiling particle's time-of-flight. This consequently constrains the range of half-lives that can be measured for these states; short-lived isomers decay *in-flight*, therefore such decay will be unable to be detected inside the focal plane.

Figure 7.3(a) shows the singles spectrum in the planar germanium detector taken in

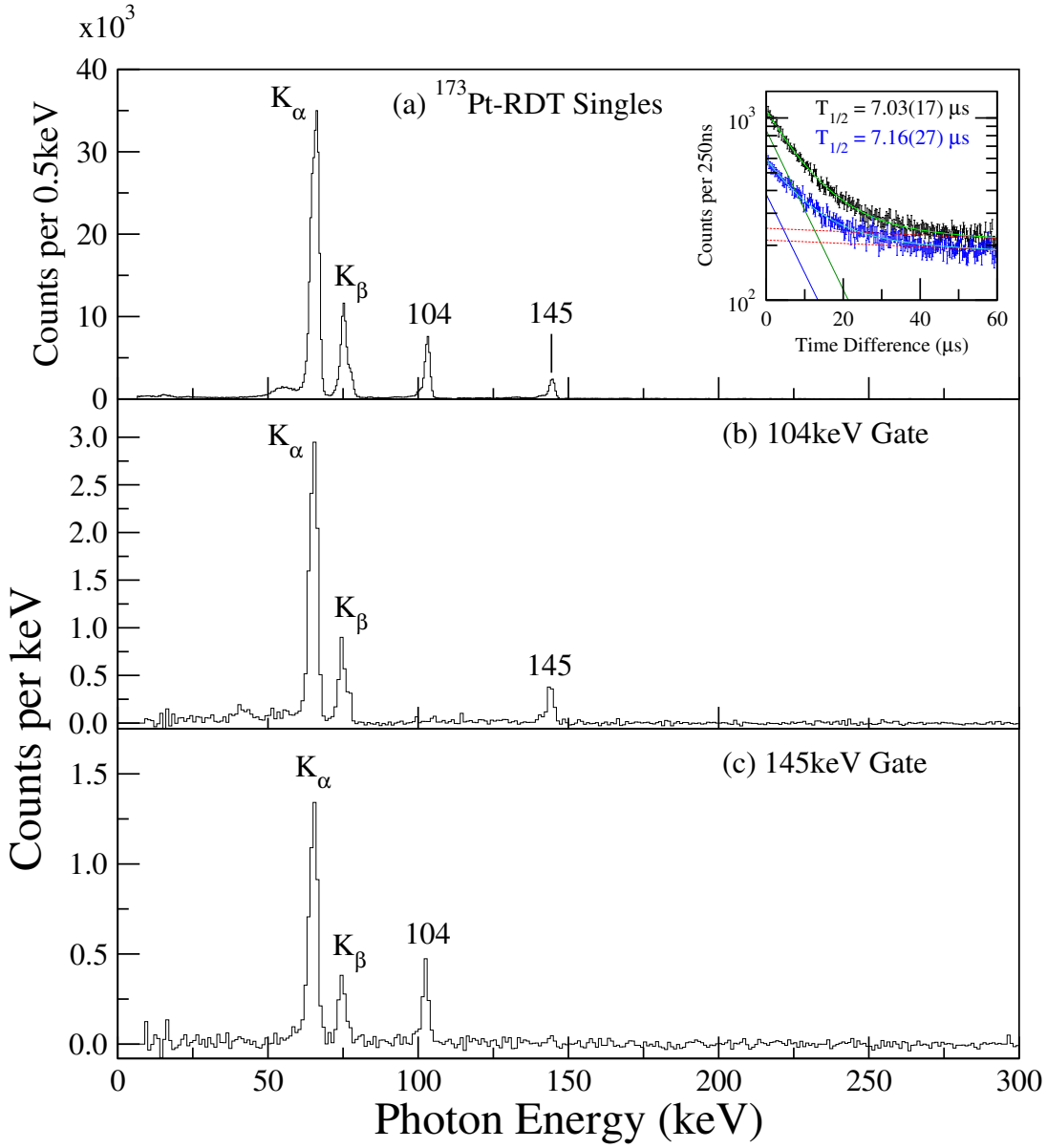

Figure 7.3: (a) Planar germanium γ-ray singles spectrum correlated with the RDT of ^{173}Pt, with the triggering conditions between the DSSD and the focal plane germanium detectors occurring within 30μs after the recoil implantation. The inset shows the time difference spectra for both the 104-keV (black) and 145-keV (blue) transitions, with a least-squares fit performed to the data, which includes the components of the 104-keV (green lines) and the 145-keV (blue lines) transitions, along with their corresponding backgrounds (dotted red lines). The projection of the (b) 104-keV and (c) 145-keV γ gates, showing coincidences taking place in the planar detector.

delayed coincidence with a recoil-α decay correlation of ^{173}Pt taking place within the same pixel of the DSSD. The triggering conditions between the DSSD and the focal plane germanium detectors must also occur within 30μs after the recoil implantation. Two γ

rays, of energies 104- and 145-keV, were observed in both focal plane germanium detectors, along with the characteristic platinum X-rays, though the signals in the clover detector were weaker, due to the large Compton background and lower photo-peak efficiency at this energy range. The time-difference spectrum between a recoil implantation of ^{173}Pt and a subsequent γ-ray event in the planar detector was produced for each of the two γ rays, and is shown as an inset to figure 7.3, and does not utilise the 30μs trigger time gate. The planar detector was chosen owing to having much more statistics than its partnering clover detector. A decay curve was fitted to the data using the least-squares method, with a background term included, and is shown as an inset in figure 7.3(a). From the results of the fit for both γ-ray gates, the half-lives of the 104- and 145-keV transitions were measured as 7.03(17)μs and 7.16(27)μs, respectively. The measured half-lives are consistent to each other for both transitions, indicating the possibility of the decays emanating from the same isomer; taking an error weighted mean of the two measured half-lives yields 7.06(14)μs.

Coincident analysis was performed in the focal plane, and can be approached in several different ways. For example, a two-fold $E_{\gamma 1}$-$E_{\gamma 2}$ matrix can be filled for the planar detector, which looks for a sequence of two hits taking place within a short time-frame inside the whole of the detector crystal. Other examples include a $E_{\gamma 1}$-$E_{\gamma 2}$ matrix for two-fold events taking place in the clover detector, or even looking for coincident events taking place in both detectors. In this work, two-fold coincidence analysis in the planar detector and coincidences between the clover and planar detectors were investigated. The former is presented in figures 7.3(b) and 7.3(c), and clearly shows that the 104- and 145-keV γ rays form a cascade. As no other transitions were observed, one can measure the K-shell internal conversion coefficient, $\alpha_{ICC,K}$, and is given by

$$\alpha_{ICC,K} = \frac{I_{K_\alpha} + I_{K_\beta}}{I_\gamma \omega_K}, \tag{7.3}$$

where $I_{K_\alpha} + I_{K_\beta}$, I_γ and ω_K are the intensities of the K-shell X-rays and the γ ray, and the K-shell X-ray fluorescence, respectively, in the gated spectrum. This was performed when gating on the two γ rays in the clover detector, and looking at the projection spectra in the planar detector; this had allowed the peak volumes to be corrected for the efficiency

E_γ (keV)	E_i (keV)	E_f (keV)	$\alpha_{ICC,K_{expt}}$	$\alpha_{ICC,K_{BrIcc}}$	$I_i^\pi \rightarrow I_f^\pi$
103.64(23)	104	0	4.9(3)	4.95(8) *(M1)*	$(9/2^-) \rightarrow (7/2^-)$
145.11(25)	249	104	10.1(10)	10.49(16) *(M2)*	$(13/2^+) \rightarrow (9/2^-)$

Table 7.3: A summary of the two delayed γ rays that were detected in the focal plane spectrometers. The initial (E_i) and final (E_f) energies of the transition, as well as the measured and *BrIcc*'s calculated values of $\alpha_{ICC,K}$ for the corresponding multipolarity are also shown here.

of the planar detector, while this would not have been possible when looking for two-fold γ-γ events exclusively in the planar detector. Using the value of $\omega_K = 0.963(13)$ for Pt [31], $\alpha_{ICC,K}$ was measured and then compared to *BrIcc*'s calculated values [66], and have shown that the 104- and 145-keV transitions are most compatible with *M1* and *M2* multipolarities, respectively. The isomeric transition has been assigned to the 145-keV *M2* transition, thus allowing a reduced transition probability, $B(M2)$, to be determined. The formula was modified to take into account of the branching ratio, b_γ, and the total internal conversion coefficient, α_{ICC}. This procedure was also used by Scholey *et al.* [76], where the $B(M2)$ is given by

$$B(M2) = \frac{b_\gamma 3.10 \times 10^7}{A^{2/3} E_\gamma^5 T_{1/2}(1+\alpha_{ICC})} \text{W.u.}, \tag{7.4}$$

where E_γ is in keV and $T_{1/2}$ is in seconds. Using a branching ratio of 100%, a value of $B(M2) = 0.140(3)$W.u. is compatible with the idea that this transition is of single-particle nature. A summary of these results are displayed in table 7.3.

The energy measurement of the 103.6-keV γ ray in the planar detector was consistent to the energy measurement of the 103.4-keV γ ray inside JUROGAM II when gating on the 495-keV transition. In addition, the lack of the yrast transitions was observed when gating on the 495-keV transition, whereas the yrast spectrum in JUROGAM II was reproduced when gating on the focal plane γ rays. It can be concluded, therefore, that the band comprising of the 495-, 634-, 662-, 530- and 511-keV transitions has been placed directly feeding the $(9/2^-)$ state, presumably of the band-head configuration $\nu h_{9/2}$ for the first time. This consequently allowed the excitation energy of the $\nu i_{13/2}$ band-head to be measured for the

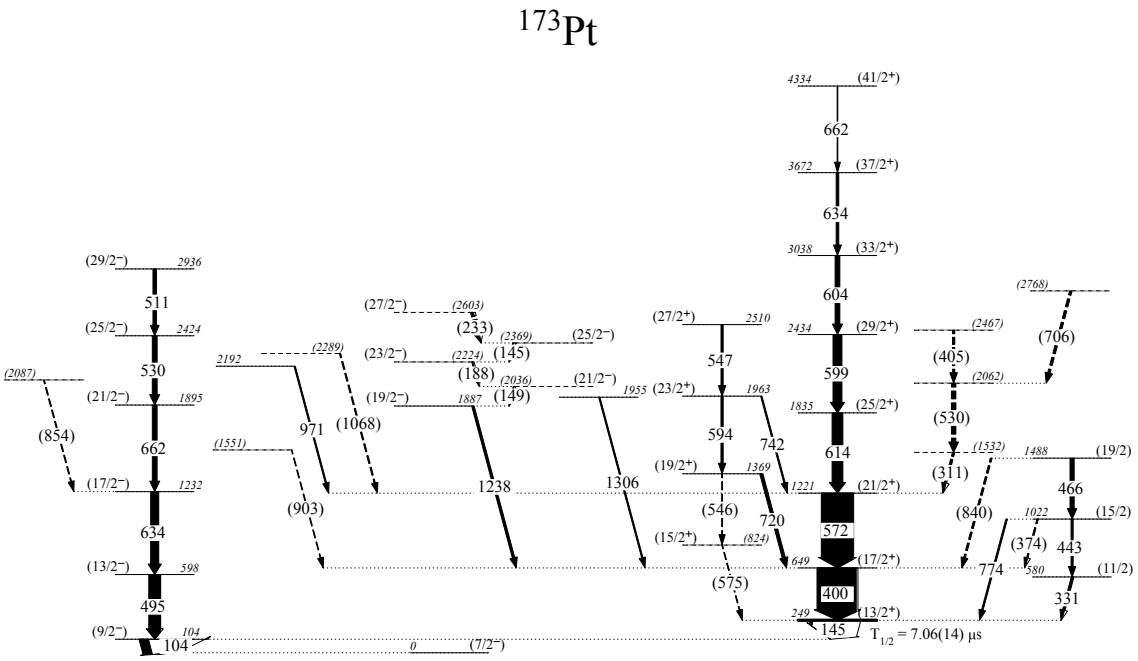

Figure 7.4: Level scheme of ^{173}Pt, showing the yrast band and its unfavoured signature band, a newly discovered negative parity band as well as some more exotic states. The widths of the arrows is proportional to the intensities of the γ rays. Tentative assignments are marked in parentheses. The half-lives of any confirmed isomeric states are also indicated.

first time, and has a value of 248.8(3)keV. This was not known before due to the state being isomeric; γ decays from this state take place long after the recoil has left the target chamber, and requires detailed spectroscopy in the focal plane. The excitation energy of the yrast band has been adjusted to give 4334(1)keV, which now takes the above measured band-head's excitation energy into account.

Together with the in-beam and the focal plane γ spectroscopy of ^{173}Pt, a level scheme was constructed, and is shown in figure 7.4. Tentative and confirmed transitions are both displayed in the diagram, along with their excitation energies of each state. Tentative spin and parity assignments have assumed the ground state configuration of ^{173}Pt to be of $\nu f_{7/2}$ nature.

7.3 Fine Structure in the α Decay of ^{173}Pt

Previous reports [10] have found evidence of fine structure in the α decay of ^{173}Pt, in which several, low-lying states in the daughter nucleus, ^{169}Os, were populated. In this work, the decay spectroscopy of ^{173}Pt was investigated, utilising in the planar germanium detector to improve the sensitivity of this behaviour.

Figure 7.5(a) shows all hits in the planar germanium detector that take place following a correlated recoil-α decay event of ^{173}Pt taking place within 1.5s in the same pixel of the DSSD. A wide energy gate was used to include all known fine-structure transitions in the spectrum. It was found that all of the observed γ rays were prompt ($T_{1/2} < 10$ ns), and so a narrow time gate was imposed in order to suppress background events. This revealed a very weak transition, a 112.3-keV γ ray, which was previously unobserved. Due to the sensitivity of low-energy photons of the planar detector, another transition, a 34.8-keV γ ray, was observed, and was noted for its large intensity. The other two γ rays, the 136.1-keV and the 171.0-keV transitions, confirm previous observations. The 136.1-keV γ ray was observed to be a doublet; the more intense peak corresponds to the fine-structure α decay of ^{173}Ir. No evidence of γ-cascades was observed in the fine-structure analysis of ^{173}Pt.

In order to establish that all of these transitions do emanate from the ground state of ^{173}Pt, a gate was placed on each of the γ rays and a decay spectrum of the DSSD was filled that looked for corresponding α decays coming from ^{173}Pt. The half-lives for each fine-structure transition were also measured using the maximum-likelihood method (with the exception of the 34.8-keV transition, in which there was sufficient statistics to perform a least-squares fit) and were consistent to the half-life of the ground-state to ground-state (G.S.-G.S.) transition. The α-decay Q-value for each fine-structure transition was calculated from the measured decay energy; a list of results for all the observed decay transitions and their corresponding γ ray is shown in table 7.4.

The relative branching ratios for all of the fine-structure transitions were measured. There was a significant challenge in obtaining reliable results due to contamination in the α spectra in the DSSD. The alternative was to measure the intensities of the γ decays

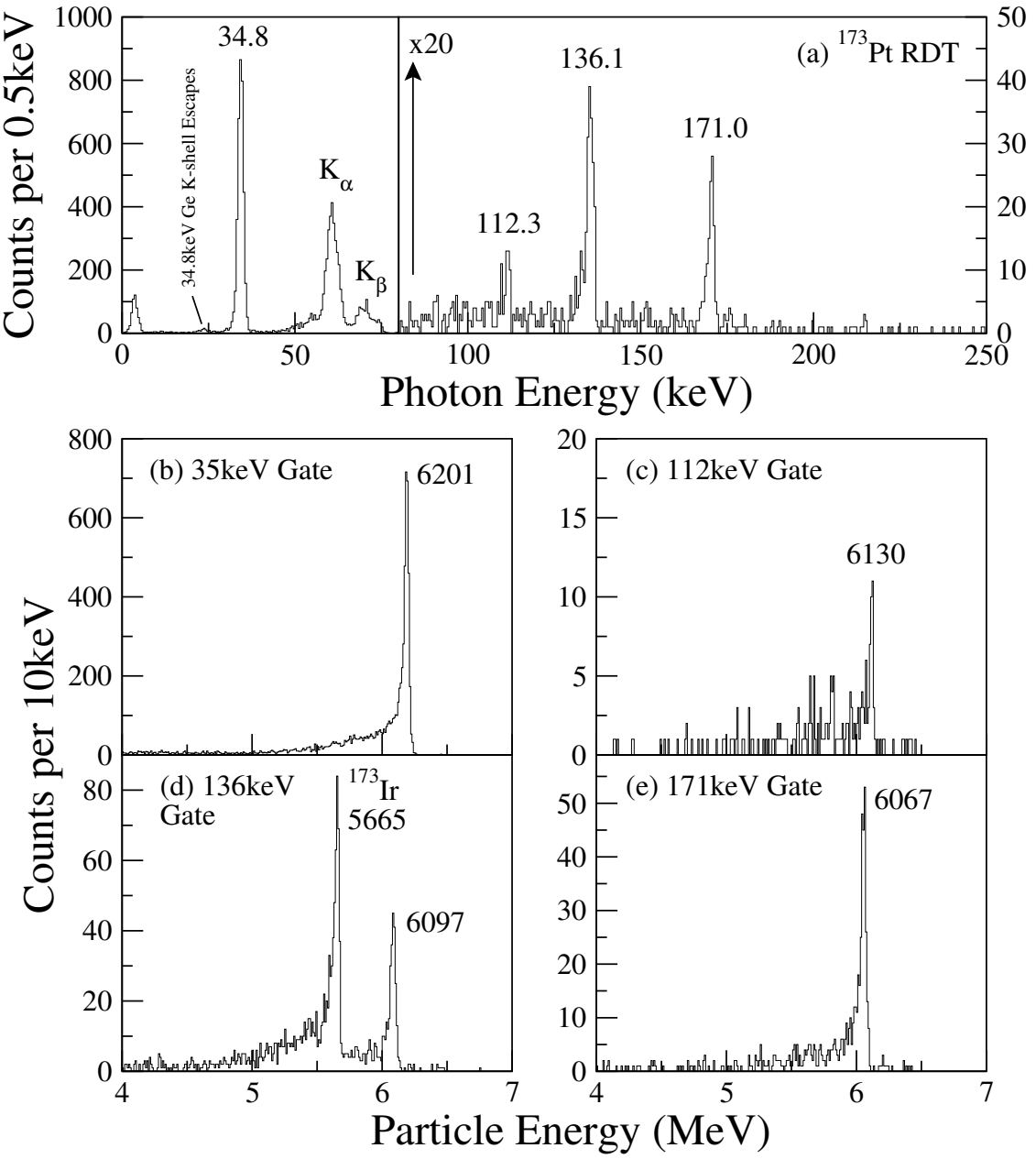

Figure 7.5: (a) All photon events in the planar detector that have been correlated with a recoil-α decay event of ^{173}Pt occurring within 1.5s taking place in the same pixel of the DSSD (using a wide energy gate). A narrow time gate between the α-decay event and the subsequent γ decay was utilised. Correlated α-decay spectra in coincidence with the (b) 35-keV γ ray, (c) the 112-keV γ ray, (d) the 136-keV γ ray, and (e) the 171-keV γ ray in the planar detector.

in the planar detector; however, the internal conversion coefficient is required, and it was not possible to measure this due to the impracticalities of selecting a single transition in the DSSD due to the low resolution of the peaks, as well as low-energy tail contributions

E_α (keV)	Q_α (keV)	$T_{1/2}$ (ms)	$b_{\alpha_{relative}}$ (%)	$b_{\alpha_{absolute}}$ (%)	E_γ (keV)
6235(4)	6383(4)	378(3)	83.6(17)	71.9(36)	0
6201(4)	6348(4)	385(9)	15.2(11)	13.1(11)	34.84(18)
6130(7)	6275(7)	498^{+106}_{-75}	0.15(3)	0.13(3)	112.3(3)
6097(5)	6241(5)	375(35)	0.5(4)	0.4(4)	136.12(19)
6067(5)	6210(5)	354(37)	0.5(4)	0.4(4)	170.97(20)

Table 7.4: A summary of all of the observed fine-structure transitions emanating from the ground state of ^{173}Pt, with the G.S.-G.S. transition also included. The α energy, Q-value, half-life, relative and absolute branching ratio (using $b_\alpha(^{173}\text{Pt}) = 86(4)\%$), and its corresponding γ-ray energy have been listed.

from other decay events. With the exception of the 34.8-keV fine-structure decay, which was measured directly from the α spectrum, the intensities were obtained from deducing a range of internal conversion coefficients, based on the observation of prompt γ emission. By limiting the multipolarities to *E1*, *E2* and *M1*, an *average* conversion coefficient was obtained from *BrIcc* [66], which allowed, albeit imprecise, measurements of the relative branching ratios for these transitions. The 112.3-keV transition, as demonstrated in the following section, was found to be of *M1* nature, thus improving the precision of its relative branching ratio measurement.

Figure 7.6 shows a plot of the various fine-structure α-decay transitions, including the G.S.-G.S. transition, corresponding to the emitted γ ray in coincidence with the decay. Using the Q-value for the G.S.-G.S. α decay as the total Q-value for this decay event, the fine-structure Q-value can be checked by applying the formula

$$Q_{\alpha,G.S.} = Q_{\alpha,F.S.} + E_{\gamma,F.S.} \tag{7.5}$$

for each transition. If the resulting value is consistent with $Q_{\alpha,G.S.}$, then one can confidently establish this decay sequence emanating from the ground state of ^{173}Pt, and the subsequent γ decay will therefore take place in ^{169}Os. The errors of the Q-values here are smaller due to the uncertainty of the calibration error of the DSSD and the planar detector cancels when the energy differences are taken. It was found that summing the Q-value energies for each of the α and γ decays of all of the fine-structure transitions in

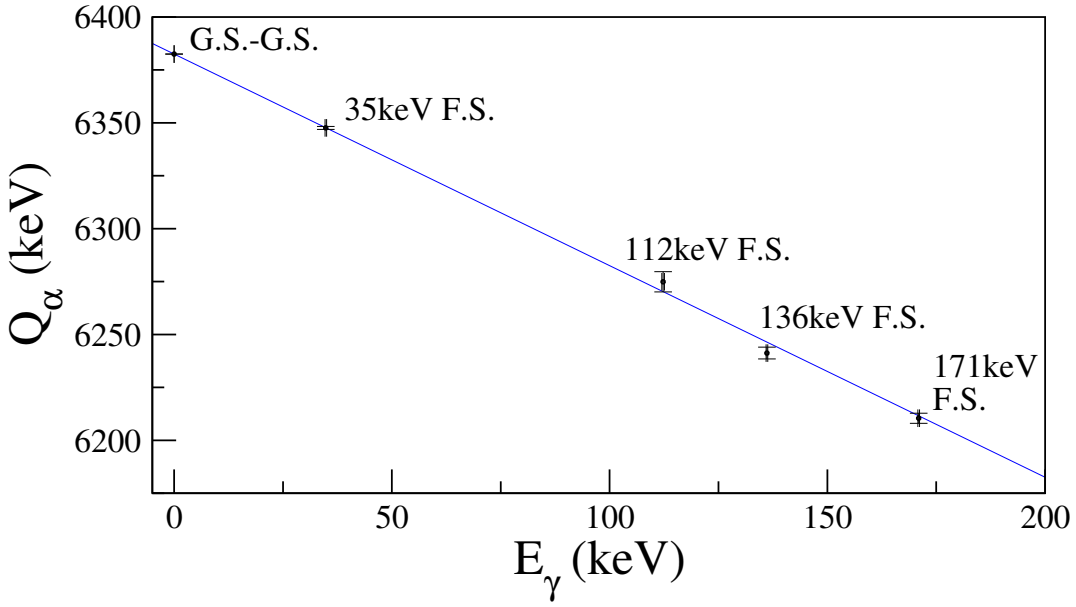

Figure 7.6: The comparison between the α-decay Q-values and their corresponding γ-ray energies for all of the decay transitions taking place from the ground state of ^{173}Pt. The blue line indicates transitions that correspond to the ground-state to ground-state α decay of ^{173}Pt.

^{173}Pt yielded consistent results to that of the G.S.-G.S. α-decay transition.

Figure 7.8 illustrates the five different possible decay paths that were observed to be emanating from ^{173}Pt. Additional data from the in-beam and focal plane spectroscopy of ^{169}Os, described in detail in the next section, has helped constrain some of the properties of a couple of the fine-structure decay paths in the decay scheme.

7.4 ^{169}Os: Yrast and Low-Spin Structure Analysis

A small amount of ^{169}Os recoils were populated in this experiment, via an assumed αp2n evaporation channel, from the compound formation of ^{176}Hg. In-beam and focal plane spectroscopy were performed as if this was considered the "mother" isotope. Consequently, this additional knowledge had complimented the α-decay fine-structure of ^{173}Pt, using the additional information obtained from the ^{169}Os recoils. Due to the low α decay branching ratio of 11(1)% and the relatively long half-life of 3.6(2)s [6], using the RDT technique would reduce too much statistics of an already uncommon reaction channel in this experiment. Clean focal plane spectra with lots of statistics could still be obtained

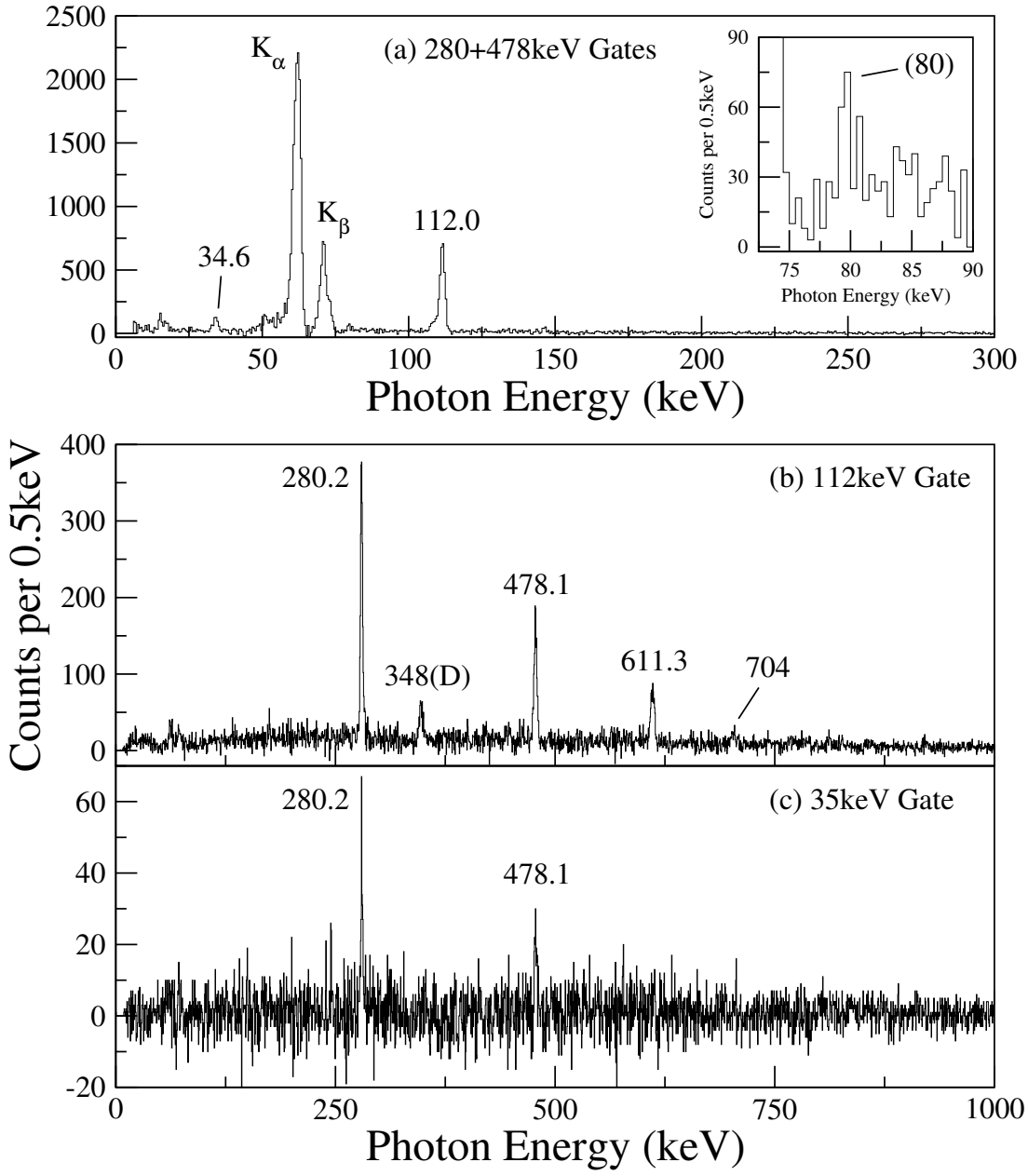

Figure 7.7: (a) Background-subtracted planar germanium spectrum correlated within 50μs of a recoil implantation in the DSSD, as well as the 280- and 471-keV γ gates in JUROGAM II. Panels (b) and (c) show the background-subtracted spectra in JUROGAM II when tagging on the 112.0- and the 34.6-keV transitions, respectively.

by only utilising the RT method, and gating on a corresponding γ ray in JUROGAM II. In reverse, the *recoil-isomer-tagging* technique was used to gate on a delayed γ transition detected in the focal plane in order to bring out the yrast spectrum of ^{169}Os in JUROGAM II.

Figure 7.7(a) shows background subtracted events in the planar germanium detector when tagging on ^{169}Os's 280- and 471-keV γ rays [11] in JUROGAM II. These two γ ray energy peaks had no observable contamination from other activities at similar photon energies detected in JUROGAM II. By applying a background gate on a section of the Compton continuum, a relatively clean spectrum in the focal plane was realised. Transitions of varying intensities were observed in the planar germanium spectrum, which includes the 112.0-, 34.6- and 80-keV transitions. The measured E_γ of the 112.0-keV activity was consistent to that found in the α-decay fine-structure analysis of ^{173}Pt; the same can be said for the 34.6-keV activity. A 80-keV transition was barely visible above the background, and thus observation of this γ ray is currently tentative. A fourth photon-peak of roughly 16keV was also noted; subsequent analysis suggests it was the result of "background" artefacts, as this peak appeared when using different γ gates in JUROGAM II. A time difference spectrum was constructed by gating on the 112-keV transition; a least-squares fitted half-life yielded a value of 17.3(12)μs. Assuming that this transition is the same that was observed in the α-decay fine-structure activity, the 112-keV γ ray is prompt; another γ ray decaying from an isomer must be feeding this state. One could speculate that the 80-keV transition could be isomeric, and is of *M2* nature; it was not possible, however, to find any coincident γ rays with this transition, nor was it possible to determine its half-life, due to the lack of statistics. Assuming that this transition is isomeric, the reduced transition probability for this state has been estimated to be $B(M2) = 0.153(13)$W.u.

The authenticity of the 34.6- and 112.0-keV delayed γ rays were investigated. Figures 7.7(b) and 7.7(c) shows background-subtracted prompt γ-rays in JUROGAM II that were in delayed coincidence with the 112.0- and 34.6-keV γ rays, respectively. The γ rays known to populate the yrast states in ^{169}Os were observed, indicating that these delayed transitions are fed from the $(13/2^+)$ isomer. The measured energies are consistent to the measured γ-ray energies following the α-decay fine structure of ^{173}Pt.

A different technique in obtaining the internal conversion coefficient for the focal plane γ rays was employed, because it was not possible to isolate the γ rays of interest via γ-γ coincidence analysis. The total intensity of the band-head feeding γ ray, corrected for

internal conversion, was compared to the total γ-ray intensity of the delayed γ transition. The total internal conversion coefficient can then be calculated by the following relation

$$\alpha_{ICC} = \frac{I_{\gamma+\alpha_{ICC}}(\text{Yrast})}{I_{\gamma}(\text{Delayed})} - 1, \tag{7.6}$$

where $I_{\gamma+\alpha_{ICC}}$(Yrast) is the total intensity for the band-head feeding Yrast transition, and I_{γ}(Delayed) is the γ intensity of the delayed γ ray of interest.

This method assumes that:

- The transmission efficiency of RITU has been accounted for.
- Missing intensity due to Compton scattering is negligible.
- *BrIcc*'s calculated value of α_{ICC} is assumed for a pure *E2* transition for the band-head feeding γ ray.
- Missing intensity in the focal plane due to isomeric decays in-flight, as well as due to the time-gate cut off, has been accounted for.
- The band-head feeding transition is the only decay that feeds this state, and has fully decayed before the recoil leaves the target chamber.

The total intensity of the 400-keV $(17/2^+) \rightarrow (13/2^+)$ transition in ^{173}Pt, in addition to the intensities of the side-feeding transitions that also feed the $(13/2^+)$ state, was compared to the intensity of the focal plane 104- and 145-keV γ rays. The measured value of α_{ICC} for the 145-keV transition was 13.5(14), which is consistent to *BrIcc*'s calculated value of 14.69(23) for an *M2* transition [66]. The 104-keV transition had a measured α_{ICC} $6.3^{+1.5}_{-1.1}$, also consistent to *BrIcc*'s calculated value of 6.02(10) for an *M1* transition [66].

This approach was now applied to the 112.0-keV focal plane γ ray, and when the intensities were compared to the 280-keV $(17/2^+) \rightarrow (13/2^+)$ transition, yielded a measured α_{ICC} of $4.3^{+1.0}_{-0.8}$ for the 112.0-keV transition. This value is consistent with *BrIcc*'s calculated value of 4.07(6) for an *M1* transition [66]. The measurement of the 35-keV transition yielded a value of poor significance due to low statistics and large intensity differences between the front and back strips of the planar detector. The 80-keV transition was too

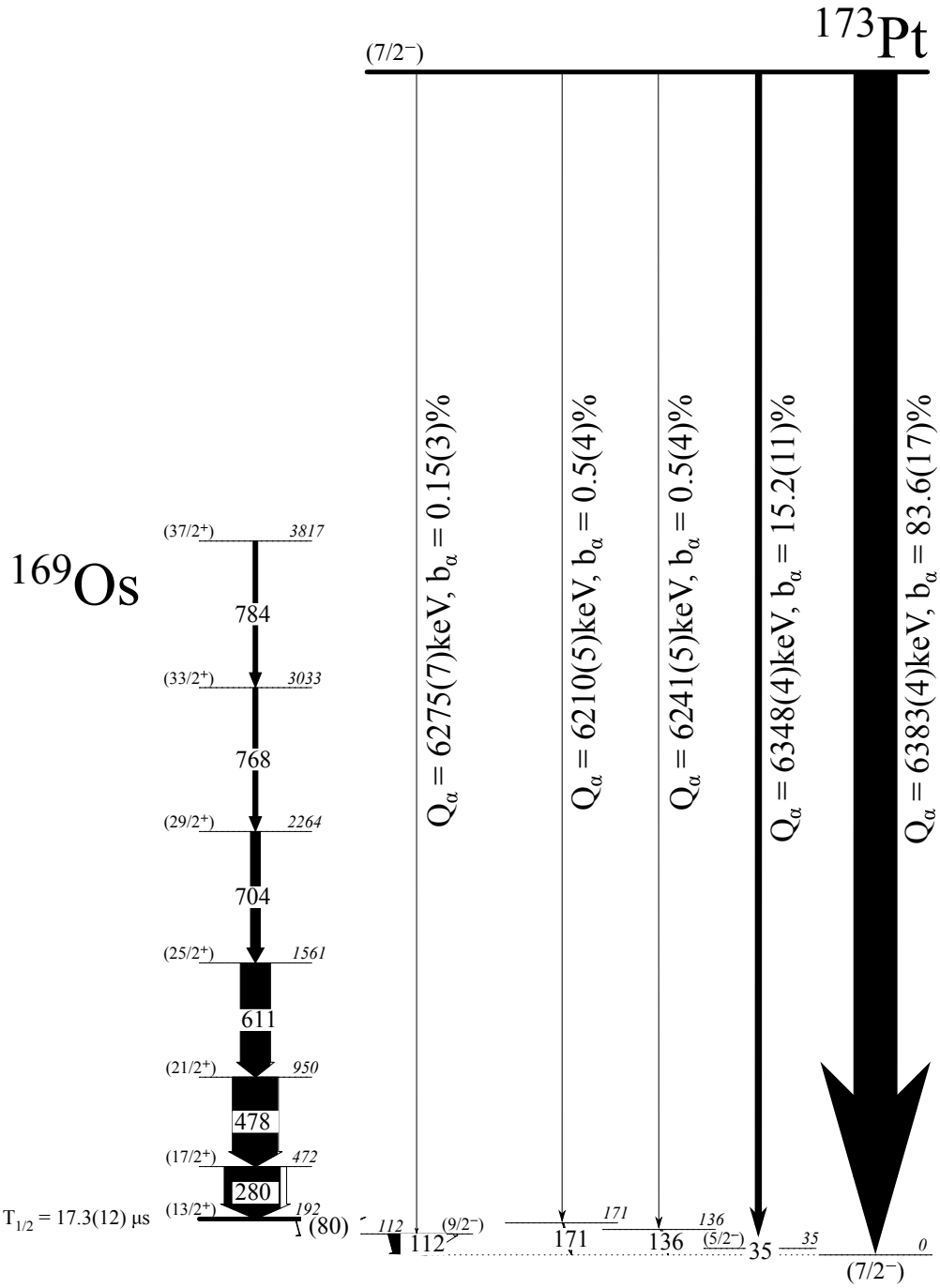

Figure 7.8: The decay scheme of ^{173}Pt, showing all of the fine-structure transitions that have been observed, along with the yrast decay path taking place in ^{169}Os.

weak to obtain a measurement of α_{ICC}. That said, the spin and parities of the yrast decay path have been tentatively established, and is presented in ^{173}Pt's decay scheme in figure 7.8.

Chapter 8

Discussion

8.1 The Decay Chains from ^{177}Tl

Prior to the undertaking of this work, the known α decay of ^{161}Ta was assumed to be the result of the decay of the ground state [7]. However, from the results presented above it is apparent that the 5142(6)keV α decay is in fact the decay of the high-spin isomeric state in ^{161}Ta. The deduced Q_α value of 5273(6)keV is plotted in figure 8.2(a) and can be seen to continue the near-linear trend of the decreasing Q_α values with increasing neutron number. The Q_α-value for the previously unreported decay of the ground state of ^{165}Re is plotted in figure 8.2(b). This value appears to fit very well with the linear trend already established by the neighbouring Re isotopes.

The α-decay activities of ^{165}Re^g and ^{161}Ta^m were successfully correlated with parent nuclides that decay from the ground and isomeric states, respectively. Combining this evidence, along with the decay data from other nuclides that take part in the same α-decay sequence, a decay chain spanning seven generations was established, and is shown in figure 8.1. The decay chain also includes the sequence following the proton emission of ^{177}Tl, which was observed for both high- and low-spin states [5]. As a result of the observation of the α decay of ^{165}Re^g in this work, the excitation energy of the high-spin state in ^{161}Ta can be determined; the formula that calculates this excitation energy is

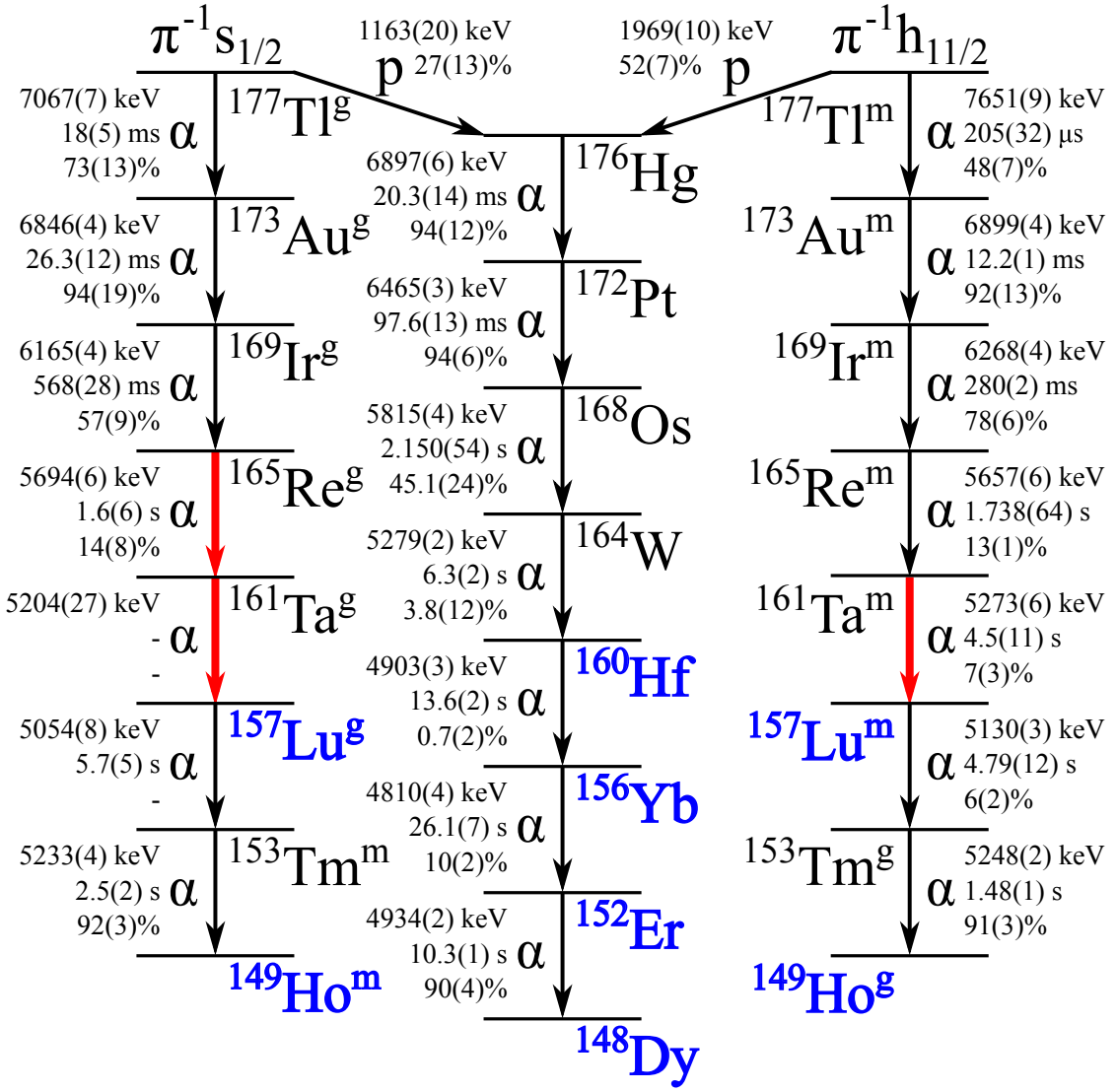

Figure 8.1: A schematic decay scheme that originates from the $\pi^{-1}(h_{11/2})$ and the $\pi^{-1}(s_{1/2})$ states of ^{177}Tl. The nuclides written in blue bold font have had their masses measured directly [77, 78]. The decay Q-values, half-lives and branching ratios are indicated. The decays that have been observed for the first time, or have had their decay path reassigned are shown as thick red arrows. Data not measured in this work were obtained from references [5, 79, 6, 80, 81, 51, 68, 59, 82, 83, 84, 85, 86, 87].

given by

$$\Delta E\left(^{161}\mathrm{Ta}\right) = \Delta E\left(^{165}\mathrm{Re}\right) + Q_\alpha\left(^{165}\mathrm{Re}^g\right) - Q_\alpha\left(^{165}\mathrm{Re}^m\right). \tag{8.1}$$

Using the α-decay energies reported here and the excitation energy of the α-decaying isomeric state in ^{173}Au, 214(23)keV as reported by Poli *et al.* [5], it has been determined that the high-spin state in ^{161}Ta has an excitation energy of 95(26)keV. Taking this analysis

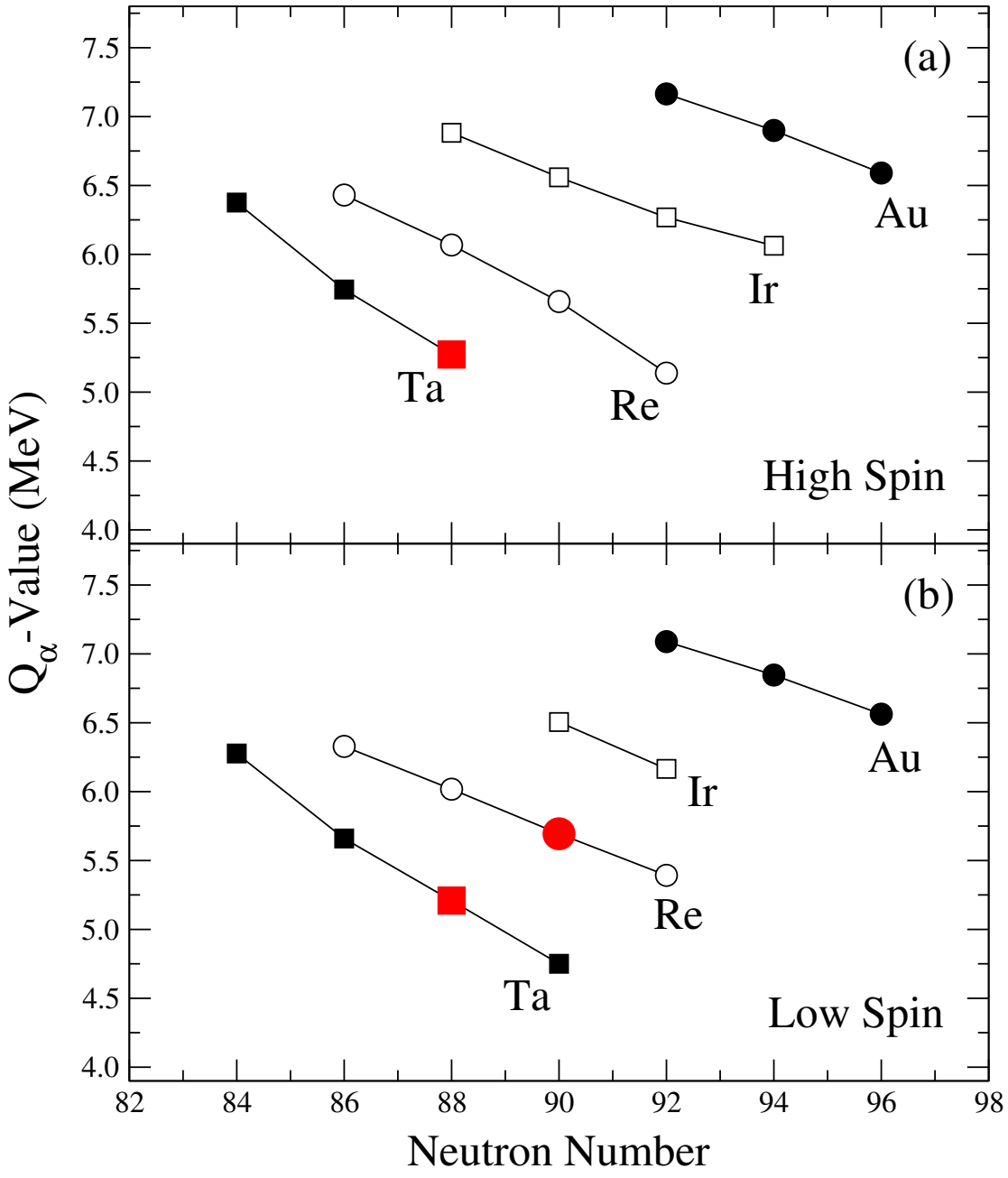

Figure 8.2: Experimental decay Q-values of odd-Z, even-N nuclei located in the region of interest. Panel (a) shows the Q_α values for decays emanating from the high-spin states (based on the $\pi^{-1}(h_{11/2})$ orbital), whereas panel (b) shows the Q_α values for decays emanating from the low-spin ($\pi^{-1}(s_{1/2})$) states. The symbols that represent the Q_α values determined from this work are shown in red and are enlarged. Data not measured in this work are taken from references [7, 51, 68, 82, 88, 89, 90, 91, 92, 93, 94, 85].

one step further, the knowledge of the energy difference of the two α-decaying states in ^{157}Lu, 26(7)keV [7], allows the Q_α-value of the unobserved decay of the ground state of

^{161}Ta to be determined: $Q_\alpha\left(^{161}\mathrm{Ta}^g\right) = 5204(27)$keV. This new value is plotted in figure 8.2(b) where once more it fits well with the trend established by the neighbouring Ta isotopes.

In reference [95] an extensive level scheme of excited states in ^{161}Ta built upon a proposed $J\pi = (11/2^-)$ state was reported. However, in that work it was not possible to establish whether this level or a $(9/2^-)$ level was the lowest-lying $\pi^{-1}(h_{11/2})$ state. The separation energy of the $J\pi = (9/2^-)$ and the $(11/2^-)$ states in the neutron-deficient Ta isotopes is observed to decrease from 99keV in ^{167}Ta [96], 71keV in ^{165}Ta [97] to 45keV in ^{163}Ta [98]. Extrapolating to ^{161}Ta suggests the separation could be as low as ∼20keV in this nuclide. This would be accommodated within the 40keV uncertainty on the deduced mass excess for the high-spin state in ^{149}Ho meaning that the question regarding the spin and parity of the $\pi^{-1}(h_{11/2})$ based state in ^{161}Ta cannot be resolved by the present study. In addition, no evidence was observed in the focal plane germanium spectrometers that suggested subsequent γ decays following the α decay of $^{165}\mathrm{Re}^m$, $^{169}\mathrm{Ir}^m$ or $^{173}\mathrm{Au}^m$. It therefore remains unclear whether the α-decaying isomer in ^{161}Ta has $J\pi = (9/2^-)$ or $(11/2^-)$.

In combining these new measurements with the information already available on ^{157}Lu it has also been possible to deduce the Q_α-value for the decay of the ground state of ^{161}Ta. As a result of the present work Q_p-values of $-129(24)$keV and $-37(21)$keV have been determined for the ground and isomeric states of ^{161}Ta, respectively, indicating that these states are only just bound with respect to proton emission.

8.2 Atomic Mass Measurements

Proton and α-decay Q-value measurements provide important information on the nuclear mass far from the valley of β stability. Conventional methods, such as Schottky mass spectrometry or Penning trap mass spectrometry are impractical to utilise, due to the low production cross sections and short life times of these nuclei of interest. However, *indirect* methods are possible, and require a correlation of radioactive decays of known Q-values to reach a nucleus that has had its mass measured directly. This would allow the mass

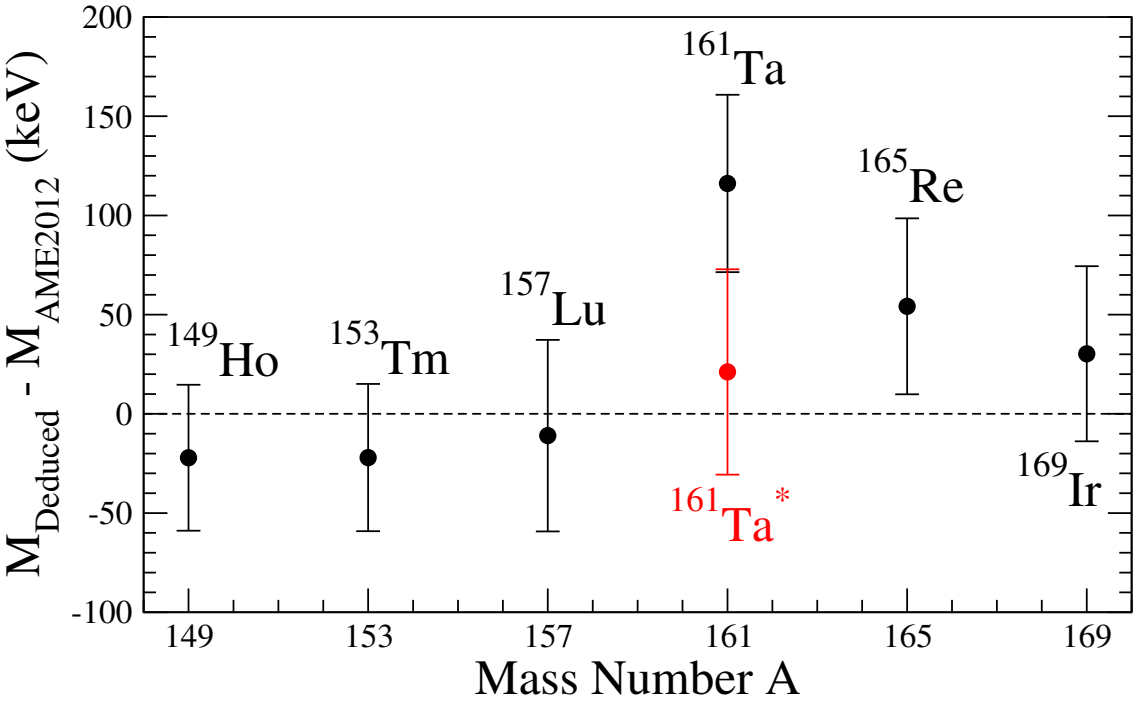

Figure 8.3: The mass excess differences between the values deduced in this work and the values reported in the most recent Atomic Mass Evaluation literature [99, 100]. The dashed line indicates zero difference. The red data point corresponds to the mass of ^{161}Ta once corrected for the excitation energy of the $h_{11/2}$ isomer, as was previously assumed.

excesses of nuclei, which can potentially be located beyond the proton drip line, to be determined with little ambiguity.

In combining this new measurement with the α-decay Q-values of Figure 8.1 and the mass excess of ^{156}Yb reported by Litvinov *et al.* ($-53283(28)$keV [78]), it is possible to determine the mass excess for the ground state of ^{161}Ta: $-38816(40)$keV. Using the measured mass excess for ^{156}Yb and the α-decay Q values of figure 8.1, the mass excesses of the ground and isomeric states in ^{149}Ho can be deduced. The deduced mass excess of the high-spin state in ^{149}Ho is $-61648(40)$keV which agrees remarkably well with the directly measured value of Litvinov *et al.* [78] of $-61646(31)$keV. The mass excess deduced for the low-spin state of ^{149}Ho was found to be $-61582(58)$keV which is in line with expectations based on the previously known 49keV excitation energy of the $\pi^{-1}(s_{1/2})$-based isomer in ^{149}Ho [81].

The mass excesses deduced in the present work are compared with the values reported in the most recent Atomic Mass Evaluation (AME2012) [99, 100] in figure 8.3. Overall,

		This Work		Literature
Nucleus	$\Delta\ell$ ($\hbar$)	δ^2 (keV)	HF	δ^2 (keV)
^{169}Ir^m	0	70(10)	1.00(15)	72(11) [5]
^{169}Ir^g	0	64(13)	0.91(19)	45(25) [5]
^{165}Re^m	0	81(8)	1.15(12)	
^{165}Re^g	0	66(45)	0.93(64)	
^{161}Ta^m	0	113(56)	1.60(80)	

Table 8.1: The reduced widths, δ^2, and the hindrance factors, HF, of the α-decay activities of nuclei measured in this work. The hindrance factors were measured relative to the ground-state to ground-state α decay of ^{212}Po. The changes in angular momentum, $\Delta\ell$, were also presented, and assumed to have no changes to the nuclear spin through the decay chain.

there is very good agreement between the values obtained in this study and those in the evaluation with the deduced mass of ^{161}Ta being the notable exception. This discrepancy is possibly the result of the inclusion of the incorrectly assigned α-decay of ^{161}Ta. Indeed, if the 95(26)keV energy difference between the $(11/2^-)$ and $(1/2^+)$ states of ^{161}Ta is taken into account then the difference between the mass reported here and the AME2012 value is similar to those found for the other five nuclides plotted in figure 8.3.

The consistency in the mass measurements indicated by the agreement between the deduced masses of the ground and isomeric states of ^{149}Ho and the masses measured in reference [78] suggests that all of the α decays proceed between ground states with no electromagnetic decays occurring at any points in the decay chain between ^{177}Tl and ^{149}Ho. This is indicative that the single-particle configurations, established as $\pi^{-1}(h_{11/2})$ and $\pi^{-1}(s_{1/2})$ in the heavier members of the decay chain, are also consistent down the entire decay chain. This conclusion is supported by the reduced width measurements, calculated using the Rasmussen formalism [101] and assuming s-wave emission, which are listed in table 8.1. The reduced widths measured in the present work have been compared to the value corresponding to the α decay of the ground state of ^{212}Po. These hindrance factors, also listed in 8.1, are consistent with unhindered α decays.

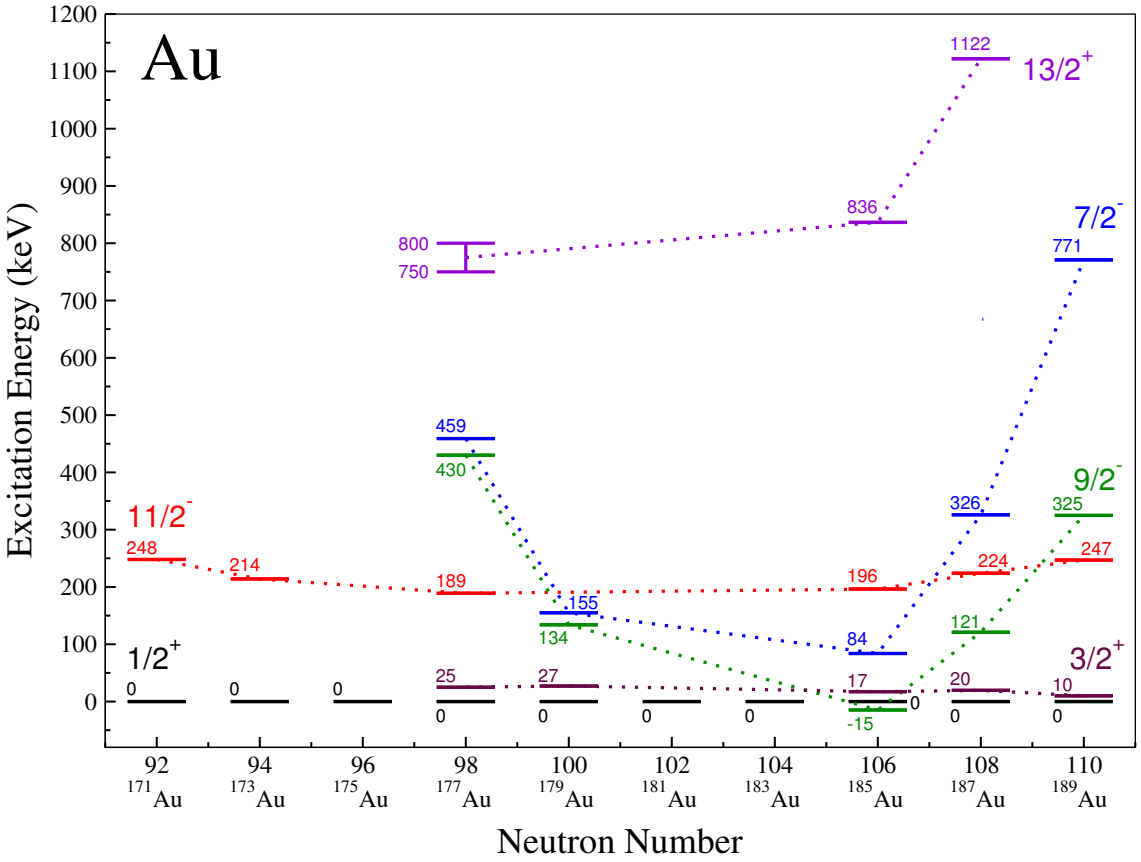

Figure 8.4: The excitation energies of the various configurations found in various isotopes of Au, relative to the $\pi^{-1}(s_{1/2})$ state. Each state has been associated by its colour in this figure. The data was taken from references [67, 102, 103, 104, 105, 106, 107].

8.3 Single-Particle Behaviour of the Light Au Isotopes

Figure 8.4 presents the excitation energies, relative to the $\pi^{-1}(s_{1/2})$ state, of the intruder quasiparticle configurations as a function of neutron number. It is noted that, particularly for the "mid-shell" region of mass numbers 181–185, the ground state configurations are of deformed nature. It is also this region where *shape coexistence* takes place, and has been reported for several odd-N isotopes of Au [108, 103, 109]. Outside of this region, these configurations become energetically unfavourable, and so nuclei exhibit near-spherical, single particle excitations, as it is apparent in ^{173}Au and ^{195}Au, which remarkably resembles its lighter partner [63].

As the $(9/2^-)$ and $(7/2^-)$ band-head states are only known down to ^{177}Au, extrapolation methods were used in order to determine their excitation energy in the region of

Configuration	E_x Relative to $(11/2^-)$ (keV)	E_x Relative to $(1/2^+)$ (keV)
$(7/2^-)$	1323(56)	1537(51)
$(9/2^-)$	995(78)	1209(74)
$(13/2^+)$	1411(133)	1625(135)

Table 8.2: Extrapolated excitation energy values for the three intruder states of ^{173}Au, using the documented excitation energy of 214(23)keV for the $h_{11/2}$ state in ^{173}Au [5].

^{173}Au. The same approach was used also for the $i_{13/2}$ band, which was observed in ^{175}Au and has an excitation energy of 976.7keV relative to the $(11/2^-)$ state [4], as well as in the heavier isotopes [106, 104, 105]. A quadratic fit function was used to the data for each configuration, ensuring that the excitation energies are relative to a common state. For example, the excitation energy values used for the $(7/2^-)$ and the $(9/2^-)$ band heads were relative to the $(1/2^+)$ state, which is not known in ^{181}Au and ^{183}Au, and has an excitation energy of 23.6keV [106] relative to the $(5/2^-)$ ground state. The values of the $(13/2^+)$ band-head excitation energies were used relative to the $(11/2^-)$ state, if known. The calculated results are presented in table 8.2. The main feature is the excitation energies in excess of 1MeV for all of the intruder states relative to the ground state of ^{173}Au. While the excitation energies are all consistent to the documented 1176-keV γ ray found feeding the $(h_{11/2})$ isomer in ^{173}Au, due to the lack of statistics for this transition when utilising γ-γ coincidence analysis, it was not possible to associate the excitation of the 1176-keV transition to one of these configurations; more statistics would also be required in order to measure its multipolarity unambiguously.

The α decay of both states in ^{177}Tl, are reported to be unhindered [5]. In addition, the observation of proton emission have assigned configurations of $\pi^{-1}(s_{1/2})$ and $\pi^{-1}(h_{11/2})$ for the low- and high-spins, respectively. This therefore suggests a pure $\pi^{-1}(s_{1/2})$ configuration for the low-spin state of ^{173}Au. The reported excitation energies found in this work show remarkable similarity to the excitation energies of ^{189}Au [67]. The lack of observation of the $\pi^{-1}(d_{3/2})$ orbital in ^{173}Au implies it may have a larger excitation energy, although the lack of statistics in this analysis has prevented its determination. It was also not possible to extrapolate the excitation energy of this orbital due to influences of strong

mixing with the $s_{1/2}$ state in heavier isotopes of Au [103, 104, 105, 110]. As was mentioned previously, the assignments to the spins and parities of these states are assumed based on these systematics.

8.4 Rotational Behaviour in ^{173}Pt

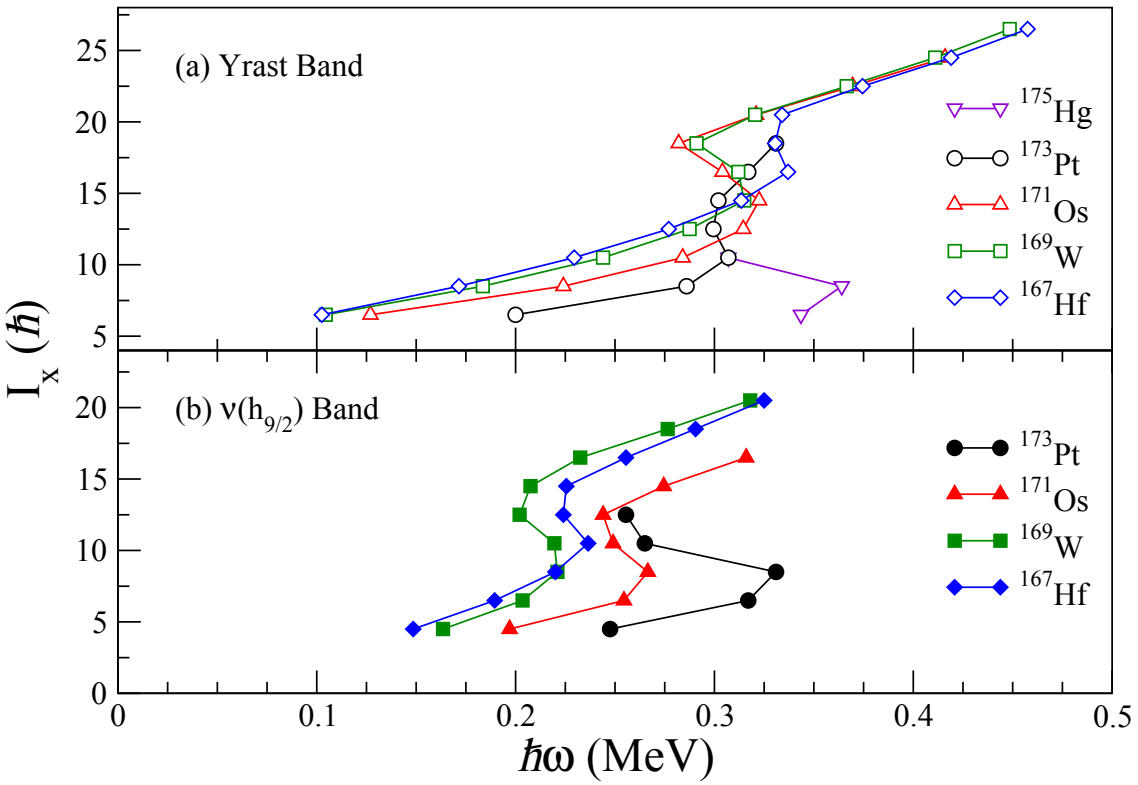

Figure 8.5: The plotted total aligned angular momentum, I_x, as a function of the rotational frequency, $\hbar\omega$, for the (a) yrast bands and the (b) $\nu(h_{9/2})$ bands of the even-Z $N = 95$ isotones. Panel (a) shows data from ^{175}Hg [111], ^{173}Pt (this work), ^{171}Os [112], ^{169}W [113] and ^{167}Hf [114]. Panel (b) excludes the nucleus ^{175}Hg as no evidence of the $\nu(h_{9/2})$ band has been found as of this time of writing.

The behaviour of the lone neutron in the $\nu(i_{13/2})$ intruder band in ^{173}Pt has already been interpreted [9] to exhibit weak coupling to the core due to the near degeneracy of the transitions in the yrast band. Unlike its heavier isotopes, where the large splitting of energy levels between the odd- and even-N isotopes of Pt give rise to strong neutron-core coupling, the neutron behaves as a 'spectator' in ^{173}Pt, and therefore has little influence on the yrast states. Figure 8.5(a) shows the plot of the aligned angular momentum of the

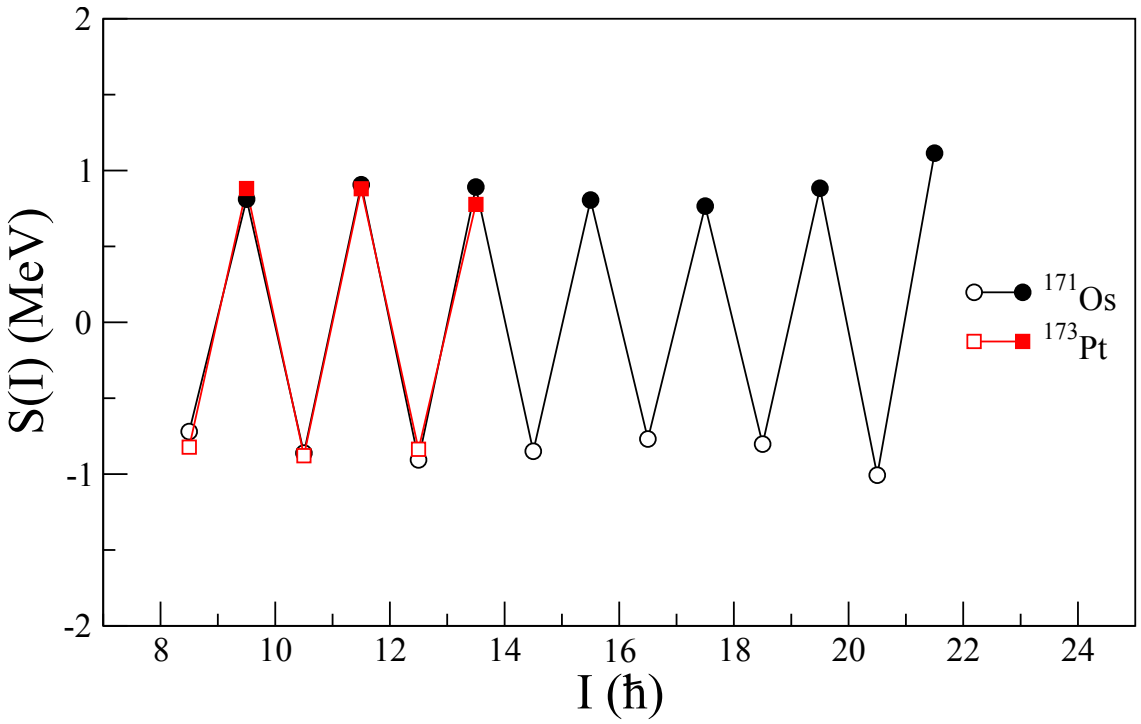

Figure 8.6: The plotted staggering parameter, $S(I)$, as a function of spin, I, for the $\nu(i_{13/2})$ bands in the isotones ^{173}Pt, which was measured from this work, and ^{171}Os, which data was obtained from reference [112]. The filled and open symbols correspond to the $\alpha_{\pm} = -1/2$ and $\alpha_{\pm} = +1/2$ signature bands, respectively.

yrast bands for the even-Z, $N = 95$ isotones, and shows a notable change from isotones (^{171}Os, ^{169}W and ^{167}Hf) where the neutron is strongly coupled to the core, up to ^{173}Pt and ^{175}Hg where decoupling takes place. Due to the odd valence neutron, the first $\nu(i_{13/2})^2$ neutron alignment becomes 'blocked'. The observed backbending in these isotones was suggested to arise from the second $\nu(i_{13/2})^2$ neutron alignment.

The plotted $\nu(h_{9/2})$ bands in figure 8.5(b), show a trend of increasing rotational frequency of the first band alignment as one removes protons from the nucleus. This is due to fewer valence neutrons available, which in turn reduces the deformation of the nucleus, thus requiring more energy to align a pair of neutrons. For the low-Z isotones, this band aligns with the first $\nu(i_{13/2})$ neutron, which was 'blocked' for the $\nu(i_{13/2})$ band. The increasing rotational frequency as Z increases could indicate a change in the mixing to another neutron orbital, and was assumed to be $\nu(f_{7/2})$.

Evidence of the unfavoured signature partner ($\alpha_{\pm} = -1/2$) of the $\nu(i_{13/2})$ intruder

band has been observed in this work. The lowest spin and parity found in this band, the $(15/2^+)$ state, feeds the favoured $(13/2^+)$ band-head via a tentative 575-keV γ ray; the $(19/2^+)$ feeds the $(17/2^+)$ state via a 720-keV γ ray, and the $(23/2^+)$ feeds the $(21/2^+)$ state via a 742-keV γ ray. In-band transitions were also observed up to a spin of $(27/2^+)$ and an excitation energy of 2510keV. The band has been observed, therefore, to exhibit strong splitting. This is expressed in terms of the *staggering parameter*, $S(I)$ [115], which is defined as

$$S(I) = E(I) - E(I-1) - \frac{1}{2}\left[E(I+1) - E(I) + E(I-1) - E(I-2)\right], \qquad (8.2)$$

where $E(I)$ is the excitation energy of the state with spin I. The measured values of $S(I)$ for ^{173}Pt are plotted, along with measurements made from the neighbouring even-Z, $N = 95$, isotone, ^{171}Os [112], in figure 8.6. The results show a remarkable agreement, favouring the $\alpha_{\pm} = +1/2$ signature partner of the $\nu(i_{13/2})$ band.

8.5 Low-spin Structure of ^{169}Os

Calculations performed by Möller *et al.* [12] suggested a ground state configuration of ^{169}Os to be $(5/2^-)$, and it was assumed when analysing its subsequent α decay to ^{165}W [13]. In this work, with the ground state configuration for ^{173}Pt established to be $(7/2^-)$, the possibility of hindered α decays was investigated. Following from the measurement of the relative branching ratios made in Fine Structure in the α Decay of ^{173}Pt (chapter 7, section 3), the reduced width for each α-decay transition was calculated, using the same procedure as was used for the decay chain of ^{173}Au. Table 8.3 shows both the reduced width and the hindrance factors, relative to the ground-state to ground-state α decay of ^{212}Po, for the five confirmed decay paths from ^{173}Pt.

Goon *et al.* [10] had previously measured the reduced α-decay widths and their hindrance factors for the 171-, 136- and 112-keV fine structure transitions (although in Goon's work, no corresponding γ ray was found with the 112keV fine structure transition). As the 35-keV fine structure transition was not observed, the relative branching ratio for the

		This Work		Literature	
Decay Transition	$\Delta\ell$ ($\hbar$)	δ^2 (keV)	HF	δ^2 (keV)	HF
G.S.-G.S.	0	41.8(26)	1.68(10)	47(2)	2.3(2)
35-keV F.S.	1	12.5(11)	5.6(5)	*	*
112-keV F.S.	1	0.24(6)	298(71)	2.9(4)	37(7)
136-keV F.S.	(2)	1.6(13)	45(39)	1.9(4)	56(18)
171-keV F.S.	(2)	2.1(19)	33(30)	2.4(3)	45(12)

Table 8.3: The reduced widths, δ^2, and the hindrance factors, HF, for the five reported α-decay transitions that decay from the ground state of ^{173}Pt in this work. The hindrance factors were measured relative to the ground-state to ground-state α decay of ^{212}Po. The results were compared to previous literature [10]. The changes in angular momentum, $\Delta\ell$, were also presented for each transition; bracketed values indicate tentative assignments. * The 35-keV transition was previously unreported, and so the reduced width and hindrance factor was based from the combined relative branching ratios of the ground-state and 35-keV transitions.

ground-state to ground-state transition was measured to be much larger than in this work; the small energy separation between the 35-keV and ground-state transitions has made resolving the two α peaks difficult. It has been assumed that the 35-keV transition is of *M1* nature, decaying from the $(5/2^-)$ state in ^{169}Os, although it was not possible in this work to verify this hypothesis.

The results from this work is in support with the previously reported values, although the 112-keV transition was found to be more hindered than previously thought. In this work, it was found that the 112-keV transition was consistent to an *M1* multipolarity, decaying from the $(9/2^-)$ state to the $(7/2^-)$ ground state of ^{169}Os. Consequently, fine structure transitions of ^{169}Os may in fact originate from this $(7/2^-)$ state, and not the previously assumed $(5/2^-)$ state. This transition would only give a small contribution to the centrifugal barrier as $\Delta\ell = 1$. Shape change could be the main contributor that gives rise to its large decay hindrance although it was not possible to determine these characteristics.

It was also not possible, in this work, to determine the multipolarity of the 136- and 171-keV γ-ray transitions following the α decay of ^{173}Pt. The uncertainty of the measured hindrance factors have had their internal conversion coefficient ranges taken into account, as these transitions could be either of *E1*, *M1*, or *E2* character. No evidence was found

that these transitions proceed the cascade decays in the yrast band in ^{169}Os, indicating the possibility of other, exotic nuclear configurations that are non-yrast in ^{169}Os, in which can be populated via α decay.

Chapter 9

Conclusions

The neutron deficient nucleus ^{173}Pt and its proton-unbound isobar ^{173}Au have been investigated in an experiment performed at the JYFL Accelerator Laboratory in Jyväskylä. They were produced in fusion-evaporation reactions, separated in flight using a gas-filled separator RITU, and then implanted into the DSSD, located in GREAT, which was used to study their subsequent α decays. Prompt γ radiation is captured by utilising JUROGAM II; an array of Compton-suppressed hyper-pure germanium (HP-Ge) detectors that surrounds the target position, covering as much of the 4π solid angle as possible. Using the well established recoil-decay tagging technique, prompt γ transitions for a particular nucleus can be selected by tagging on its subsequent α decay that was measured in the DSSD, located at the recoil separators focal plane.

Excited states with γ rays feeding the low-spin ground state state of ^{173}Au were discovered for the first time by utilising the recoil-decay tagging method of the α decay of ^{173}Au^{g}, with the additional background subtraction of the high-spin isomer α-decay of ^{173}Au^{m} that was contaminating the spectrum. A level scheme was constructed and is very similar to the low-spin structure of heavier isotopes of Au. The level scheme feeding the high-spin isomer was also expanded, with some features exhibiting remarkable similarity to its heavier even-N isotope, ^{195}Au; tentative spin and parity assignments were based on the systematics of the heavier Au isotopes. No evidence of collective behaviour was observed; estimates of the excitation energies of the intruder $(7/2^{-})$, $(9/2^{-})$ and $(13/2^{+})$

bands vary from 1000–1500keV relative to the ground state. Only one γ ray was observed within this energy range. However, its characteristics were not very well established due to the lack of statistics. There was also no evidence of excitations to the $d_{3/2}$ orbital from the $s_{1/2}$ state; the possibility of this due to low statistics, coupled with large internal conversions could not have been eliminated.

The α-decay chains originating from the ground $s_{1/2}$ and isomeric $h_{11/2}$ states in ^{173}Au have also been investigated. The α decay of the $s_{1/2}$ state in ^{165}Re has been identified for the first time and was successfully correlated with the α decays of the $s_{1/2}$ states in ^{169}Ir and ^{173}Au, with an additional γ gate in JUROGAM II on γs feeding this low-spin state of ^{173}Au. The previously reported α decay of ^{161}Ta has been shown to emanate from the high-spin $h_{11/2}$ state. No evidence of any delayed or isomeric γ transitions were found in both α decay chains. Consequently, the excitation energy of the $h_{11/2}$ state and the α-decay Q-value was able to be determined for the first time, and found the values of 95(26)keV and 5204(27)keV, respectively.

The mass excesses of certain nuclei in the decay chain were also measured. Starting from the directly measured value of Δm = -53283(28) keV by Litvinov *et al.* [78], the decay chain was followed to the high- and low-spin states of ^{149}Ho, where the indirect mass excesses were measured to be -61648(40) keV and -61582(58) keV, respectively. The high-spin state measurement was found to be consistent to the directly measured value of -61646(31) keV, and the low-spin state measurement was consistent to the previously reported excitation energy of 49 keV to the $s_{1/2}$ isomer. The indirectly measured mass excesses for the ground states of ^{153}Tm, ^{157}Hf, ^{161}Ta, ^{165}Re and ^{169}Ir in this work were compared to values reported in the latest Atomic Mass Evaluation table [99, 100]. After correcting for the state from which the previously reported α decay of ^{161}Ta is now associated with, the results are in agreement to the literature values. The possibility of fine structure taking place within the decay chain could not have been eliminated however; in particular, low-energy transitions that are highly converted, become masked by the finite sensitivity of the planar detector, and by the energy resolution of the DSSD, makes observing these processes very difficult.

Previous in-beam spectroscopy on ^{173}Pt revealed the $i_{13/2}$ yrast band and a second band that was assumed to be the unfavoured signature band, although the authors of that work [9] were unable to determine its decay path. The $i_{13/2}$ band head was found to be isomeric, with a half-life measured to be 7.06(14) μs, giving a reduced transition probability of $B(M2) = 2.20(4)$ W.u., and is compatible to a single particle transition. Internal conversion coefficients (ICC) were able to be measured for the first time and found that the 145-keV isomeric transition is of *M2* nature, and its following prompt 104-keV γ ray is of *M1* nature. A linking transition for the unplaced non-yrast band has been found to feed the ground state of ^{173}Pt directly, which has been established, for the first time, to have a spin and parity of $(7/2^-)$, and is associated with the $f_{7/2}$ orbital. The newly-discovered band is therefore able to be described in terms of the $h_{9/2}$ configuration.

The unfavoured signature band of the $i_{13/2}$ yrast band has been tentatively assigned in the level scheme of ^{173}Pt, and was shown to exhibit strong splitting, indicating the possibility of triaxial deformation in the $i_{13/2}$ band. The interpretation of the $i_{13/2}$ band has already been described [9] as a decoupled valence neutron that has little influence on the yrast states. The observed backbending in the aligned angular momentum plots suggest that the first $i^2_{13/2}$ neutron alignment is 'blocked', and that the second neutron alignment takes place instead. The $h_{9/2}$ band's backbend takes place at larger values of the rotational frequency than the less neutron-deficient isotones of ^{173}Pt, and may indicate changes in the neutron mixing to the assumed $f_{7/2}$ neutron. Additional γ rays were found in-coincident with the 1236-keV dipole transition, as well as the 1306-keV transition, though no linking transition was found that feeds the latter state; this behaviour points to the possibility of a high-K band in ^{173}Pt.

Focal plane studies of ^{173}Pt's α decaying daughter, ^{169}Os, reveal a new delayed 35-keV γ transition for the first time, and was shown to be decaying from the previously reported $i_{13/2}$ yrast band. A second 112-keV γ transition, also found to decay from this isomer, was found to be of *M1* character. A tentative ∼80 keV transition was also observed, and was assumed to be an isomeric transition, of *M2* character, emanating from the yrast band-head. With a measured half-life of the isomer to be 17.3(12)μs, a reduced transition

probability was calculated to give $B(M2) = 17.9(12)$ W.u, a very unhindered transition. This leads to a tentative assignment of the ground state of ^{169}Os to be also $(7/2^-)$. Due to the low cross section of the direct production of the nucleus in-beam, and contamination of more intense reaction exit channels, coincidence analysis in the focal plane, or in-beam, could not have been performed.

Fine structure analysis of the decay of ^{173}Pt reveals two new delayed γ transitions that follow their corresponding α decay. The 112keV was found to be in coincident with an α energy consistent to previous work [10]. The 35-keV fine structure transition was previously unreported. α Q-value checks has confirmed all of the four fine structure transitions to decay from the ground state of ^{173}Pt. The 112- and 35-keV γ-ray energies were consistent to those that were produced following the decay of the $(13/2^+)$ isomer. The ground-state to ground-state transition was found to be unhindered, compatible with no change in angular momentum. The 35-keV fine structure transition was assumed to be of $\Delta\ell = 1$ character, feeding the $(5/2^-)$ state in ^{169}Os although this assignment is very tentative. The 112-keV fine structure transition, also of $\Delta\ell = 1$ character, was found to be more hindered than previously thought, and could be the result of structural change in ^{169}Os. The 136- and 171-keV transitions, assuming $\Delta\ell = 2$, were found to have reduced widths consistent to previous work [10], however the spin and parity of the states the α decay feeds could not have been established in this work.

It is possible for future experiments to expand on the knowledge of these nuclei even further, but require them to be the main focus; in this work's experiment, the nuclides ^{173}Hg and ^{173}Pt were the primary focus. This meant that the parameters used for the nuclear fusion reactions to take place were optimised to give the largest cross sections for ^{173}Hg and ^{173}Pt, but not necessarily for the others. Even so, ^{173}Pt could be populated more easily if krypton ions were used on the molybdenum target, and by studying the xn exit channels. An experiment has already been performed that populated states ^{169}Os with much more statistics than this work, and also took place at the University of Jyväskylä, using the reaction ^{94}Mo(^{78}Kr, $2p1n$)^{169}Os.

The nature of utilising symmetrical reactions in RITU also suffers from lower transmis-

sion efficiencies, as it was not originally designed to accommodate this. Construction of a new vacuum separator called MARA (Mass Analysing Recoil Apparatus) [116] is well under way at the University of Jyväskylä, and aims to provide high transmission efficiencies for reactions that RITU was not originally catering for. For example, symmetrical reactions that produce light compound nuclei can be accommodated here, which may provide more opportunities in populating states in highly exotic, neutron deficient nuclei.

Bibliography

[1] P. J. Woods and C. N. Davids, Annual Review of Nuclear and Particle Science **47**, 541 (1997).

[2] L. S. Ferreira, E. Maglione, and P. Arumugam, Journal of Physics: Conference Series **420**, 012053 (2013).

[3] T. Duguet, M. Bender, P. Bonche, and P.-H. Heenen, Physics Letters B **559**, 201 (2003).

[4] F. G. Kondev, M. P. Carpenter, R. V. F. Janssens, K. A. Saleem, and I. Ahmad, Physics Letters B **512**, 268 (2001).

[5] G. Poli *et al.*, Physical Review C **59**, R2979 (1999).

[6] R. Page *et al.*, Physical review C: Nuclear physics **53**, 660 (1996).

[7] R. G. Helmer, Nuclear Data Sheets **103**, 565 (2004).

[8] National Nuclear Data Center (NNDC), 2014.

[9] D. Joss *et al.*, Physical Review C **74**, 014302 (2006).

[10] J. T.-M. Goon, *Alpha and Gamma-ray Spectroscopic Studies of Au, Pt, and Ir Nuclei Near the Proton Dripline*, PhD thesis, 2004.

[11] D. Joss *et al.*, Physical Review C **66**, 054311 (2002).

[12] P. Moller, J. R. Nix, and K.-L. Kratz, Atomic Data and Nuclear Data Tables **66**, 131 (1997).

[13] T. Hild *et al.*, Physical Review C **51**, 1736 (1995).

[14] E. Rutherford, Philosophical Magazine Series 6 **21**, 669 (1911).

[15] J. J. Thompson, Philosophical Magazine Series 6 **7**, 237 (1904).

[16] N. Bohr, Philosophical Magazine Series 6 **26**, 476 (1913).

[17] E. Rutherford, Philosophical Magazine Series 6 **37**, 537 (1919).

[18] J. Chadwick, Nature **129**, 312 (1932).

[19] K. Heyde*Basic Ideas and Concepts in Nuclear Physics* No. 0-7503-0535-5 (Institute of Physics Publishing, 1999).

[20] R. Shurtleff, American Journal of Physics **57**, 552 (1989).

[21] E. Paul, Advanced nuclear physics, 2009.

[22] J. C. Caillon and J. Labarsouque, Physical Review C **54**, 2069 (1996).

[23] T. H. R. Skyrme, Philosophical Magazine **1**, 1043 (1956).

[24] R. B. Firestone *et al.*, *Table of Isotopes* (, 1996).

[25] V. M. Strutinsky, Nuclear Physics A **95**, 420 (1967).

[26] H. Becquerel, Comptes Rendus **122**, 420 (1896).

[27] E. Rutherford, Philosophical Magazine Series 6 **4**, 315 (1902).

[28] C. Qi, R. J. Liotta, and R. Wyss, Journal of Physics: Conference Series **381**, 012131 (2012).

[29] C. L. Cowan, F. Reines, F. B. Harrison, H. W. Kruse, and A. D. McGuire, Science **124**, 103 (1956).

[30] J. Beringer *et al.*, Physical Review D **86**, 010001 (2012).

[31] W. Bambynek *et al.*, Reviews of Modern Physics **44**, 716 (1972).

[32] L. Hong-Feng, G. Li-Sheng, and M. Jie, Chinese Physics Letters **23**, 2940 (2006).

[33] V. E. Viola Jr. and G. T. Seaborg, Journal of Inorganic and Nuclear Chemistry **28**, 741 (1966).

[34] D. Ni and Z. Ren, Romanian Journal of Physics **57**, 407 (2012).

[35] R. Bonetti and A. Guglielmetti, Romanian Reports in Physics **59**, 301 (2007).

[36] P. E. Hodgson*Nuclear heavy-ion reactions* No. 0-19-851514-6 (Oxford University Press, 1978).

[37] H. Bohn *et al.*, Physical Review Letters **29**, 1337 (1972).

[38] M. B. Smith *et al.*, Physics Letters B **551**, 262 (2003).

[39] J. B. Cumming and D. E. Alburger, Physical Review C **31**, 1494 (1985).

[40] T. B. Ryves, Journal of Physics G: Nuclear and Particle Physics **6**, 763 (1980).

[41] C. W. Beausang and J. Simpson, Journal of Physics G: Nuclear and Particle Physics **22**, 527 (1996).

[42] G. Duchene *et al.*, Nuclear Instruments and Methods in Physics Research Section A: Accelerators, Spectrometers, Detectors and Associated Equipment **432**, 90 (1999).

[43] D. C. Radford, Nuclear Instruments and Methods in Physics Research Section A: Accelerators, Spectrometers, Detectors and Associated Equipment **361**, 297 (1995).

[44] P. T. Greenlees *et al.*, Physical Review Letters **109**, 012501 (2012).

[45] M. Leino, Nuclear Instruments and Methods in Physics Research Section B **126**, 320 (1997).

[46] A. N. Andreyev *et al.*, Nuclear Instruments and Methods in Physics Research Section A: Accelerators, Spectrometers, Detectors and Associated Equipment **533**, 422 (2004).

[47] R. Page *et al.*, Nuclear Instruments and Methods in Physics Research Section B: Beam Interactions with Materials and Atoms **204**, 634 (2003).

[48] R. S. Simon *et al.*, Zeitschrift fur Physik A: Atoms and Nuclei **325**, 197 (1986).

[49] J. Sarén, J. Uusitalo, M. Leino, and J. Sorri, Nuclear Instruments and Methods in Physics Research Section A: Accelerators, Spectrometers, Detectors and Associated Equipment **654**, 508 (2011).

[50] E. S. Paul *et al.*, Physical Review C **51**, 78 (1995).

[51] H. Kettunen *et al.*, Physical Review C **69**, 054323 (2004).

[52] M. D. Z. James F. Ziegler, Jochen P. Biersack, *SRIM: The Stopping and Range of Ions in Matter* (, 2012).

[53] I. Lazarus *et al.*, IEEE Transactions on Nuclear Science **48**, 567 (2001).

[54] P. Rahkila, Nuclear Instruments and Methods in Physics Research Section A: Accelerators, Spectrometers, Detectors and Associated Equipment **595**, 637 (2008).

[55] D. Seweryniak, J. Nyberg, C. Fahlander, and A. Johnson, Nuclear Instruments and Methods in Physics Research Section A: Accelerators, Spectrometers, Detectors and Associated Equipment **340**, 353 (1994).

[56] R. Wyss, Nuclear Instruments and Methods in Physics Research Section A: Accelerators, Spectrometers, Detectors and Associated Equipment **256**, 499 (1987).

[57] G. D. Dracoulis, R. A. Bark, and A. E. Stuchbery, Nuclear Physics A **486**, 414 (1988).

[58] S. Hofmann, W. Faust, G. Miinzenberg, W. Reisdorf, and P. Armbruster, Zeitschrift Physik A **70**, 53 (1979).

[59] S. Hofmann *et al.*, Zeitschrift fur Physik A: Atoms and Nuclei **299**, 281 (1981).

[60] P. J. Woods *et al.*, Nuclear Instruments and Methods in Physics Research A **276**, 195 (1989).

[61] H. A. Enge *et al.*, Physical Review C **25**, 1830 (1982).

[62] A. Thornthwaite *et al.*, Physical Review C **86**, 1 (2012), arXiv:1212.4852v1.

[63] G. D. Dracoulis *et al.*, Physical Review C **87**, 014326 (2013).

[64] I. M. Band, M. B. Trzhaskovskaya, C. W. Nestor, P. O. Tikkanen, and S. Raman, Atomic Data and Nuclear Data Tables **81**, 1 (2002).

[65] S. Raman, C. Nestor, A. Ichihara, and M. Trzhaskovskaya, Physical Review C **66**, 044312 (2002).

[66] T. Kibedi, *BrIcc program to evaluate conversion coefficients: User's manual for version 2.3* (, 2011).

[67] D. Rupnik, E. F. Zganjar, J. L. Wood, P. B. Semmes, and P. F. Mantica, Physical Review C **58**, 771 (1998).

[68] A. Rytz, Nuclear Data Tables **47**, 205 (1991).

[69] E. Hagberg, X. J. Sun, V. T. Koslowsky, H. Schmeing, and J. C. Hardy, Physical Review C **45**, 1609 (1992).

[70] E. Runte *et al.*, Zeitschrift fur Physik A: Atoms and Nuclei **324**, 119 (1986).

[71] K. H. Schmidt, C. C. Sahm, H. G. Clerc, and K. Pielenz, Zeitschrift fur Physik A: Atoms and Nuclei **316**, 19 (1984).

[72] L. Bianco *et al.*, Nuclear Instruments and Methods in Physics Research Section A: Accelerators, Spectrometers, Detectors and Associated Equipment **597**, 189 (2008).

[73] S. Della Negra, C. Deprun, D. Jacquet, and Y. Le Beyec, Zeitschrift fur Physik A: Hadrons and Nuclei **300**, 251 (1981).

[74] E. Hagberg *et al.*, Nuclear Physics A **318**, 29 (1979).

[75] J. Simpson, M. Bates, C. Brookes, and P. J. Nolan, Nuclear Instruments and Methods in Physics Research A **269**, 209 (1988).

[76] C. Scholey *et al.*, Physical Review C **81**, 014306 (2010).

[77] D. Beck *et al.*, Nuclear Physics A **626**, 343 (1997).

[78] Y. A. Litvinov *et al.*, Nuclear Physics A **756**, 3 (2005).

[79] C. M. Baglin, Nuclear Data Sheets **111**, 1807 (2010).

[80] C. Reich, Nuclear Data Sheets **90**, 645 (2000).

[81] B. Singh, Nuclear Data Sheets **102**, 1 (2004).

[82] R. G. Helmer, Nuclear Data Sheets **107**, 507 (2006).

[83] M. S. Basunia, Nuclear Data Sheets **107**, 791 (2006).

[84] B. Singh, Nuclear Data Sheets **93**, 243 (2001).

[85] C. W. Reich, Nuclear Data Sheets **104**, 1 (2005).

[86] A. Artna-Cohen, Nuclear Data Sheets **79**, 1 (1996).

[87] M. R. Bhat, Nuclear Data Sheets **89**, 797 (2000).

[88] C. M. Baglin, Nuclear Data Sheets **96**, 611 (2002).

[89] M. Rowe *et al.*, Physical Review C **65**, 1 (2002).

[90] C. N. Davids *et al.*, Physical Review C **55**, 2255 (1997).

[91] C. W. Reich and B. Singh, Nuclear Data Sheets **111**, 1211 (2010).

[92] R. G. Helmer, Nuclear Data Sheets **99**, 483 (2003).

[93] F. Meissner, H. Salewski, W.-D. Schmidt-Ott, U. Bosch-Wicke, and R. Michaelsen, Zeitschrift fur Physik A: Hadrons and Nuclei **343**, 283 (1992).

[94] R. J. Irvine *et al.*, Physical Review C **55**, 1621 (1997).

[95] K. Lagergren *et al.*, Physical Review C **83**, 014313 (2011).

[96] K. Theine *et al.*, Nuclear Physics A **536**, 418 (1992).

[97] D. Roux *et al.*, Physical Review C **63**, 024303 (2001).

[98] M. Sandzelius *et al.*, Physical Review C **80**, 054316 (2009).

[99] G. Audi *et al.*, Chinese Physics C **36**, 1287 (2012).

[100] M. Wang *et al.*, Chinese Physics C **36**, 1603 (2012).

[101] J. O. Rasmussen, Physical Review **113**, 1593 (1959).

[102] F. A. Ali, *Shape Coexistence in the Proton-Unbound Nucleus* ^{177}Au, PhD thesis, University of Liverpool, UK, 2014.

[103] M. Venhart *et al.*, Physics Letters B **695**, 82 (2011).

[104] M. I. Macias-Marques *et al.*, Nuclear Physics A **427**, 205 (1984).

[105] W. F. Mueller *et al.*, Physical Review C **59**, 2009 (1999).

[106] C. Bourgeois, P. Kilcher, B. Roussiere, J. Sauvage-Letessier, and M. G. Porquet, Nuclear Physics A **386**, 308 (1982).

[107] J. L. Wood, M. O. Kortelahti, E. F. Zganjar, and P. B. Semmes, Nuclear Physics A **600**, 283 (1996).

[108] F. A. Ali, D. T. Joss, M. Venhart, J. L. Wood, and R. D. Page, Shape Coexistence and the Strongly Coupled Band in ^{177}Au (*To be published*), 2014.

[109] H. Watkins *et al.*, Physical Review C **84**, 2 (2011).

[110] A. N. Andreyev, *To be published*, 2014.

[111] D. O'Donnell *et al.*, Physical Review C **79**, 051304 (2009).

[112] R. A. Bark *et al.*, Nuclear Physics A **646**, 399 (1999).

[113] J. Recht *et al.*, Nuclear Physics A **440**, 366 (1985).

[114] M. Cromaz *et al.*, Physical Review C **59**, 2406 (1999).

[115] A. J. Kreiner, M. A. J. Mariscotti, C. Baktash, E. der Mateosian, and P. Thieberger, Physical Review C **23**, 748 (1981).

[116] J. Sarén *et al.*, Nuclear Instruments and Methods in Physics Research Section B: Beam Interactions with Materials and Atoms **266**, 4196 (2008).